

PARTICLE DYNAMICS AND PARTICLE-CELL INTERACTION
IN MICROFLUIDIC SYSTEMS

by

Matthew T. Stamm

A Dissertation Submitted to the Faculty of the

DEPARTMENT OF AEROSPACE AND MECHANICAL ENGINEERING

In Partial Fulfillment of the Requirements

For the Degree of

DOCTOR OF PHILOSOPHY

WITH A MAJOR IN MECHANICAL ENGINEERING

In the Graduate College

THE UNIVERSITY OF ARIZONA

2013

THE UNIVERSITY OF ARIZONA
GRADUATE COLLEGE

As members of the Dissertation Committee, we certify that we have read the dissertation prepared by Matthew Stamm, titled Particle Dynamics and Particle-Cell Interaction in Microfluidic Systems and recommend that it be accepted as fulfilling the dissertation requirement for the Degree of Doctor of Philosophy.

_____ Date: July 31, 2013
Pak Kin Wong

_____ Date: July 31, 2013
Xiaoyi Wu

_____ Date: July 31, 2013
Yitshak Zohar

Final approval and acceptance of this dissertation is contingent upon the candidate's submission of the final copies of the dissertation to the Graduate College.

I hereby certify that I have read this dissertation prepared under my direction and recommend that it be accepted as fulfilling the dissertation requirement.

_____ Date: July 31, 2013
Dissertation Director: Yitshak Zohar

STATEMENT BY AUTHOR

This dissertation has been submitted in partial fulfillment of the requirements for an advanced degree at the University of Arizona and is deposited in the University Library to be made available to borrowers under rules of the Library.

Brief quotations from this dissertation are allowable without special permission, provided that an accurate acknowledgement of the source is made. Requests for permission for extended quotation from or reproduction of this manuscript in whole or in part may be granted by the head of the major department or the Dean of the Graduate College when in his or her judgment the proposed use of the material is in the interests of scholarship. In all other instances, however, permission must be obtained from the author.

SIGNED: Matthew T. Stamm

ACKNOWLEDGEMENTS

I would like to express my sincerest gratitude to the following people:

Prof. Yitshak Zohar, my advisor, for allowing me the use of his lab and supervising my work over the years, for advising me on my work throughout, for teaching me how proper research is done, for the countless colloquial intellectually-stimulating conversations, and for making himself nearly always available for advice, guidance, questions, or even just to talk.

Prof. Xiaoyi Wu for sitting on my committees, allowing me the use of his equipment, and for his efforts in teaching and perpetual eagerness to help.

Prof. Pak Kin Wong for sitting on my committees, allowing me the use of his equipment, and for his teaching and feedback on how to improve for the future.

Dr. Linan Jiang for the many fascinating conversations, for her constant eagerness to help, her patience in answering endless questions in hopes of furthering the understanding of others', and her persistence in finding solutions to others' problems when she did not have an answer already.

Dr. Linda Zheng for her help and advice on my work when it related to things she had done in the past, and for the numerous intellectually-stimulating conversations related to a such a vast and diverse array of topics ranging from classes to lab work to politics and religion and more.

Dr. Luthur Cheung for his significant role in teaching me the way of the lab when I first arrived, and for sharing his expertise and experience with me, helping me to become independent.

Mr. Andrew Steven Trickey-Glassman for his hard and very diligent work that gave me confidence to allow him to work with my experiments with no supervision, and to rely on results that he produced and measurements he made. My trust in these areas is not easily earned, but with Andrew I had no reservations.

Dr. Jonathan Sexton for his consultations in all matters related to microbiology and his explanations of the issues of concern and tips on how to avoid problems, for the random reagent here and there, and for his friendship throughout the many years.

My friends for not forgetting me during long periods of absence from social functions, and for treating me as though I had been there all along upon my return.

My family for supporting my decisions and pursuits, for the encouragement that never wavered, for the love and understanding when I could not see them, and my parents for raising me as they did.

Finally, my wife Karen, for more than can fit within these pages.

DEDICATION

To the woman whose incredible work ethic and dedication have already saved more lives than I could possibly hope for any part of this work to ever do. The woman whose friendship ensured that once I came home, no matter what had transpired before, the rest of the day would be good. The woman who put up with my often ridiculous hours and the bad moods they caused. The woman whose love has kept me inspired, and whose decade of companionship has kept me motivated to work for more than just myself. To the most impressive and amazing person I have ever had the honor to know.

To my lovely wife Karen.

And in memory of

Rodger Stamm, who selflessly forwent life-prolonging treatment in favor of suffering over burdening the family he was leaving behind with his medical expenses.



Born Rodger Lee Stamm January 28, 1943
Succumbed to prostate cancer February 14, 2013

TABLE OF CONTENTS

| | |
|--|----|
| LIST OF FIGURES | 8 |
| ABSTRACT..... | 12 |
| 1. INTRODUCTION | 14 |
| 1.1 Non-Specific Interactions in Microfluidic Systems | 15 |
| 1.2 Motivation for the Study of Specific Interactions..... | 19 |
| 1.3 Targeted Drug Delivery..... | 20 |
| 1.4 Characterization of Specific-Interaction Processes | 21 |
| 2. METHODS AND MATERIALS..... | 23 |
| 2.1 Particle Clustering | 23 |
| 2.1.1 Cluster Growth Modeling..... | 23 |
| 2.1.2 Microchannel Design and Fabrication | 25 |
| 2.1.3 Experimental Program..... | 27 |
| 2.2 Cerasome Functionalization | 28 |
| 2.2.1 Cerasome Formation | 28 |
| 2.3 Particle-Cell Interaction in an Orbitally-Mixed Suspension | 30 |
| 2.3.1 Image Analysis and Quantification of Particle-Cell Binding..... | 31 |
| 2.4 Particle-Cell Interaction in a Microchannel | 33 |
| 2.4.1 Microchannel Fabrication..... | 33 |
| 2.4.2 Functionalized Particle Suspension Preparation and Handling..... | 34 |
| 2.4.3 Cell Detachment and Preparation for Experiments | 37 |
| 2.4.4 Microchannel Functionalization and Cell Immobilization..... | 37 |
| 2.4.5 Experimental Apparatus | 39 |
| 2.4.6 Experimental Program..... | 41 |
| 2.4.7 Cell Fixation, Channel Disassembly, and Specimen Preparation | 43 |
| 3. PARTICLE-CELL INTERACTION MODELING | 45 |
| 3.1.1 Generalized Form of the Mathematical Model | 45 |
| 3.1.2 Ligand-Receptor Bond Dynamics | 46 |
| 4. RESULTS AND DISCUSSION | 50 |
| 4.1 Cluster Area Growth | 50 |
| 4.1.1 Suspension Void Fraction Effect..... | 51 |
| 4.1.2 Effect of Shear Strain Rate | 53 |

TABLE OF CONTENTS - *Continued.*

| | | |
|-------|--|-----|
| 4.1.3 | Effect of Channel-Height to Particle-Diameter Ratio | 55 |
| 4.2 | Cerasome Functionalization | 59 |
| 4.2.1 | Cerasome Functionalization with Antibodies | 59 |
| 4.2.2 | Characterization of Bio-Functionalized Cerasomes | 62 |
| 4.2.3 | Functionalized Particle – Target Cell Interaction..... | 64 |
| 4.3 | Specific Interactions Between Antibody-Functionalized Particles and Circulating Tumor Cells in an Orbitally-Mixed Suspension | 66 |
| 4.3.1 | Effects of Incubation Time and Particle Concentration | 67 |
| 4.3.2 | Particle Desorption | 69 |
| 4.3.3 | Loss of Binding Affinity | 71 |
| 4.3.4 | Cell-Particle-Cell Interactions | 72 |
| 4.3.5 | Scaling Parameters for Cell Surface Coverage | 74 |
| 4.3.6 | Cell-Particle-Cell Interaction Analysis | 79 |
| 4.4 | Specific Interactions Between Antibody-Functionalized Particles and Circulating Tumor Cells in a Microfluidic Device | 83 |
| 4.4.1 | Validation of Specimen Preparation Methods..... | 84 |
| 4.4.2 | Modeling Particle-Cell Binding For Immobilized Cells in a Steady Shear Flow | 85 |
| 4.4.3 | Asymptotic Analysis and the Linear Approximation..... | 89 |
| 4.4.4 | Effects of Particle Concentration and Incubation Time | 90 |
| 4.4.5 | Effects of Shear Strain Rate | 101 |
| 4.4.6 | Restrictions on Experimental Control Parameters | 105 |
| 4.4.7 | Comparison of Experimental Results to the Model Description..... | 107 |
| 5. | GENERALIZED DESCRIPTION PARTICLE-CELL INTERACTION | 111 |
| 6. | CONCLUSIONS..... | 117 |
| | REFERENCES | 121 |

LIST OF FIGURES

- Figure 1 – Schematics of (a) microchannel fabrication steps, and (b) experimental setup. Microchannel fabrication employed standard photolithographic techniques to create a silicon mold from which channels were cast in PDMS. Channels were capped with silicon and observed under a microscope while particle suspension flow was in progress..... 26
- Figure 2 – A schematic illustration of cerasome formation from organotrialkoxysilane lipids. Dissolved lipids were deposited on the walls of a glass vessel as the solvent evaporated. The dried vessels were filled with DI water and subjected to ultrasonic excitation. Detached lipids suspended in water and self-assembled to form the hollow spherical structure of the cerasome. Spontaneous cross-linking at the lipid head groups occurred over a subsequent period, yielding the structurally robust, lipid-bilayer vesicle that was the fully-formed cerasome..... 28
- Figure 3 – SEM images of cerasomes after formation and prior to functionalization..... 29
- Figure 4 – Examples of cerasome size distributions of an original sample and a filtered sample measured by dynamic light scattering. Credit: Dr. Linan Jiang 30
- Figure 5 – A schematic illustration of the method used to quantify fractional cell-surface coverage f due to particle-cell binding. The fractional cell-surface coverage is calculated as the ratio of the projected area on the cell surface for which further particle binding is prohibited by size-exclusion to the total projected area of the spherical cell..... 32
- Figure 6 – Schematic of completed experimental apparatus. Magnetic actuation provided stirring of the suspension in the syringe (to) allowing for longer periods of stability. The channel (bottom) was supplied by the syringe which was driven by a pump. 40
- Figure 7 – Qualitative depiction of steady-state N_{RB} value dependence on binding force illustrating degeneracy owing to the existence of a critical force value. 49
- Figure 8 – Total cluster area growth in time under various experimental conditions. 51
- Figure 9 – Average cluster area growth rate as a function of suspension void fraction ($h/d = 10$, $S = 7400 \text{ s}^{-1}$). 53
- Figure 10 – Growth rate coefficient as a function of suspension shear strain rate (blue dashed line), ($h/d = 10$, $\varphi = 0.001$). The other lines are presented for comparison with findings from broadly similar work done by others. 55
- Figure 11 – Growth rate coefficient as a function of channel-height to particle-diameter ratio ($\varphi = 0.001$, $S = 7400 \text{ s}^{-1}$). The data point for $h/d=2$ is not the result of the interactions of interest herein and is therefore omitted from the fit. 57

LIST OF FIGURES – Continued.

- Figure 12 – Images of a pre-formed cluster in an experiment with $h/d = 2$: (a) moving with the suspension flow at the microchannel inlet region, and (b) attached on the microchannel bottom surface a short distance downstream ($\phi = 0.001$, $S = 7400 \text{ s}^{-1}$) 58
- Figure 13 – Representative images of cluster patterns due to different h/d : (a) $h/d = 10$, and (b) $h/d = 2$ ($\phi = 0.001$, $S = 7400 \text{ s}^{-1}$) 59
- Figure 14 – A flow chart of the various major steps required in the functionalizing process. 61
- Figure 15 – Micrographs of cerasomes using bright field (A1 and B1) and fluorescence imaging (A2 and B2) taken: before (top), and after (bottom) functionalization with antibodies. 63
- Figure 16 – A typical EpCAM-expressing target cancer cell (BT-20) after exposure to particles functionalized with: (a) the proper counter-receptor anti-human EpCAM, and (b) anti-mouse IgG, demonstrating the specific binding capabilities of the functionalized particles. All other experimental conditions were identical. 65
- Figure 17 – Micrographs of individual cells with bound particles for cell coverage evaluation under various experimental conditions. Note: Depth-of-focus limitations preclude clear rendering of all particles in any single image. Scale bars $10 \mu\text{m}$ 66
- Figure 18 – Surface coverage as a function of particle concentration for various incubation times. 67
- Figure 19 – Fractional cell-surface coverage as a function of incubation time for various particle concentrations. 68
- Figure 20 – Comparison of surface coverage between cells with an initial coverage to those of standard experiments, wherein cells had no initial coverage, for $N_p=6000 \mu\text{l}^{-1}$ showing the lack of significant particle desorption with incubation time. 70
- Figure 21 – Surface coverage as a function of cell incubation time prior to introduction of particles with subsequent particle-cell incubation time fixed at 20 min. for particle concentrations $N_p=6000$ and $20000 \mu\text{l}^{-1}$. Cell incubation time without particles does not affect the particle adsorption rates; effects related to cell viability loss are negligible. 72
- Figure 22 – Example of counting scheme. The total population is 8 including 5 individual cells and 3 clusters. Individual cells comprise $5/8=62.5\%$ of total population. 73
- Figure 23 – Percentage of population appearing as individual cells for various times and particle concentrations; 100% means that all cells appear as individuals with no cell clustering. 74

LIST OF FIGURES – *Continued.*

- Figure 24 – Cell surface coverage normalized by its steady-state value, f/f_{ss} , as a function of the normalized incubation time, t/τ . Experimental results (symbols) collapse onto a single exponential curve (solid line calculated using Equation 25) for the low particle concentrations but not for the high particle concentration $N_p=40000 \mu\text{l}^{-1}$ 76
- Figure 25 – A comparison between experimentally estimated steady-state and time-constant values (symbols) as a function of the particle concentration and calculated values (dash lines) based on a first-order interaction model (Equations 25-27). 78
- Figure 26 – Percentage of population appearing as individual cells re-plotted from Figure 23 and fit by Equation 32. Best-fit lines calculated using the same cluster-dissociation timescale $\tau_d=6.9$ min, but different cluster-association timescales $\tau_a=\tau_a(N_p)$. Comparison shows that cell-particle-cell clustering processes are association-dominated for only the highest particle concentration $N_p=40000 \mu\text{l}^{-1}$ for which $\tau_a/\tau_d \approx 0.7$ 81
- Figure 27 – Images taken (a) before and (b) after removal of the PDMS channel. Although some free particles are seen to have moved (green circles), particles bound to cells remain undisturbed. 85
- Figure 28 – Average number of bound particles per cell ν (left axis) and fractional cell-surface coverage f (right axis) as functions of flow volume for various particle concentrations with flow rate fixed at the reference value $Q=1.0 \mu\text{l/s}$. Dashed lines are linear fits made for the purposes of analysis and discussion and are not intended to indicate linear behavior..... 91
- Figure 29 – Average number of bound particles per cell ν (left axis) and fractional cell-surface coverage f (right axis) as functions of particle concentration for various flow volumes with flow rate fixed at the reference value $Q=1.0 \mu\text{l/s}$. Dashed lines are linear fits made for the purposes of analysis and discussion and are not intended to indicate linear behavior..... 93
- Figure 30 – Slopes of linear fits to the data shown in Figure 28 as a function of particle concentration..... 94
- Figure 31 – Slopes of linear fits to the data shown in Figure 29 plotted as a function of flow volume..... 94
- Figure 32 – Average number of bound particles per cell ν (left axis) and fractional cell-surface coverage f (right axis) functions of $N_p * V$ with flow rate fixed at the reference value $Q=1.0 \mu\text{l/s}$. For comparison, the flow volumes are indicated by the different markers; particle concentration may be deduced from the x-coordinate. The data shown here include all of the data shown in Figure 28 and Figure 29; each point corresponds to a different value of the pair (N_p, V) . The quality of fit achieved by a straight line indicates linearity of f and ν in both N_p and V 98

LIST OF FIGURES – Continued.

- Figure 33 – Average number of bound particles per cell ν (left axis) and fractional cell-surface coverage f (right axis) as functions of flow rate for various particle concentrations with flow volume fixed at the reference value $V=100 \mu\text{l}$ 102
- Figure 34 – Average number of bound particles per cell ν (left axis) and fractional cell-surface coverage f (right axis) as functions of particle concentration for various flow rates with flow volume fixed at the reference value $V=100 \mu\text{l}$ 103
- Figure 35 – Slopes of linear fits in Figure 34 as a function of flow rate plotted on (a) a normal scale, showing the strong affect shear strain rate can have on particle-cell binding at low flow rates and (b) a log-log scale, illustrating the high quality of fit achieved using a power-law relationship. 104
- Figure 36 – Average number of bound particles per cell ν (left axis) and fractional cell-surface coverage f (right axis) as functions of the product $N_p(Q/Q_0)^{-0.63}$ for several values of particle concentration with flow volume fixed at the reference value $V=100 \mu\text{l}$. Analysis shows that this scaling of the x-coordinate should yield a linear relationship with ν and f ; the dashed line is for comparison purposes only. 105
- Figure 37 – Average number of bound particles per cell ν (left axis) and fractional cell-surface coverage f (right axis) as functions of time scaled by the time constant obtained from the theoretical model and calculated using the empirically-found value of K_{on} . All data appearing in Figure 28, Figure 29, Figure 32, Figure 33, Figure 34 and Figure 36 appear here. The solid curve was calculated from Equation 57. Different markers are for comparison and indicate different flow volumes without indicating any commonality among particle concentration or flow rate values. 110
- Figure 38 – Cell surface coverage normalized by its steady-state value, f/f_{ss} , as a function of the normalized incubation time, t/τ , plotted on a normal scale (top) and a log-log scale (bottom). Experimental results shown in Figure 18 and Figure 19 (set “A”) and in Figure 28, Figure 29, Figure 33 and Figure 34 (set “B”) collapse onto a single exponential curve (calculated using Equation 58). Set “A” corresponds to data resulting from experiments with cells freely moving in suspension as described in Section 4.3. Set “B” corresponds to data resulting from experiments involving immobilized cells in a microchannel as described in Section 4.4. Only the data for the high particle concretion of $N_p=40000 \mu\text{l}^{-1}$ in set “A” deviate substantially. This deviation occurs when cell-particle-cell clustering is at its highest, as seen from Figure 23. This phenomenon is not described by the model, which examines the process on an individual-cell level. 115

ABSTRACT

Particle-laden flow in a microchannel resulting in aggregation of microparticles was investigated to determine the dependence of the cluster growth rate on the following parameters: suspension void fraction, shear strain rate, and channel-height to particle-diameter ratio. The growth rate of an average cluster was found to increase linearly with suspension void fraction, and to obey a power-law relationships with shear strain rate as $S^{0.9}$ and channel-height to particle-diameter ratio as $(h/d)^{-3.5}$.

Ceramic liposomal nanoparticles and silica microparticles were functionalized with antibodies that act as targeting ligands. The bio-functionality and physical integrity of the cerasomes were characterized. Surface functionalization allows cerasomes to deliver drugs with selectivity and specificity that is not possible using standard liposomes.

The functionalized particle-target cell binding process was characterized using BT-20 breast cancer cells. Two microfluidic systems were used; one with both species in suspension, the other with cells immobilized inside a microchannel and particle suspension as the mobile phase. Effects of incubation time, particle concentration, and shear strain rate on particle-cell binding were investigated.

With both species in suspension, the particle-cell binding process was found to be reasonably well-described by a first-order model. Particle desorption and cellular loss of binding affinity in time were found to be negligible; cell-particle-cell interaction was identified as the limiting mechanism in particle-cell binding. Findings suggest that separation of a bound particle from a cell may be detrimental to cellular binding affinity.

Cell-particle-cell interactions were prevented by immobilizing cells inside a microchannel. The initial stage of particle-cell binding was investigated and was again found to be reasonably well-described by a first-order model.

For both systems, the time constant was found to be inversely proportional to particle concentration. The second system revealed the time constant to obey a power-law relationship with shear strain rate as $\tau \propto S^{-.37 \pm .06}$. Under appropriate scaling, the behavior displayed in both systems is well-described by the same exponential curve. Identification of the appropriate scaling parameters allows for extrapolation and requires only two empirical values. This could provide a major head-start in any dosage optimization studies.

1. INTRODUCTION

In recent years, micro/nanoscale particles have seen increased use in a variety of applications. Use as part of a microfluidic system constitutes a substantial fraction of these applications. Multi-phase flow significantly complicates the physics involved regardless of what the phases may be. This is especially true when working fluids contain suspended or colloidal solid micro/nanoscale particles. Whether part of a flow in a microfluidic chip, suspended in a fluid contained in a large vessel, or circulating in the bloodstream, the presence of solid micro/nanoparticles in a working fluid constitutes a multi-phase microfluidic system. Nearly all microfluidic systems share some common characteristics, perhaps the most notable of which is the dominance of surface forces over body forces. These surface forces are frequently due to numerous complex interactions that can cause problematic effects, but also provide new possibilities that are not seen on a larger scale. For instance, antibody-antigen interaction relies on these various forces to forge highly specific and/or selective affinities to one another. Conversely, these forces may cause indiscriminant binding of two species leading to clogging of microchannels, loss of particles, etc. This can be quite detrimental to microfluidic systems, causing decreased performance, obscured data or even complete failure. In order to design for maximum performance of a microfluidic system, it is therefore necessary to characterize both desired and undesired effects. This work approaches the study of these phenomena from several angles; non-specific interactions, specific interactions, and a method of achieving specificity are investigated. Particle dynamics in aggregation processes, due to non-specific interactions in a suspension flow in a microfluidic device, are investigated experimentally and analyzed theoretically. A method of functionalizing particles with antibodies, in order to achieve specific-

targeting capabilities, is then developed and utilized as the foundation of investigations of specific interactions. The specific interactions of antibody-functionalized particles with the target cells are examined from a macroscopic standpoint. These interactions are further investigated with the aid of a microfluidic device, enabling the study of the effects of additional parameters through increased control. Throughout the work, a theoretical model of particle-cell interaction is developed and compared with the various results. The experimental results involving particle-cell interactions are brought together in their entirety, and compared with the aid of the theoretical model.

1.1 NON-SPECIFIC INTERACTIONS IN MICROFLUIDIC SYSTEMS

Effects due to van der Waals (VDW), electric double layer (EDL), hydrophobic and steric interactions, hydrogen and ionic bonding, and hydrodynamic forces are among those most commonly seen in microfluidic systems. Some of these result in strictly attractive forces, others strictly repulsive and some can be either one depending on various system constituent properties. It is rare for any single one of these effects to be the only significant interaction in a system so it is not uncommon for the sign of the net force between two surfaces (i.e. attractive or repulsive) to be strongly dependent on separation distance. Consequently, there nearly always exists at least one potential energy minimum. The separation distance at which such a minimum exists corresponds to a stable geometrical configuration of two bodies which results in binding. In suspensions and colloids, the result frequently manifests itself in adhesion of individual particles to other surfaces or each other, eventually leading to a population of many clusters and relatively few individual particles; a phenomenon known as aggregation, flocculation, or coagulation,

depending on context. The investigation of aggregation of microparticles in a dilute suspension flow in a microfluidic device is the first part of this work.

Multiple possible mechanisms of microchannel clogging due to flowing suspended particles have been proposed including simple size exclusion of the particles by the channel, random occurrence of a local high void fraction [1], and particle self-supporting arch formation within the channel [2]. The aggregation process in a microchannel often starts with the adhesion of single particles to the channel surface. Aggregation of additional individual particles results in clusters, which can subsequently act as single particles of a much larger size thereby augmenting the clogging phenomenon.

Various aspects of microchannel clogging have been investigated employing different theoretical, computational and experimental techniques. A survey of the available literature reveals several common factors that are reported to have a significant impact on particle aggregation. Some of the literature reports functional dependence of aggregation rate on various parameters for special cases.

The deposition of spherical particles onto cylindrical solid surfaces, accounting for van der Waals and electrical double-layer effects, was analyzed theoretically and investigated experimentally using oil droplets [3-4]. Particle motion and aggregation under pressure-driven flow through converging-diverging microchannels has also been studied experimentally [5]. Particle aggregation and capture by channel walls were studied using a soft-sphere discrete element model (DEM) with a “frozen deposit” assumption [6-7]. This assumption significantly decreases the computational expense of simulations but is not always appropriate as it does not allow for particle desorption. The applicability of the “frozen deposit” assumption has been

examined and it has indeed been confirmed that it is often inaccurate [6]. A kinetic clustering model combined with direct numerical simulations was used to analyze shear flow of particulate suspensions [8]. A direct simulation Monte Carlo (DSMC) method has been employed to investigate the effects of van der Waals forces on inter-particle interactions [9]. The DSMC investigations showed that increasing van der Waals forces can, in some cases, lead to cohesive forces that significantly affect the local particle concentration distribution. It is known that particle aggregation in shear flows (orthokinetic) is enhanced over that in static fluids with Brownian motion alone (perikinetic) [10]. However, excessive shear can decrease aggregation by breaking apart clusters and overcoming adhesive forces. In one study, the shear stress was reported to have a major effect on particle deposition; while for the most part absent within the microchannels, the headers were found to be quite susceptible to particulate fouling due to the lower shear stress [11]. A significant difference between the model descriptions and the experimental studies lies in the length scales of interest among the studies [12].

The Peclet number is a measure of the relative effects of advection and diffusion within a suspension flow. Accordingly, the orthokinetic regime is characterized by large Peclet numbers indicating advection dominance, while the perikinetic regime is diffusion-dominated and characterized by a small Peclet number. Therefore, for a very large Peclet number, $Pe \gg 1$, the Brownian motion effect becomes negligible. For suspensions in shear flows, a shear strain rate gradient can cause particle migration resulting in non-uniformity in void fraction spatial distribution in the suspension flow [13-14]. The frequency of particle-particle as well as particle-wall collisions, and consequently adhesions due to van der Waals attractive forces, increases with increasing shear strain rate within a certain range. Thus the aggregation rate is expected to

increase with increasing shear strain rate. However, under sufficiently large shear stress, the aggregates could break apart resulting in a plateau or even decrease in overall aggregation rate. These particle aggregation patterns in suspension flows have been qualitatively characterized by several experimental works and simulations [11,15-16].

Van der Waals and electrostatic forces due to the electric double layer (EDL) are highly sensitive to surface properties of both the particles and the channel wall as well as the properties of the working fluid [17]. The combinations and the relative degree of these effects not only determine the rate but also the type of aggregation. Multiple potential energy minima characterizing the interactions may exist thus allowing for different aggregate stability levels [18-19]. Furthermore, such forces do not necessarily behave monotonically with respect to the surface and/or fluid properties [20-21]. Thus, conducting experiments on particle aggregation of suspension flow in microchannels can be quite challenging. To circumvent these problems, less-sensitive systems utilizing electric or magnetic forces may be used to suppress the relative magnitude of van der Waals effects on aggregation rate by introducing long-range forces to the system. One study employing such a technique investigates the aggregation of paramagnetic particles in microchannel flows [22]. This study reported the aggregation mechanism for linear chains to be accumulation of isolated particles and/or other existing chains in the bulk flow. The chain growth rate was observed to increase with the shear strain rate and follow a power-law relationship. Recently, experiments investigating clogging of individual pores were conducted and a probabilistic model was developed [23]. It is reported that the adhesion probability of a particle to the pore surface is directly related to that of the particle passing within a critical

distance from the wall. This critical distance was found to be comparable to the typical thickness of an electrostatic double layer at low ionic concentration.

From the available literature, several of the most commonly reported factors influencing aggregation are suspension void fraction (i.e. particle concentration), shear strain rate, and the dimensions of the particles and channels. A work preceding what is presented herein reports on the formation and evolution of single clusters on a microchannel surface due to pressure-driven flow of dilute particle suspension [24]. Here, the effects of several control parameters, namely suspension void fraction, channel-height to particle-diameter ratio and suspension flow shear strain rate, on the growth rate of the average cluster area are further investigated. The functional dependence of the cluster growth rate on each of these control parameters is obtained experimentally and analyzed theoretically.

1.2 MOTIVATION FOR THE STUDY OF SPECIFIC INTERACTIONS

Treatment of diseases such as cancer usually requires the administration of large doses of drugs. The inability of a drug to target only tumor cells results in healthy cells being exposed to the harmful effects. The use of nanoparticles with the abilities to carry a payload of drugs within their cores and to possess “targeting” molecules on their surfaces is widely viewed as an ideal solution to many of the adverse effects of drug therapies [25].

Liposomes are vesicles consisting of a hydrophobic lipid bilayer membrane mimicking that of many kinds of biological cells. The primary application of liposomes lies in drug delivery [26,27]. Liposomes can be made to encapsulate drugs by forming the vesicles in a solution containing the drugs. The encapsulated solution is able to pass through the membrane only by way of passive diffusion, so the contents are retained for extended periods of time while the

liposome is in a suspension. The most common mechanisms of drug delivery by liposomes are passive diffusion through the membrane, and uptake of the vesicles by other lipid bilayer structures [28].

Using liposomes for drug delivery has an advantage in that the drugs are directed to cells, and consequently, drastically reduces the amount of drug introduced to the surrounding medium (e.g. blood). Another advantage is due to the enhanced permeability and retention effect and results in liposomes accumulating more in tumor tissue than in normal tissue. However, the mechanism by which liposomes attach to cells exhibits very low targeting selectivity and specificity [29], which leaves practically any healthy cell vulnerable [30-31]. The low selectivity and specificity achieved by liposomes can be very problematic. In order to deliver drugs and target a specific type of cell, an alternative binding mechanism must be employed. Consequently, much effort has recently been put toward the development of a host of new types of particles that have the potential for surface modification thereby creating a chemical foundation for various processes. Many diseases have seen improved treatment and diagnostics through the use of these particles [32-38], but the targeting of cancer cells has sparked particularly high interest amongst the research community.

1.3 TARGETED DRUG DELIVERY

While these numerous types of particles each have their own advantages, the standard liposome has already proven itself in many applications. There is great potential for liposomal particles if the problems that come with their use as drug delivery vehicles can be overcome. A novel class of liposomal organic-inorganic hybrid nanoparticles known as ‘cerasomes’ (for ceramic liposome) has recently been developed [39,40]. Cerasomes have a liposomal bilayer

structure but also have a siloxane network on their external surface (hence the descriptor ‘ceramic’). Consequently, cerasomes possess characteristics and potential applications similar to those of liposomes, e.g. bio-compatibility and drug delivery applications. In addition, the siloxane network present on cerasomes may be exploited for surface functionalization purposes. Moreover, the siloxane network on the surface adds rigidity, and thus overcomes the inherent morphological instability of liposomes [41], which is a serious problem in practical applications [39,42].

The second part of this work presents a method of modifying the cerasome external surface such that the vesicle no longer indiscriminately targets any lipid bilayer, but instead is able to target a specific type of cell. The presence of the siloxane network on the external surface of a cerasome allows for the use of technologies and processes adapted from those previously developed for silicon surfaces to functionalize the cerasome surface. This is achieved by immobilizing antibodies on the cerasome surface that serve as targeting ligands [43]. The antibodies on the surface of a drug-containing cerasome recognize and bind to targeted receptors on a particular type of cell, and therefore allow drug delivery with improved selectivity and specificity.

1.4 CHARACTERIZATION OF SPECIFIC-INTERACTION PROCESSES

While there have been many studies describing various qualitative aspects of particle-cell interactions [25,29,30], despite interest in the topic going back several years [44], relatively few have quantitatively examined the interactions between these specialized particles and the cells to which they are intended to deliver drugs. Much of this research is being geared primarily toward therapeutic applications [25,29-31] and, despite the potential for great improvement over

conventional treatments, the issue of dosage must nevertheless be addressed [25]. Proper dosage to balance efficacy and side-effects requires more than just a fundamental understanding of the relevant interactions; it necessitates characterization of these interactions through quantitative analysis.

Utilizing particles functionalized with antibodies via the aforementioned method [45], an experimental quantitative characterization of particle-cell interaction in a mixed suspension is performed and a mathematical model is developed. Analysis of quantitative data is used to determine the relative importance of several aspects of the particle-cell interaction processes. Analysis shows that observations cannot be explained by only particle-cell interactions, and that other interactions involving multiple cells must be considered. A second experimental system is used to circumvent these interactions; a microfluidic channel is employed with which the effects of particle concentration, shear strain rate, and incubation time are investigated experimentally. From these experiments, empirical values are obtained allowing the mathematical model to be fit to the data. Scaling parameters are identified for each system and used to normalize experimental data. Once normalized, the data fall on a single exponential curve. The curve is defined by the single equation that is recovered from both variants of the mathematical model when subjected to the same normalization.

2. METHODS AND MATERIALS

2.1 PARTICLE CLUSTERING

2.1.1 Cluster Growth Modeling

Aggregation of particles in suspension flow is due to one or more of the following: particle-particle, particle-cluster or cluster-cluster interactions. In a microchannel, the close proximity of solid boundaries to the suspended particles gives rise to particle-surface and cluster-surface interactions as well. Incipience of a cluster on the channel surface starts with a particle adhering to the surface through particle-surface interaction, which seems to be random in space and time. Most clusters are initiated within the initial 5 min duration of the suspension flow through the microchannel. The initial clusters are sparse in space on the channel bottom surface and small in size with negligible interaction among them. Hence, incipience of clusters is essentially a parallel process; individual clusters simultaneously and independently grow in size. In this early stage of the cluster growth, once the initial number of clusters is established, the total cluster area increases linearly with time. Since the clusters are sparse, their initial growth proceeds mainly through recruitment of individual particles from the suspension flow. Thus, particle-cluster interaction is the dominant growth mechanism during the linear growth period.

The first recognized theoretical work dealing with aggregation of particles in suspensions was done by Von Smoluchowski [46]. The approach taken by Smoluchowski was to model the aggregation process as an irreversible reaction. In such a process, aggregates of i and j particles are treated as separate species reacting with a rate constant K_{ij} to form a single aggregate consisting of $i+j$ particles, i.e. the product species. Summing over all such reactions among all

aggregates of all sizes yields the Smoluchowski equation, Equation 1, for the concentration, c_k , of aggregates of k particles. The time derivative of c_k is given in terms of the concentrations, c_i , c_j and c_k , of aggregates of i , j and k particles, respectively, and the rate constant for the given combination of two species.

$$\frac{dc_k}{dt} = \frac{1}{2} \sum_{i+j=k} K_{ij} c_i c_j - \sum_i K_{ik} c_i c_k \quad (1)$$

The first term on the right-hand side of Equation 1 accounts for the increase in c_k due to aggregation of clusters and/or individual particles to form a single aggregate of k particles. The second term on the right-hand side accounts for the decrease in c_k due to further aggregation of clusters consisting of k particles into larger species. This yields a system of coupled equations (one for each aggregate size) that must be solved simultaneously. This model is greatly simplified by assuming only two species in the aggregation process: isolated particles in a suspension flow with a concentration $N(t)$ (per unit volume), and clusters along the channel with a concentration N_C (per unit volume). Under these assumptions, the Smoluchowski equation reduces to [22]:

$$\frac{dN(t)}{dt} = -N(t)N_C K \quad (2)$$

where K is the kernel representing the rate of aggregation of individual particles to existing clusters. Assuming aggregation forms clusters with random close-packed particles, the volume growth rate of an average cluster is given by the following kinematic relationship:

$$\varphi_R \frac{dV_C(t)}{dt} = -\frac{V_P}{N_C} \frac{dN(t)}{dt} \quad (3)$$

where $\varphi_R=0.64$ is the void fraction for spherical particles in random close-packed formation, V_C is the averaged cluster volume, and $V_P=\pi d^3/6$ is the single particle volume with d being the

particle diameter. Combining Equations 2 and 3 yields an equation governing the growth rate of the averaged cluster volume:

$$\frac{dV_C(t)}{dt} \approx -\frac{V_P}{\varphi_R N_C} \frac{dN(t)}{dt} = \frac{V_P}{\varphi_R} N(t) K \quad (4)$$

During the initial phase of cluster growth, the number of isolated particles per unit volume is much larger than the number of clusters per unit volume in the channel, N_C ; thus, the particle concentration in suspension varies slowly in time and can be considered quasi-steady with $N(t)=N_0$, N_0 being the initial particle concentration. The growth rate coefficient β , representing the rate of cluster area (volume) growth with time, is then defined as:

$$\beta \equiv \frac{1}{N_0} \frac{dV_C(t)}{dt} \approx \frac{V_P}{\varphi_R} K \quad (5)$$

The exact nature of the kernel K is unclear but K can be obtained from Equation 5 based on experimental data. In orthokinetic aggregation, it is equal to the shear strain rate S multiplied by the capture volume, i.e. $K \approx S \lambda^3$, where λ is a length scale characterizing the size of the capture volume. In our case, the size of the capture volume depends not only on the cluster size and the balance of forces involved but also on the channel height.

2.1.2 Microchannel Design and Fabrication

Microchannels with dimensions of $h=15 \mu\text{m}$ in height, $w=1 \text{ mm}$ in width, and $l=30 \text{ mm}$ in length were designed to carry out the experimental program. The dimensions were chosen to provide a fully-developed, two-dimensional flow. Polydimethylsiloxane (PDMS) was used as the construction material because of its high transparency and easy fabrication process employing a standard molding technique. A brief fabrication process is shown in Figure 1(a). The channel

mold was fabricated using a silicon substrate using standard photolithography and etching techniques.

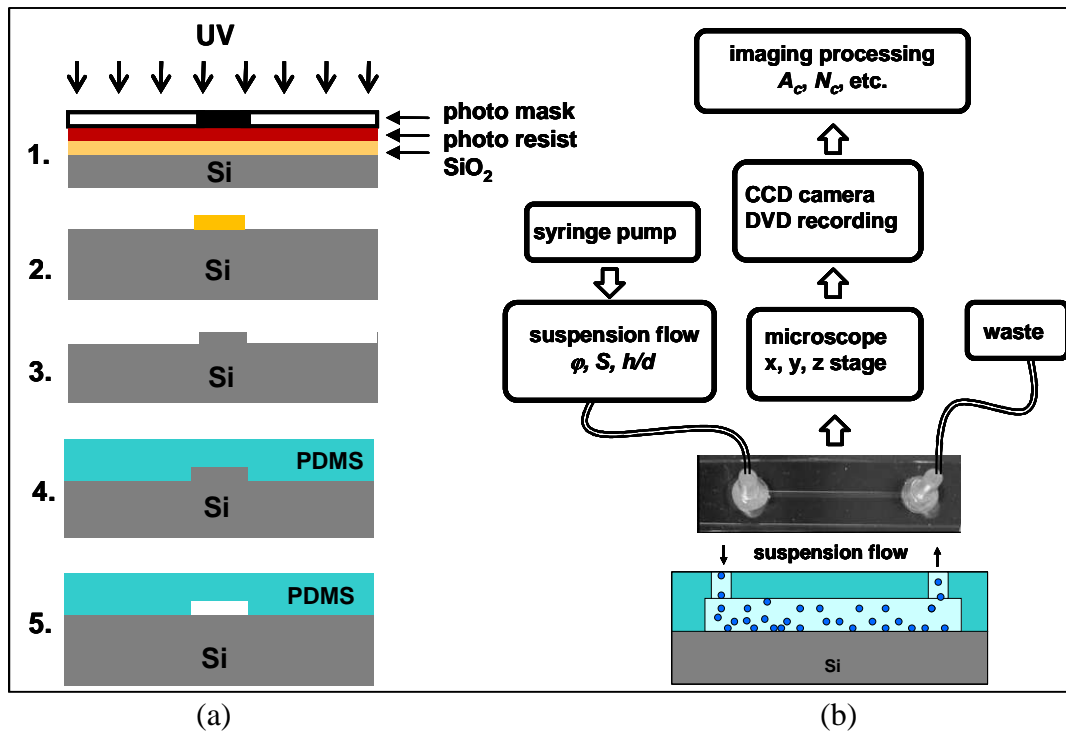


Figure 1 – Schematics of (a) microchannel fabrication steps, and (b) experimental setup. Microchannel fabrication employed standard photolithographic techniques to create a silicon mold from which channels were cast in PDMS. Channels were capped with silicon and observed under a microscope while particle suspension flow was in progress.

The PDMS channels were capped with a silicon substrate immediately after air-plasma treatment of both bonding surfaces. Flow adapters for connecting the external fluid system were bonded at the channel inlet and outlet to complete the device fabrication process. The devices were heated to approximately 100°C for a minimum of one hour before conducting experiments in order to allow the plasma treatment effects to subside. An image of a typical microchannel device is shown in Figure 1(b).

2.1.3 Experimental Program

Suspensions were obtained by diluting electrosterically neutral polystyrene microparticles in deionized water. A syringe pump was used to drive the suspension flows in the microchannels with a controlled flow rate. Digital video and images of the cluster evolution along the channel were collected throughout the duration of each experiment.

The study was conducted parametrically by independently varying the following three parameters: shear strain rate S , void fraction ϕ , and channel-height to particle-diameter ratio h/d . Void fraction, defined as volume of suspended particles divided by the total suspension volume, was controlled by dilution of the stock particle suspensions. Void fractions spanned one order of magnitude from 0.001 to 0.01. The shear strain rate S was controlled through the volumetric flow rate Q via the pump. A 2-D wall shear strain rate is used to calculate the shear strain rate: $S=6Q/wh^2$, where Q is the volumetric flow rate, w is the channel width and h is the channel height. The shear strain rate ranged from approximately 740 to 11100 s^{-1} . Particles of four different diameters were used (1.5, 3, 5 and 7.5 μm), corresponding to channel-height to particle-diameter ratios of $h/d=10, 5, 3,$ and 2 ($h=15 \mu\text{m}$). The reference experiment was conducted with parameters as follows: $\phi=0.001, S=7400 \text{ s}^{-1}$ and $h/d=10$.

The data of interest are the total cluster area growth with time along the entire channel. The measurements were acquired in the form of digital image sets of the cluster areas at various time intervals. Each set was then processed using ImageJ (NIST) and MATLAB software to quantify the total cluster area and number of clusters.

2.2 CERASOME FUNCTIONALIZATION

2.2.1 Cerasome Formation

Several stages are involved in synthesizing the organotrialkoxysilane lipids as described elsewhere [47]. Cerasomes can then be realized in aqueous media through a combination of sol-gel reaction and self-assembly of the synthesized lipids to yield bilayer vesicles with a siloxane network on the surface [40], as schematically illustrated in Figure 2. The siloxane network on their external surface provides the required surface properties for subsequent chemical processes. Specifically, the silicon atoms allow many of the processes developed for silicon substrates to be applied for manipulation of the cerasome properties.

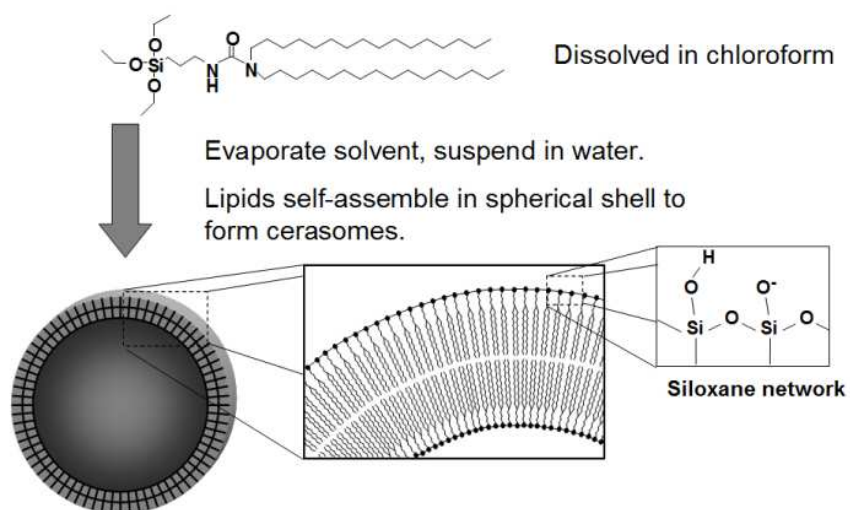


Figure 2 – A schematic illustration of cerasome formation from organotrialkoxysilane lipids. Dissolved lipids were deposited on the walls of a glass vessel as the solvent evaporated. The dried vessels were filled with DI water and subjected to ultrasonic excitation. Detached lipids suspended in water and self-assembled to form the hollow spherical structure of the cerasome. Spontaneous cross-linking at the lipid head groups occurred over a subsequent period, yielding the structurally robust, lipid-bilayer vesicle that was the fully-formed cerasome.

For the purposes of this work, cerasomes were obtained from another research group. The morphology of the obtained cerasomes was examined using scanning electron microscopy (SEM) to verify their successful formation, as well as for later comparison with functionalized cerasomes. A small volume of the cerasome suspension was dropped on the surface of a silicon die. The suspending DI water in the sample was air-dried at room temperature, and the specimen was prepared for imaging using standard techniques. A typical SEM image of the cerasomes is shown in Figure 3(a). The cerasomes are seen to be roughly spherical in shape with a diameter ranging from 200 nm to 500 nm. Figure 3(b) shows a close-up image of a well-formed cerasome prior to functionalization. The external surface is seen to be very smooth, which demonstrates that the structure is a self-assembled and closed membrane of lipid bilayer as opposed to an agglomeration of lipids or fragments of a lipid bilayer.

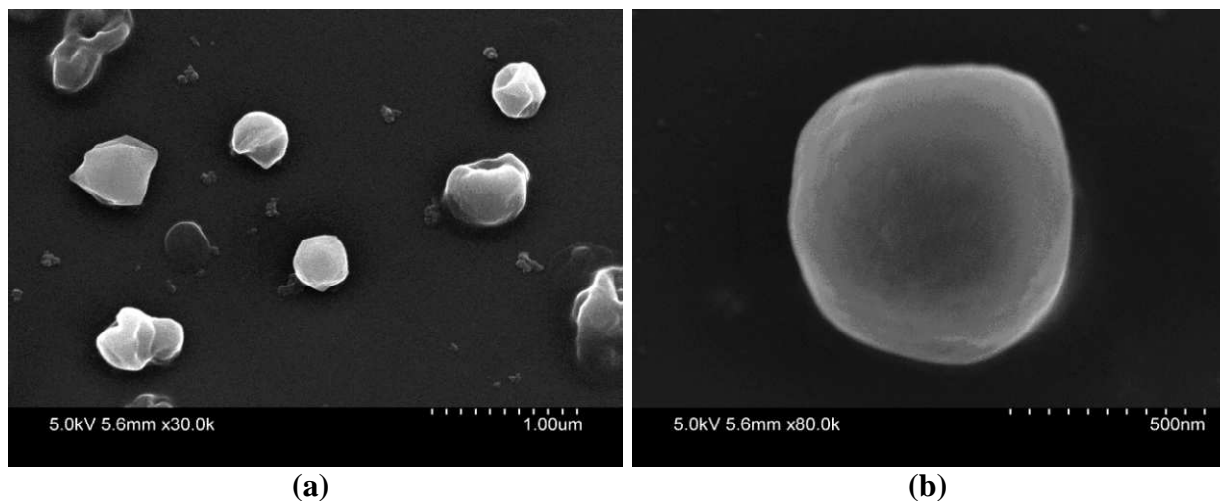


Figure 3 – SEM images of cerasomes after formation and prior to functionalization.

As-fabricated cerasomes vary in size over a wide range. The size distribution of cerasomes in a suspension was obtained utilizing the dynamic light scattering (DLS) technique. Figure 4 shows the size distribution of an original cerasome sample obtained from the DLS analysis.

Cerasomes with a certain size can be obtained using size-exclusion filtration or separation columns. As an example, the size distribution of a sample is shown in Figure 4, where a 200 nm-range sample was collected from a separation column.

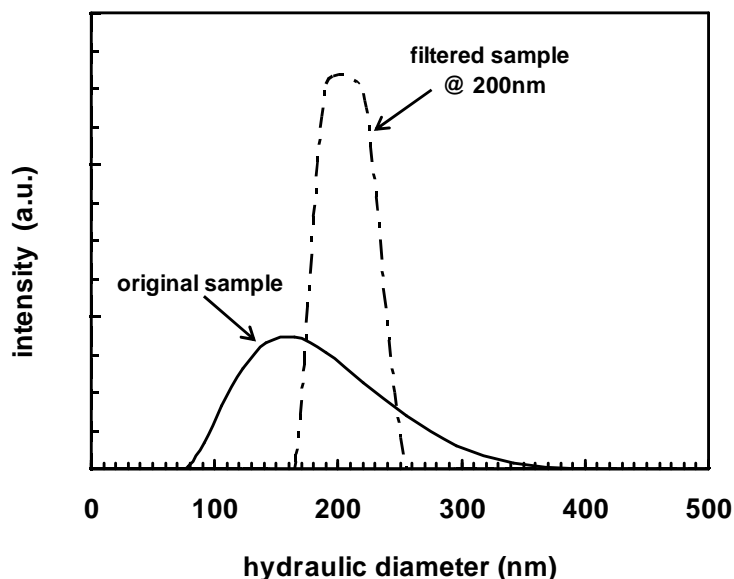


Figure 4 – Examples of cerasome size distributions of an original sample and a filtered sample measured by dynamic light scattering. Credit: Dr. Linan Jiang

Clearly, the majority of the cerasomes are less than 500 nm in diameter, as seen in Figure 4. However, it is difficult to observe these cerasomes using standard microscopy techniques. Since the cerasome surface properties of interest are independent of size, larger particles 500-1000 nm in diameter were selected for demonstration of the functionalization process.

2.3 PARTICLE-CELL INTERACTION IN AN ORBITALLY-MIXED SUSPENSION

Due to the high cost of cerasomes and inherent difficulties in working with them, silica particles were employed to mimic the cerasomes in the studies of particle-cell interaction. The

epithelial cell adhesion molecule (EpCAM) is a transmembrane protein that is over-expressed in many circulating tumor cells but absent in normal blood cells [48]. This makes EpCAM a good candidate for a target receptor. Hence, the EpCAM-expressing human breast carcinoma cell line BT-20 was used. Accordingly, EpCAM antibodies were used as the targeting ligands.

Utilizing methods to be described (see also [45]), anti-EpCAM molecules were immobilized on 1.6 μm diameter silica particles. Prescribed volumes of the stock suspensions of functionalized particles and target cells were diluted and combined in wells on a typical 24-well plate, then mixed using a shaking incubator. Parameters held constant throughout all experiments include the total suspension volume per well (500 μl), the number of cells per well (10000), temperature (25°C), and orbital speed (400 rpm). The suspending medium was 1X CMF PBS (calcium and magnesium-free phosphate-buffered saline) with 2% fetal bovine serum.

Upon completion of mixing, each well was sampled. Samples were deposited on glass slides where the liquid spread to a thin layer. Allowing the sample to spread to a thin layer minimized the possibility of false counts due to particle sedimentation on cells below. The samples were examined under a standard bright-field microscope.

2.3.1 Image Analysis and Quantification of Particle-Cell Binding

To quantify the degree of particle-cell binding, the fractional cell-surface coverage f is used and is defined as the number of particles bound to the cell divided by the geometrically-dictated maximum number of particles that could fit on the cell (e.g. a surface coverage value of $f=1$ does not imply that 100% of the cell surface is bound to particles, but that no single section of exposed cell surface is large enough to accommodate another particle without displacing adjacent bound particles).

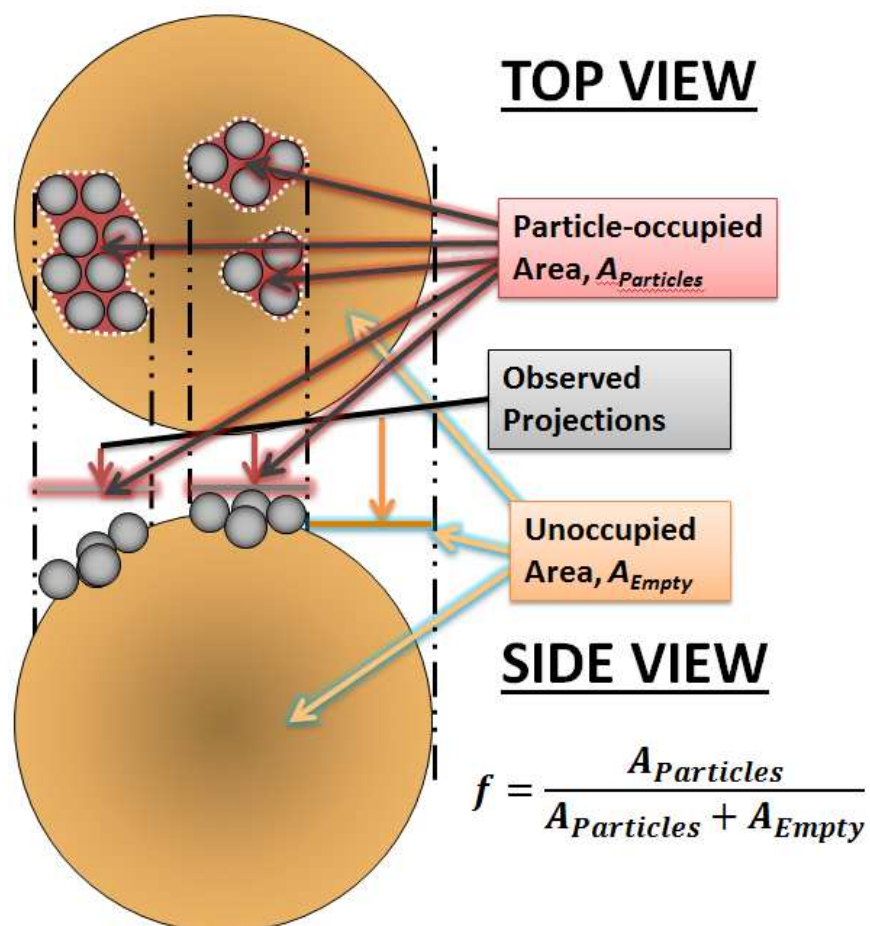


Figure 5 – A schematic illustration of the method used to quantify fractional cell-surface coverage f due to particle-cell binding. The fractional cell-surface coverage is calculated as the ratio of the projected area on the cell surface for which further particle binding is prohibited by size-exclusion to the total projected area of the spherical cell.

For each cell analyzed, the surface coverage measurement was performed by constructing a z-stack of images taken at focal planes distributed across the height of the cell. With the aid of ImageJ (NIST) image processing software, stack layers were individually analyzed for particles and the occupied area was marked. Logical statement commands and a convolution of the marked stack layers provided the total occupied area while also preventing false counts due to overlap. Multiple cells from each sample were analyzed, and samples for each set of parameters

were collected from repeated experiments under similar conditions. The data shown in the figures to follow result from the aggregate (i.e. each data point represents multiple cells coming from multiple experiments). The error bars are estimated based on the calculated standard deviation of the distribution of fractional cell-surface coverage values for that set of experimental conditions.

2.4 PARTICLE-CELL INTERACTION IN A MICROCHANNEL

Several steps were required both before and after execution of flow programs in order to obtain satisfactory data. The major steps consisted of microchannel fabrication, immobilization of cells, particle flow, cell fixation and channel detachment. Data acquisition was then performed in a way similar to what is described in Section 2.3. This section details or references all steps taken when conducting experiments.

2.4.1 Microchannel Fabrication

PDMS microchannels with dimensions of height $h=100\ \mu\text{m}$, width $w=1\ \text{mm}$ and length $l=30\ \text{mm}$ were fabricated from a silicon mold as previously described. Glass microscope slides were cleaned in a piranha solution (1:1:5 parts 1.5 M H_2SO_4 , H_2O_2 , and DI water) at 80°C for 20 minutes. Following rinsing with DI water, the slides were stored in 0.1 M H_2SO_4 . These storage conditions ensured that the glass was appropriately protonated and remained free of contaminants.

If a higher operating pressure was required, the cleaned glass slides were rinsed with ethanol and immersed in a 1% APTES in ~100% ethanol solution for 5 min. The slides were rinsed thoroughly with ethanol and DI water, and cured for 1 hr at 110°C . Upon completion of

curing, the slides were immersed in 0.1 M sulfuric acid to remove contaminants that may have adsorbed during curing. Silanization of the glass created a highly hydrophobic surface against which the (also highly hydrophobic) PDMS was pressed. The contact interface between the two hydrophobic materials increased the allowable operating pressure by increasing the net work of adhesion required for water to penetrate between the two surfaces.

Immediately before capping the PDMS channels, slides were removed from the storage solution, rinsed with 95~100% ethanol and dried with compressed air. Bonding was achieved by simply placing the PDMS channel on the glass, inspecting for particulates and air bubbles, then applying light pressure. Channels could then be stored by covering the outer surface (closing holes) with adhesive tape. Regardless of which glass was used, the bond with the channel was maintained by Van der Waals and electrostatic forces, leaving it completely reversible using only physical means.

2.4.2 Functionalized Particle Suspension Preparation and Handling

Much of the discussion to follow may seem trivial as may tasks such as measuring concentration. This is not so and improper handling often yielded a bad batch of particles that would produce unusable results, and could not be recovered. In short, mishandling the suspensions rendered the entire time preparing for and executing experiments essentially wasted. Preparation was involved and this could mean as much as two full days. So what follows is here for posterity as well as to explain the reasons behind relatively large error that will be seen later.

A method of functionalizing certain types of micro/nanoparticles with antibodies was developed and is described in Section 4.2.1. This method was utilized to functionalize silica microparticles approximately 1.6 μm in diameter with anti-EpCAM antibodies. Functionalization

of particles for a given experiment was completed the same day as said experiment was performed. The newly functionalized particle suspension, henceforth referred to as the stock suspension, was supplemented with 0.5% BSA and kept at $\sim 4^{\circ}\text{C}$ prior to use.

Particle concentration was measured using a hemocytometer. This measurement technique offered an accuracy of $\pm 10\%$ at the very best. Therefore, multiple measurement-dilution steps were required in order obtain particle concentration within a particular desired range; the measured concentration of the stock was useful only as a rough estimate.

When needed for an experiment, the appropriate quantity of stock suspension was sequestered and washed three times with PBS to remove BSA from the suspending fluid. If this step were not performed, the particle would aggregate quickly and it was visually evident that clusters were a major constituent of the suspension flowing through the channel.

Despite the low protein-adhesion materials and continuous mixing of the suspension, depletion of the particles in suspension (via adhesion to various surfaces or clustering and sedimentation) remained a significant issue. To illustrate, the particle concentration measured from the syringe was not observed to remain constant over the full duration of preparation, execution, etc. of experiments and in fact often dropped by a factor ~ 3 (that is not to say it changed significantly while conducting the experiment itself, i.e. executing the flow program).

With a measurement device (hemocytometer) that is accurate to $\pm 10\%$ at best, it was crucial to minimize other sources of error, of which there were many, between measured and true values of particle concentration. Since the problems with maintaining a constant particle concentration over a long period of time were never fully resolved, steps were taken to prevent them from affecting results. Samples of the particle suspension were collected for concentration

measurement immediately before and after experiments (i.e. before and after every flow program). When working with functionalized microparticle suspensions, even seemingly simple tasks such as sampling for concentration measurement can be significantly complicated by the various particle adhesion phenomena. Samples collected in, for example, something as inert as a polypropylene centrifuge tube will be rendered useless within a matter of minutes due to particles adhering to the walls of the tube. One common practice is to rinse the vessel with a dilute solution of a protein such as BSA which will itself adsorb onto the vessel walls, but proteins in the suspending medium can cause particles to adhere to each other causing the formation of large clusters by way of hydrophobic interactions (which cannot be counted for particles). In order to achieve an acceptable accuracy level in a concentration measurement, the sample must be stabilized from aggregation be it with other particles or onto vessel wall etc. and for the most part, monodisperse to allow reliable counting. Accordingly, samples were deposited directly from the tubing into polypropylene microcentrifuge tubes that already contained a dispersant. A frequently used dispersant that has shown to be particularly effective with nano-scale organic-inorganic composites is sodium citrate [49], which proved to be very well-suited for the task. A 0.1% w/v aqueous solution used as the suspending medium performed well. A small amount of 10X solution was put in the tubes prior to sample collection. As long as the concentration was not diluted below .1% w/v, the samples could be stored indefinitely without being compromised. Prior to concentration measurement, the samples were exposed to ultrasonic excitation until completely monodisperse in order to allow accurate counting. Finally, the pre- and post-experiment sample concentrations were compared. If significantly different, the experiment was thrown out. If not, the measured values were averaged.

2.4.3 Cell Detachment and Preparation for Experiments

As before, experiments used cells from the EpCAM-expressing human breast carcinoma cell line BT-20. Cells were maintained at 37°C in a 5% CO₂-enriched incubator. Eagle's minimum essential media (EMEM, ATCC) supplemented with 10% fetal bovine serum (FBS) and 1% penicillin streptomycin (pen-strep) was used for culture and changed every ~3 days. Prior to an experiment, the cells were washed then incubated in 0.5% trypsin-EDTA solution at 37°C for 4 min. Complete culture media was then added and the cell suspension was aspirated 8 times. Repeating the same cell detachment procedure was necessary to minimize variations in the cells from batch to batch.

2.4.4 Microchannel Functionalization and Cell Immobilization

Cells were immobilized in the microchannels by covalently bonding antibodies to the glass and utilizing the antibody-antigen affinity to hold the cells in place. The chemical processes involved were similar to those depicted in Figure 14. Constructed channels were removed from any storage packaging and treated with air plasma at ~500 mTorr for 5 min to produce surface hydroxyl groups on the glass (and oxidize the silanized surface inside the channel, if applicable). With channels already constructed, the contact surfaces of the PDMS and the glass were not exposed to plasma and the adhesion of the two surfaces remained reversible. The plasma-treated channels were filled with 1% APTES in ethanol and periodically flushed with fresh APTES-ethanol solution for 5 min. Following the allotted reaction time, the APTES-ethanol solution was washed from the channel with ethanol for 10 min. Channels were emptied (not dried) with compressed air and cured for 10 min at 110°C. This shortened cure time served to minimize contaminants adsorbed during curing and was sufficient since these reaction conditions

generated an APTES layer of sufficiently low thickness. Channels were allowed to cool to room temperature, washed briefly with PBS, filled with 5% glutaraldehyde (Grade 1, Sigma-Aldrich) in PBS and allowed to react at room temperature for a minimum of 2 hr. The channels were thoroughly washed of glutaraldehyde using PBS. Channels were then filled with antibody solution (anti-EpCAM) at a concentration of 100 $\mu\text{g/ml}$ and incubated for 15 min at room-temperature. Great care was taken to prevent any air from entering the channels once the antibodies were introduced since denaturation of the antibodies could result in only the cells expressing the highest levels of EpCAM being immobilized. Upon completion of incubation, channels were washed with continuous flow of PBS for 5 min. The final wash step was performed to ensure that only covalently bound antibodies remained on the channel surface and that the buffer within the channel contained no free antibodies. Reversibility of the various glutaraldehyde-amine reactions [50] mandated a continuous flow during washing to ensure that any quantity of antibodies released into the buffer contained within the channel thereafter had negligible effect on cells.

Shortly before immobilization, cells suspensions were checked for concentration and cell clustering by infusing a small sample into a dummy channel. The cell suspensions were then aspirated and/or diluted accordingly and resampled until the spacing and clustering were satisfactory. Cells were pipetted gently into the channels through the outlet to avoid an excess of cells where the particles were to be introduced. Immediately after infusing the cell suspension into the channel, any excess at the inlet or outlet was removed to equalize liquid levels and stop flow inside the channel while the cells settled down to the bottom surface. Cells were incubated inside microchannels at room temperature for 5 min before particle suspension flow was

initiated. The length of this incubation period was seen to have an effect on particle-cell binding so it was controlled as precisely as possible; channels in which cell incubation time deviated by more than 10% of the prescribed value were considered unsuitable for use.

2.4.5 Experimental Apparatus

The experimental apparatus setup with the completed microdevice, connections and equipment is shown schematically in Figure 6. The suspension was contained in a 3 ml syringe (Becton Dickinson) mounted horizontally in a PHD Ultra syringe pump (Harvard Apparatus). The syringe was fitted with a 25-gauge hypodermic needle secured by a luer-lock connection. The needle was sheathed in Intramedic tubing (Becton Dickinson) of 0.28 mm inner-diameter. The size difference created a press-fit-like connection capable of withstanding high working pressures while permitting no detectable leakage. This particular tubing was used due to its low protein adhesion properties and particle aggregation on the inner surface of the tubing was not an issue during experiments. The other end of the tubing was cut at an angle of $\sim 45^\circ$ and inserted directly into the inlet of the microchannel. The microchannel device was secured on the microscope stage during experiments.

The syringe containing the particle suspension also housed a neodymium-based disc approximately 3 mm in diameter and 1.5 mm thick that was externally manipulated in order to mitigate sedimentation. The high magnetization of the disc allowed it to be manipulated from afar using a typical magnetic stir bar attached to a continuously-variable speed rotary tool that was situated above the syringe. The rotary tool setup allowed the disc to be positioned at the top of the inside of the syringe while it was rotated; this important detail of the setup allowed the suspension to be mixed while avoiding resuspension of the sediment at the bottom of the syringe.

This effect was desirable since proper speed settings created a relatively large difference in the stability of suspension constituents; large particle clusters could be permitted to fall out of suspension and settle on the bottom of the syringe while the rest of the suspension remained relatively stable. Since the syringe was situated horizontally, only stable suspension was pumped through the microchannel.

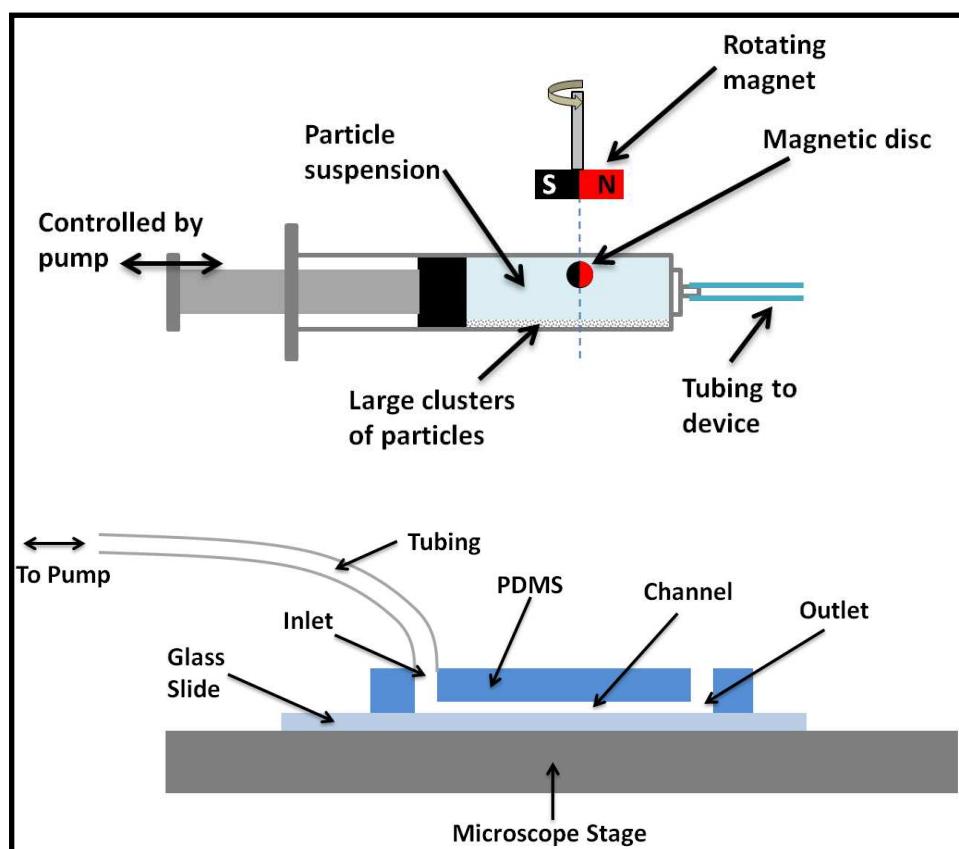


Figure 6 – Schematic of completed experimental apparatus. Magnetic actuation provided stirring of the suspension in the syringe (to) allowing for longer periods of stability. The channel (bottom) was supplied by the syringe which was driven by a pump.

Tubing was connected shortly before initiation of flow, and the particle suspension flow commenced immediately upon completion of cell incubation within the channel. A down-stream location near to the exit of the channel was observed under a standard bright field microscope

while particle suspension flow was in progress. The flow was inspected for large particle clusters, air bubbles, freely-moving cells, dust, etc. which would disqualify that experiment from inclusion in the data. Following completion of the flow program, the entire apparatus was left untouched for ~1 min to ensure ligand-receptor bond networks between particles and cells had reached steady-state and to allow particles to settle to the bottom of the channel. The inlet tube was carefully removed while observing the channel under the microscope. Detachment of particles from cells, mobile cells, or any violent motion observed were grounds for disqualification of the experiment.

2.4.6 Experimental Program

Three parameters that clearly impact the particle-cell binding process are particle concentration, incubation time, and shear strain rate of the suspending fluid. The particle concentration was controlled by dilution. Particle suspension concentrations were measured with a hemocytometer and several dilution-measurement steps were performed before the desired concentration was obtained.

The particles were liable to bind to various surfaces such as the insides of tubes, syringes and pipette tips during handling and storage. Furthermore, despite continuous mixing, some sedimentation inside the supply syringe was observed. It was therefore necessary to sample the suspension immediately before and/or after an experiment, and measure the concentration at that time. Even with reliably collected samples obtained both before and after an experiment, the measured values of the particle concentration nevertheless came with a high degree of uncertainty due to the measurement device alone ($>\pm 10\%$).

The shear strain rate and incubation time, however, could be controlled much more precisely. Since the shear strain rate is directly proportional to the flow rate, it was controlled via the flow rate setting on the syringe pump. Similarly, the incubation time was simply the time that the particle suspension was allowed to flow through the channel and was controlled by setting the flow rate and flow volume accordingly.

The three parameters were varied independently with particle concentration ranging from roughly 10^3 to $3 \times 10^4 \mu\text{l}^{-1}$; shear strain rate from $300 \sim 3000 \text{ s}^{-1}$, and incubation time ranging from 20 to 1000 s. With the given channel geometry, these shear strain rate and incubation time ranges correspond to flow rates of 0.5 to 5 $\mu\text{l/s}$ and flow volumes of 50 to 1000 μl .

In addition to being within a range proven feasible in vivo [51], the particle concentration range was chosen to achieve sufficient particle-cell binding within the allotted time to provide statistically significant data while also avoiding undesired inter-particle interactions that resulted in particle clustering. For concentrations over $3 \times 10^4 \mu\text{l}^{-1}$, clustering was a significant problem leading to aggregation in the channel inlet where there are bends in the flow.

The range of flow rates was dictated by the experimental setup; rates below $\sim 0.5 \mu\text{l/s}$ allowed for sedimentation in the supply tubing and to an extent, the channel itself. Increasing the flow rate past 3 $\mu\text{l/s}$ showed little difference in results and increasing past 5 $\mu\text{l/s}$ was seen to detach some cells. Presumably, cells with weaker EpCAM expression would detach first thereby corrupting results. Hence, higher flow rates were not only unnecessary but undesirable as well. Within the range 0.5~3 $\mu\text{l/s}$, few cells were dislodged and significant non-uniformity in the height-wise particle concentration profile due to sedimentation was not an issue [52,53]. Despite

experimental limitations, the range of shear strain rate cover the majority of what is present in the human body [54].

The reference set of flow rate and flow volume values (i.e. the values of Q and V corresponding to data that was used across all parameter studies) was selected to be as follows: $Q=1.0 \mu\text{l/s}$, $V=100 \mu\text{l}$. The aforementioned difficulties in accurately prescribing the particle concentration precluded the use a single value of N_p as a reliable reference. Hence, characterization of the full parameter space using an orthogonal array of Q , V , and N_p values was not logistically possible; the investigation was performed using an orthogonal array of Q and V and a set of N_p values for each (Q,V) pair.

2.4.7 Cell Fixation, Channel Disassembly, and Specimen Preparation

Once a channel was disconnected from the tubing, a small quantity of 5% glutaraldehyde in PBS was deposited near (not in) the channel inlet, where it was drawn into the inlet via surface tension of extraneous liquid. The flow that resulted was driven only by gravity and pressure differences resulting from surface curvature of the deposited glutaraldehyde solution. Hence, the flow rate was very low and did not disrupt the cells or particles while the glutaraldehyde solution replaced the remaining liquid inside the channel. The channels were kept in closed petri dishes at room temperature during fixation and additional fixative was periodically deposited at the inlets to maintain a slight flow through the channel. Glutaraldehyde was used as the fixative due to its superior cross-linking capabilities [50] which were realized by allowing a minimum of 1 hour reaction time at room temperature.

Following fixation, the entire microchannel device was submerged in a bath of PBS where the PDMS was gently removed from the glass substrate. With the device disassembled, the glass

slide was placed in PBS containing ~.01% BSA for several minutes. This step allowed protein to adsorb onto the glass slide which aided in liquid retention during imaging. The slide was removed from the bath and placed in a dish containing only enough PBS to reach over the top of the slide; the hydrophilicity of the adsorbed protein prevented the sample from drying out while the small volume of PBS resulted in a thin liquid layer that was advantageous for imaging purposes. Image acquisition was performed as before. Analysis of images was performed in a similar way as before, except particles were counted individually rather than the area measured. Counting the particles offered a more robust method of outlier detection than did measuring the surface coverage since measurements were integer values [55]. When an experiment met all criteria to be included in data analysis, however, outliers demanding removal were rarely seen.

3. PARTICLE-CELL INTERACTION MODELING

A theoretical model of particle-cell interaction was developed in parallel to experiments and has been adapted based on various results. The foundations of the model are developed here. Modifications made to the model, based on experimental results, are described as said results are presented.

3.1.1 Generalized Form of the Mathematical Model

The basis of the model is a simple kinematic relationship accounting for adsorption and desorption of particles to/from the cell surface. Consider a single cell in a shear flow amongst a population of many particles. Without regard to the factors influencing the respective rates k_1 and k_2 , adsorption and desorption of particles affect the total number ν of bound particles (to the cell surface) as follows:

$$\frac{d\nu(t)}{dt} = k_{on}N_p[1 - f(t)] - k_{off}\nu(t) \quad (6)$$

Here, N_p is the particle concentration (#/volume), the $1-f$ term accounts for space on the cell surface already occupied by particles, and k_{on} and k_{off} are unknown rates which may or may not be functions of time, shear strain rate, particle concentration, etc. Dividing by the geometrically-limited maximum number of particles that can fit on a cell ν_{max} , and expressing each rate as a product of a constant and an unknown function of the various parameters yields the equation describing the fractional cell-surface coverage evolution in time in its most general form.

$$K_{on}g_1(t, S, N_p, \dots) \equiv \frac{k_{on}}{v_{max}} \quad (7)$$

$$K_{off}g_2(t, S, N_p, \dots) \equiv k_{off} \quad (8)$$

$$\frac{df(t)}{dt} = K_{on}g_1(t, S, N_p, \dots)N_p[1 - f(t)] - K_{off}g_2(t, S, N_p, \dots)f(t) \quad (9)$$

The general solution of Equation 9 is

$$f(t) = \exp\left(-\int [K_{on}g_1 + K_{off}g_2]dt\right) \times \int_0^t [K_{on}g_1 \cdot \exp(\int (K_{on}g_1 + K_{off}g_2)dt')]dt' \quad (10)$$

where the arguments of $g_1=g_1(t,S,N_p,\dots)$ and $g_2=g_2(t,S,N_p,\dots)$ have been omitted. Without knowledge of the dynamics of the system, Equation 10 is of little use. However, once sufficient information of the system dynamics is known, Equation 10 may be easily evaluated (albeit perhaps numerically) for a solution. Throughout this work, the functions g_1 and g_2 will take on various forms and may not be referred to explicitly so as to avoid conflicting definitions.

3.1.2 Ligand-Receptor Bond Dynamics

To gain some knowledge of the functions $g_1(t)$ and $g_2(t)$, one must examine the dynamics of the adhesive forces. Ligand-receptor bonds form and rupture at rates k_R^{on} and $k_R^{off}(F)$, respectively [56,57]. The bond rupture rate is force-dependent while the formation rate is constant and non-zero when the ligand and receptor are within a critical distance of each other. The force-dependence of the rupture rate is as follows [56]:

$$k_R^{off} \equiv k_R^0 \exp(F_R/F_D) \quad (11)$$

$$F_D = k_B T / x_c \quad (12)$$

The number of ligand-receptor bonds between a particle and cell will then follows

$$\frac{dN_{RB}}{dt} = k_R^{on} N_{RA} - \langle k_R^{off} \rangle N_{RB} \quad (13)$$

Strictly speaking, the rate of bond rupture between particle and cell (i.e. the average k_R^{off}) is *not* computed in terms of the arithmetic mean of the ligand-receptor bond force, but this makes a good first approximation and is sufficient for illustrative purposes. Under this approximation,

$$\langle k_R^{off} \rangle \approx k_R^0 \exp\left(\frac{F_{PC}}{N_{RB} F_D}\right) \quad (14)$$

and

$$\frac{dN_{RB}}{dt} \approx k_R^{on} (N_R - N_{RB}) - k_R^0 N_{RB} \exp\left(\frac{F_{PC}}{N_{RB} F_D}\right) \quad (15)$$

Two important pieces information may be obtained directly from the above equation without need for a solution; the steady state value and a characterization of the rate. The nonlinearity prohibits description of the system with the traditional time constant (since the off rate k_R^{off} is itself an implicit function of time), but upper and lower bounds on the rate are easily obtained. The response time characterizing the *instantaneous* state of system evolution (i.e. it is *not* a time constant) is

$$\tau_{LR}(N_{RB}) \approx \left[k_R^{on} + k_R^0 \exp\left(\frac{F_{PC}}{N_{RB} F_D}\right) \right]^{-1} \quad (16)$$

The upper bound on τ_{LR} is

$$\tau_{LRmax} = \frac{1}{k_R^{on} + k_R^0} \quad (17)$$

This corresponds to an unloaded state for which the exponential vanishes, the system is linear, and τ_{max} is exactly the time constant of the *unloaded* system dynamics. Order of magnitude values from literature show that the upper bound on the time scale is on the order of milliseconds [56].

The lower bound of the residence time of a particle near a cell can be established using the unperturbed flow field. So long as the local velocity profile is approximately linear,

$$\tau_{res,min} = \frac{L}{d_{pc}S}$$

where L is the length scale characterizing the effective capture radius due to multiple ligand-receptor encounters.

The second piece of information to be gained from Equation 15 is the force-dependent steady-state value of the number of ligand-receptor bonds. This value may be computed using the transcendental equation for N_{RB} obtained by setting the derivative equal to zero.

$$N_{RB} = \frac{N_R k_R^{on}}{k_R^{on} + k_R^0 \exp\left(\frac{F_{PC}}{N_{RB} F_D}\right)} \quad (18)$$

N_{RB} is degenerate due to the nonlinearity in the governing ODE, and can be shown that degeneracy occurs at a critical force value, above which a steady state cannot be achieved and the bonds will continue to rupture until the particle is free. A qualitative depiction of this is shown in Figure 7.

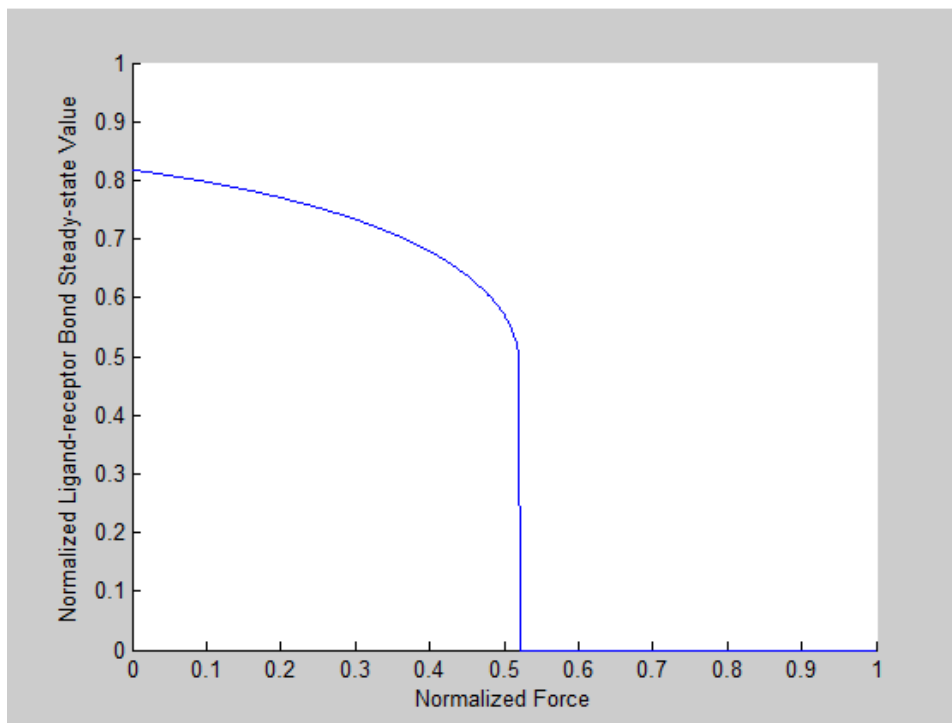


Figure 7 – Qualitative depiction of steady-state N_{RB} value dependence on binding force illustrating degeneracy owing to the existence of a critical force value.

The implications of these results are that the ligand-receptor bonds between any bound particle and cell can be assumed to be at steady state. In this case, particle adsorption and desorption rates are functions of the steady state binding force which is in turn proportional to the surface density of functional receptors. This will be revisited in discussions concerning particle desorption that are to come.

4. RESULTS AND DISCUSSION

4.1 CLUSTER AREA GROWTH

Continuous aggregation of particles results in cluster growth with its volume increasing with each joining particle. It is very difficult to measure the actual cluster volume since the 3-D shape of each cluster inside the microchannel is required. On the other hand, it is relatively easy to measure the projected area of each cluster utilizing still images from recorded video clips of the evolving clusters in the microchannel. The area of each cluster observed in the microchannel was measured under different experimental conditions by varying the control parameters φ , S and h/d . The sum of the measured cluster areas provides the time-dependent total cluster area, A_T , which is plotted in Figure 8 for all tested experimental conditions. During the initial cluster evolution, the growth of the total cluster area with time is indeed linear as evident by the best-fit curves for each set of measured data.

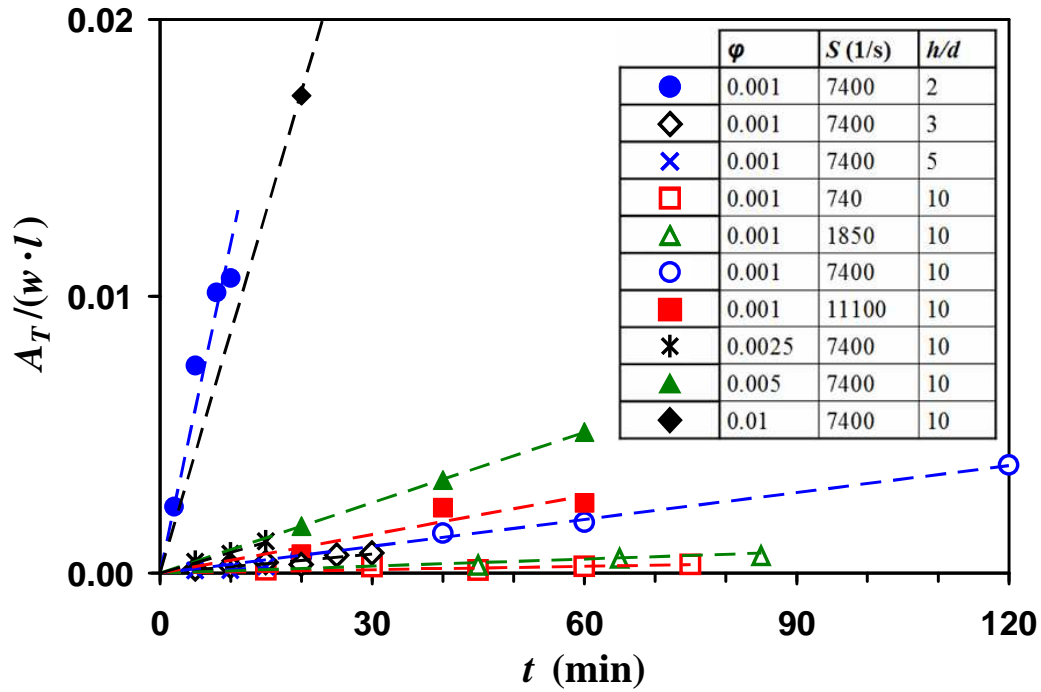


Figure 8 – Total cluster area growth in time under various experimental conditions.

4.1.1 Suspension Void Fraction Effect

The total cluster area growth, $A_T(t)$, is the result of a combination of new cluster formation (starting with a single particle) and the growth of existing clusters. From the observations in this study, we found that the vast majority of cluster incipience occurs during the very early stages of aggregation, and the increase in cluster area is predominantly due to particle-cluster interactions. Therefore, the averaged cluster area can be deduced from the total cluster area as follows: $A_C(t) = A_T(t) / N_{TC}$; N_{TC} is the total number of clusters evolving along the channel, which is assumed to be quasi-steady after the initial cluster formation stage.

To explore the effect of suspension void fraction on the growth rate of the averaged cluster size, dV_C/dt , the relationship between the averaged cluster volume and its projected area is required. The simplest assumption is that of a cluster extending the height of the channel which

is constant in time, $V_C = h \cdot A_C$, such that the cluster volume is directly proportional to its area. While this could be a valid assumption at a later time for clusters with size on the scale of the channel height, it cannot be valid for shorter time scales as particles gradually form a bridge spanning across the channel height. The next simplified assumption is a cluster of hemispherical shape where the cluster height is proportional to the square root of the cluster area, *i.e.* $V_C \propto A_C^{3/2}$, leading to:

$$\frac{dA_C}{dt} = A_C^{-1/2} \frac{dV_C}{dt} \approx \frac{\beta}{\sqrt{A_C}} N_0 \quad (19)$$

Under the assumption of quasi-steady particle concentration in the flowing suspension, the initial particle concentration can be substituted by the void fraction $N_0 = \phi/V_P$; thus, the averaged cluster area growth rate can be re-written as follows:

$$\frac{dA_C}{dt} \approx \frac{\beta}{V_P \sqrt{A_C}} \phi \quad (20)$$

Equation 20 implies that the averaged cluster area growth rate, in the initial growth regime, is proportional to the suspension void fraction. To examine this relationship, experiments were conducted under identical conditions while varying only the void fraction, *i.e.* the shear strain rate and channel-height to particle-diameter ratio were held constant at $S = 7400 \text{ s}^{-1}$ and $h/d = 10$, respectively. The measured averaged cluster area growth rate is depicted in Figure 9 as a function of the suspension void fraction. A linear curve fit yields a correlation coefficient of over 0.98, suggesting the cluster area growth rate increases linearly with the suspension void fraction; following Equation 20, this necessarily means that the growth rate coefficient is independent of the void fraction, *i.e.* $\beta \neq \beta(\phi)$. A similar finding has been reported for particle aggregation under

different conditions [22,23]. Based on the results depicted in Figure 9, Equation 20 indicates that the growth rate coefficient is proportional to the square root of the cluster area, i.e. $\beta \propto A_C^{1/2}$.

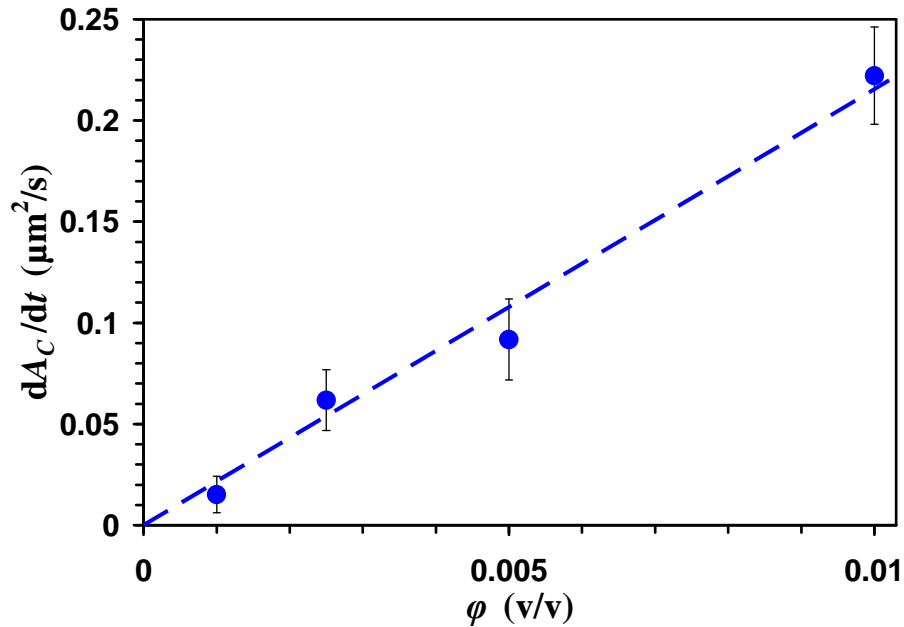


Figure 9 – Average cluster area growth rate as a function of suspension void fraction ($h/d = 10$, $S = 7400 \text{ s}^{-1}$).

4.1.2 Effect of Shear Strain Rate

In orthokinetic flocculation, the kernel is given by $K \approx S\lambda^3$. Thus, substituting this kernel into Equation 5 yields:

$$\beta \propto d^3 S \lambda^3 \quad (21)$$

The capture volume length scale depends on the operating conditions including, among others, the shear strain rate, $\lambda = \lambda(S, h, d, \dots)$. Therefore, the relationship between the growth rate coefficient and the shear strain rate is not linear, but rather complicated; in several similar, yet not identical, particle aggregation studies, a power-law relationship has been suggested in the form of $\beta \propto S^a$ [10,22-23].

In order to examine this power law relationship, experiments were conducted under identical conditions holding the suspension void fraction and the channel-height to particle-diameter ratio constant at $\varphi=0.001$ and $h/d=10$, respectively, while varying only the shear strain rate S . The averaged cluster area growth rate was measured and, based on Equation (20), the growth rate coefficient was calculated as follows:

$$\beta = \frac{V_P A_C^{1/2}}{\varphi} \frac{dA_C}{dt} \quad (22)$$

Since the growth rate coefficient is a weak function of time, $\beta \propto t^{1/2}$, growth rate coefficients were estimated from a time-integral average of the calculated values based on Equation (22). The results are logarithmically plotted in Figure 10 as a function of the applied wall shear strain rate. A power-law fit to the experimental data suggests an exponent of $a=0.9\pm 0.1$ describing the dependence of the growth rate coefficient on the shear strain rate. The relatively large experimental error in the estimated power law relationship is mainly due to the large uncertainty in the actual cluster volume, since only the projected cluster area is measured. This exponent value is within experimental error of the value of 0.82 predicted by the modernized flocculation theory for aggregation rate of equal-diameter particles in an unbounded domain [58]. On the other hand, an exponent value of 1.0 was reported based on an experimental study of particle clogging of micro constrictions [23]. While these values are in general of order 1, an experimental and theoretical study on the aggregation of paramagnetic particles into chains yielded a similar power law with an exponent equal to 0.25 [22]. Equation 21 suggests that the exponent value may be equal to 1.0 only if the capture volume is independent of the shear strain rate; otherwise, it would assume a different value depending on the relationship between the

capture volume and the shear strain rate which, in turn, depends on the detailed experimental conditions.

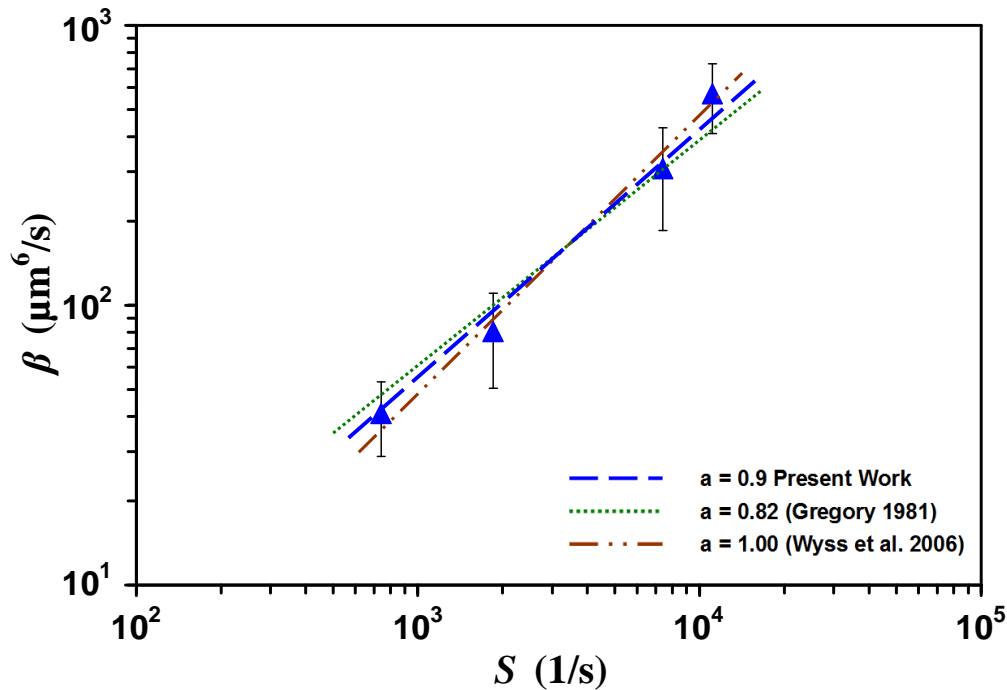


Figure 10 – Growth rate coefficient as a function of suspension shear strain rate (blue dashed line), ($h/d = 10$, $\varphi = 0.001$). The other lines are presented for comparison with findings from broadly similar work done by others.

4.1.3 Effect of Channel-Height to Particle-Diameter Ratio

Particle aggregation in suspension flows is a very complicated phenomenon depending on many parameters. To simplify the problem, early studies considered macro-scale systems, in which solid boundaries are far apart such that particle-surface interaction is negligible. Thus, in such systems, only the effects of suspension void fraction and shear strain rate are significant. However, in microchannels, all suspended particles are close to solid boundaries. As a result, particle-surface interaction becomes a dominant mechanism, and it has to be considered in the particle dynamics analysis. Since the microchannel width and length are typically much larger

than its height, the microchannel height h is the length scale of choice for characterizing particle-surface interaction. In a study of microchannel blockage phenomena, the critical particle concentration needed for blockage of microchannels was reported to depend on $(h/d)^{-3}$ [59]. In another work, the critical particle flux required for microchannel clogging was found to depend on $(h/d)^{-4}$ [23]. These exponent values demonstrate the critical role of channel height in particle aggregation in microsystems, which requires further studies both theoretically and experimentally.

As already indicated, the capture volume length scale λ dependency on h and d is yet to be resolved. Therefore, following previous studies, a power-law relationship is assumed between the cluster growth rate coefficient and the channel-height to particle-diameter ratio in the form $\beta \propto (h/d)^b$. Experiments were conducted varying h/d through a range of 2 to 10 while keeping both the shear strain rate and the suspension void fraction constant at $S=7400 \text{ s}^{-1}$ and $\varphi=0.001$, respectively. The resulting growth rate coefficient, deduced from the measured cluster area growth rate, is logarithmically plotted in Figure 11 as a function of the channel-height to particle-diameter ratio. The power-law fits well with all the data except that for $h/d=2$. The best-fit curve for $h/d>2$ is obtained with an exponent value of $b=-3.5\pm 0.25$.

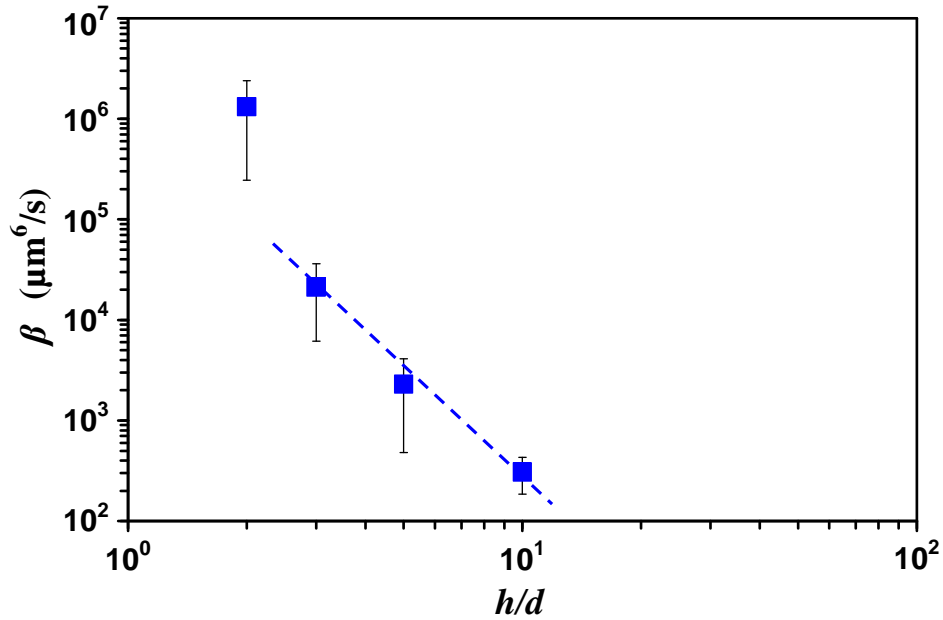


Figure 11 – Growth rate coefficient as a function of channel-height to particle-diameter ratio ($\varphi = 0.001$, $S = 7400 \text{ s}^{-1}$). The data point for $h/d=2$ is not the result of the interactions of interest herein and is therefore omitted from the fit.

The data for $h/d=2$ deviated from this relationship. In fact, different phenomena were observed during the experiment. Aggregates began to form at the channel inlet from a very early time stage, less than 5 min after starting to drive the particle suspension through the microchannel. Large pre-formed clusters were periodically observed to enter the channel inlet and attach onto the channel bottom surface. An example of such an event with a cluster much larger than an individual particle is shown in Figure 12. The introduction of these pre-formed clusters to the channel results in significant discrepancies in both the pattern and growth rate of clusters compared to the cluster evolution observed for $h/d>2$. Since the growth mechanism of these clusters is not simply based on particle-cluster interaction, the cluster growth rate does not follow the model process described by Equation 2. Hence, the data for $h/d=2$ are excluded from the curve fitting. Further observations show that the pattern of the clusters formed on the

microchannel surface depends largely on the channel-height to particle-diameter ratio. As shown in Figure 13(a) for the case of $h/d=10$, after one hour of suspension flow time, isolated clusters are observed on the channel surface that are small in overall size with a comparable length scale in both streamwise and spanwise directions. In contrast, as shown in Figure 13(b) for the case of $h/d=2$, chain-like clusters are observed. The clusters appear much bigger in overall size with a significantly larger streamwise than spanwise length scale. In addition, most of the clusters are physically interconnected. Thus, for $h/d=2$, the growth of clusters inside the channel involves not only particle-cluster but also cluster-cluster as well as cluster-wall interactions, and these interactions are not within the scope of this study.

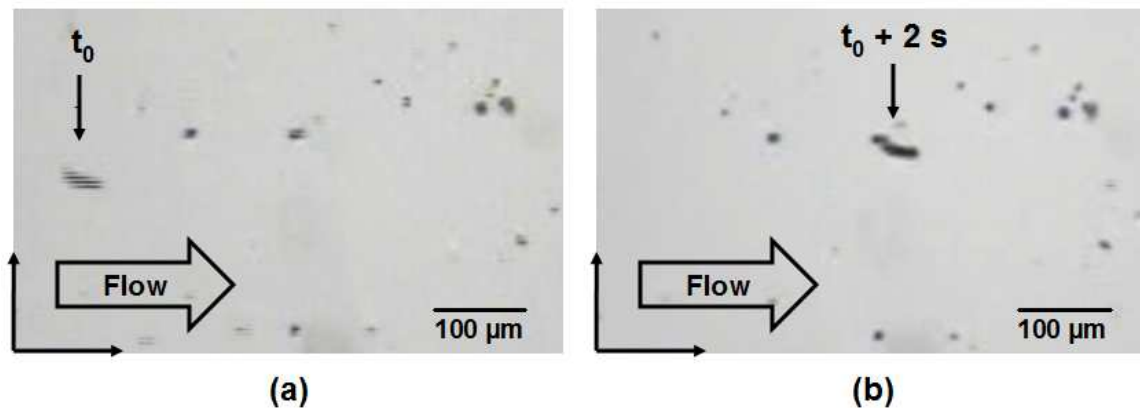


Figure 12 – Images of a pre-formed cluster in an experiment with $h/d = 2$: (a) moving with the suspension flow at the microchannel inlet region, and (b) attached on the microchannel bottom surface a short distance downstream ($\phi = 0.001$, $S = 7400 \text{ s}^{-1}$)

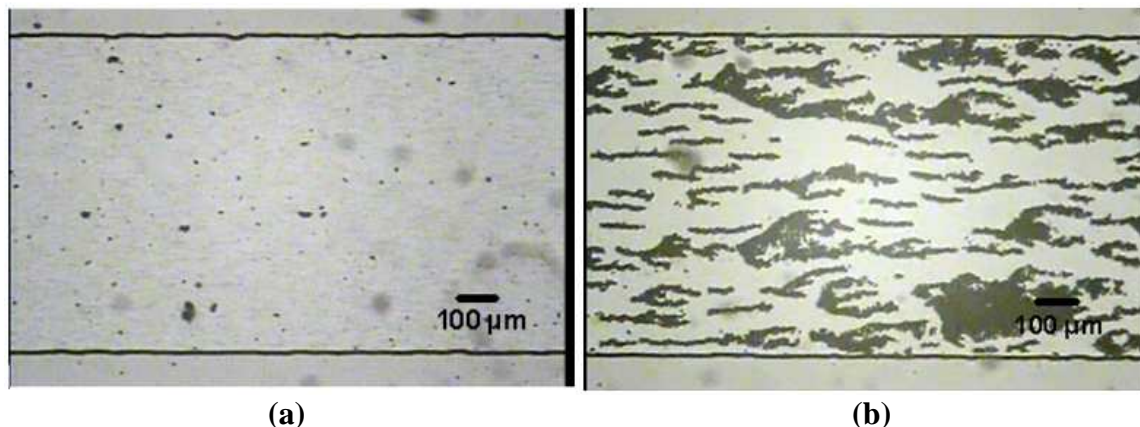


Figure 13 – Representative images of cluster patterns due to different h/d : (a) $h/d = 10$, and (b) $h/d = 2$ ($\varphi = 0.001$, $S = 7400 \text{ s}^{-1}$)

Interestingly, while the exponent value of -3.5 identified in this work is not in agreement with any of the published values, it is nonetheless within the reported range between -3 and -4. Clearly, this exponent depends to a large extent on the detailed experimental conditions. Furthermore, the data used to establish the effect of h/d were obtained by varying only the particle diameter d while keeping constant the channel height h . Consequently, how the channel height independently affects the capture volume, which in turn affects the cluster growth rate, cannot be resolved from these data.

4.2 CERASOME FUNCTIONALIZATION

4.2.1 Cerasome Functionalization with Antibodies

To immobilize targeting ligands on a cerasome surface, we followed a protocol that has been successfully utilized in immobilizing antibodies on silica nanoparticles since both cerasomes and silica particles feature surface silanol groups. A similar immunoassay has been detailed in functionalizing microchannels with antibodies [60,61], and the functionalization process used in this work is illustrated in Figure 14. Cerasomes were immersed in a 1% (vol/vol)

3-aminopropyltriethoxysilane (APTES)-acetone solution for 30 min at room temperature. The silanized surface was then activated with a solution of 2% (vol/vol) glutaraldehyde in deionized (DI) water for two hours to promote a Schiff-base reaction between the amine and aldehyde groups. After thoroughly washing with DI water, the cerasomes were incubated in a recombinant protein G solution at a concentration of 50 $\mu\text{g/ml}$ in 1 \times phosphate buffered saline (PBS) at approximately 4°C for three hours. In order to block excess silanol sites, the cerasomes were washed and then immersed in bovine serum albumin (BSA) solution of 2 mg/ml concentration for one hour at room temperature. Following a thorough wash with 1 \times PBS, the assay was completed by incubating the cerasomes with fluorescently tagged Cy3-anti-mouse IgG (from donkey) antibodies at a concentration of 100 $\mu\text{g/ml}$ for one hour at room temperature in a darkened environment. The cerasomes were washed once more with 1 \times PBS and stored in 1 \times PBS at approximately 4°C in the dark.

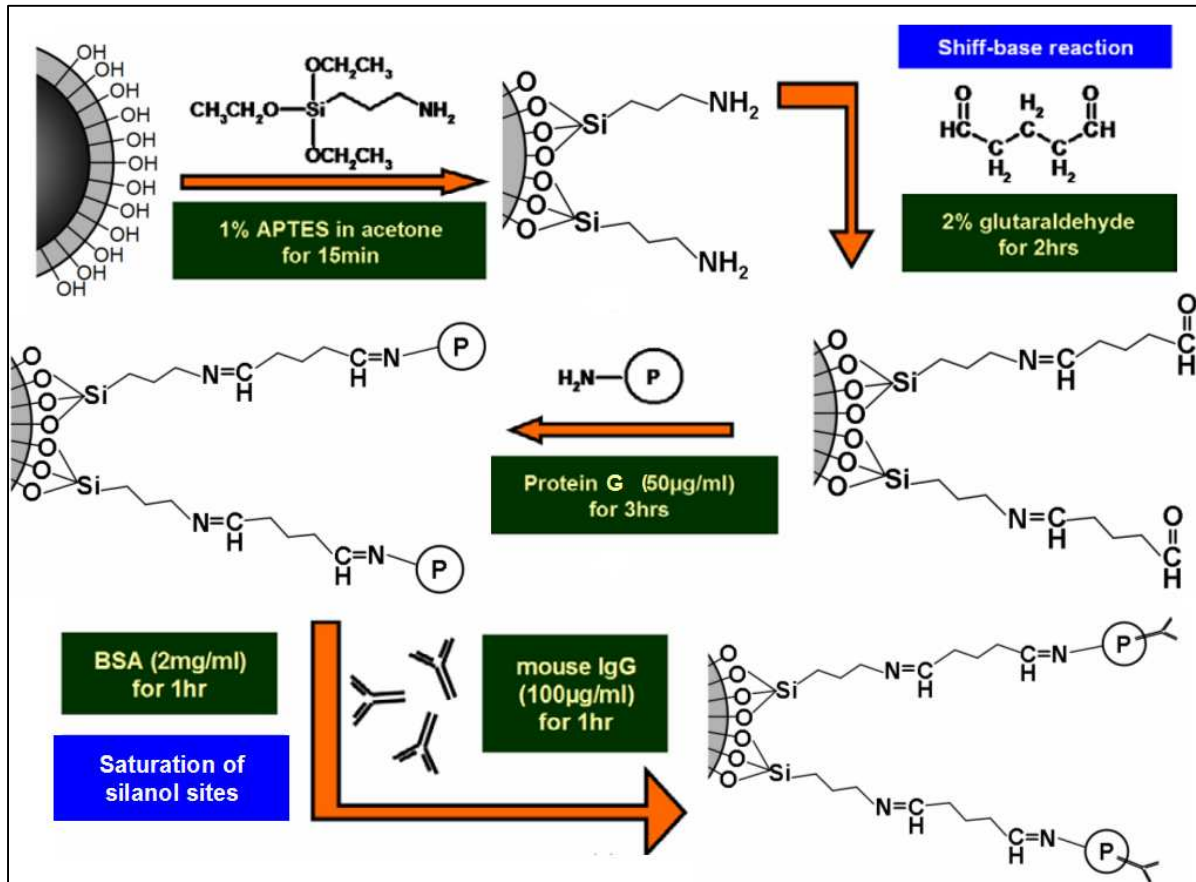


Figure 14 – A flow chart of the various major steps required in the functionalizing process.

As an alternative to this protocol, the antibody may be attached immediately following the surface activation with glutaraldehyde. The silanol and aldehyde sites are then saturated with BSA and the protein G step is omitted entirely. The glutaraldehyde solution may also be made slightly acidic to increase electrostatic repulsion between silanized particles [62] during the reaction and inhibit bridging/aggregation [24,63]. The result of this alternate protocol is that the antibodies are not oriented with the specific binding region outward [64]. As long as the target cells are Fc-blocked, however, this will not lead to non-specific binding.

4.2.2 Characterization of Bio-Functionalized Cerasomes

The fluorescently tagged antibodies were used in the assay as a means to verify the successful functionalization of the cerasomes. If the antibodies were indeed immobilized on the cerasome surfaces, then there should be an observable difference between unmodified and the functionalized cerasomes when observed using a fluorescence microscope (Nikon Eclipse 80i) with proper excitation and emission. Fluorescence microscope images of cerasomes before and after functionalization are compared in Figure 15. Images of two cerasome samples are shown under white light in Figure 15 (A1) and (B1), while those in Figure 15 (A2) and (B2) are taken at the same locations but using 550 nm excitation and 570 nm emission filters in order to detect the Cy3 labels. The images in Figure 15 (A1) and (A2), taken for unmodified cerasomes, clearly show the presence of cerasomes under white light but show no detectable fluorescence signal using the proper excitation/emission filters. The images in Figure 15 (B1) and (B2), taken for functionalized cerasomes, show a number of cerasomes under white light and fluorescence signals at identical locations using the excitation/emission filters. The results indicate that the fluorescently tagged antibodies have been successfully immobilized on the cerasome surfaces.

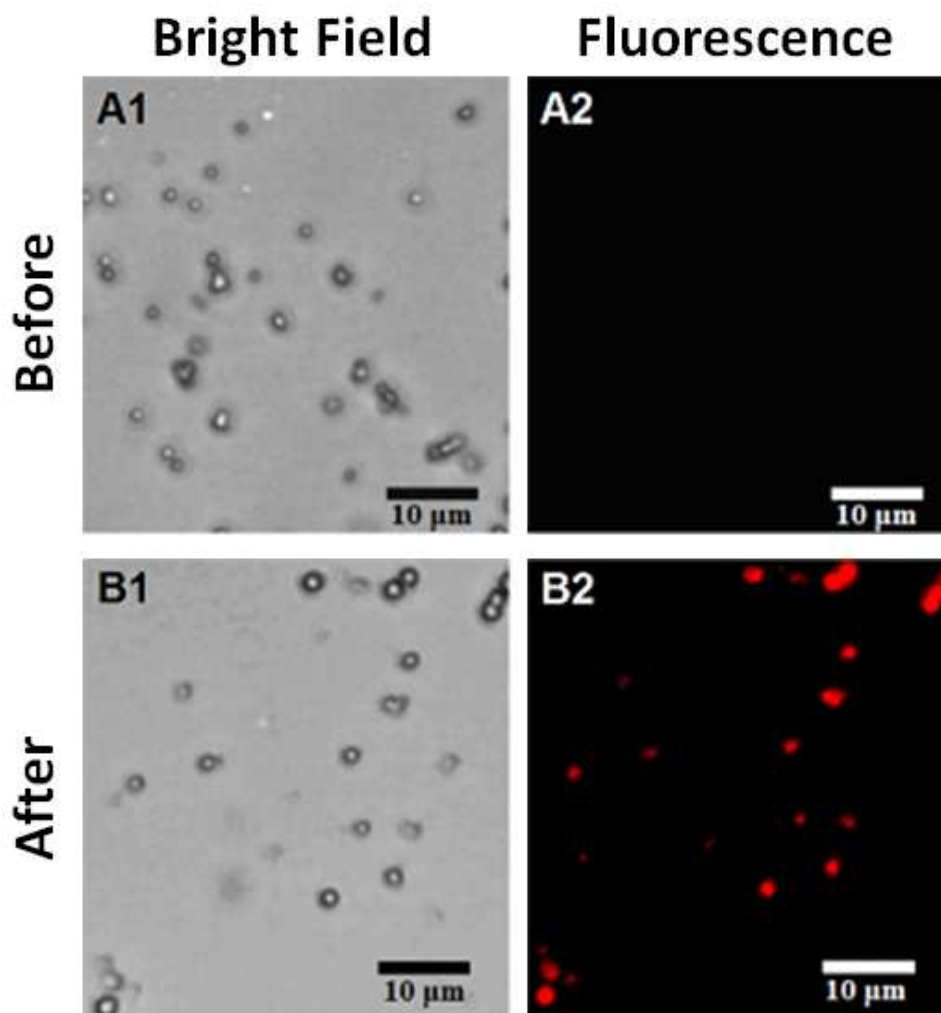


Figure 15 – Micrographs of cerasomes using bright field (A1 and B1) and fluorescence imaging (A2 and B2) taken: before (top), and after (bottom) functionalization with antibodies.

With the antibodies immobilized on the surface, the cerasomes are functionalized and have the ability of targeting specific cell types based on the receptors they express. Although anti-mouse IgG was used as an example antibody in this work, the functionalization method could be implemented to immobilize virtually any antibody on the cerasome surface. This gives the cerasomes a potential of targeted drug-delivery to specific cell types, enhancing the selectivity of the therapeutic treatment and minimizing side effects.

To examine whether the cerasomes were damaged by the successive chemical processing steps, SEM images (not shown here for brevity) of cerasomes were taken after the conclusion of the entire procedure of surface functionalization. The images, similar to the one shown in Figure 3(b), confirm that functionalized cerasomes are still intact as indicated by the retention of their spherical shape and smooth surface. The retention of the nearly spherical shape shows that the various functionalization steps have not significantly affected the morphological properties of the cerasomes in any adverse way. The smooth surface of the functionalized cerasomes, as that of the unmodified ones, indicates that the vesicle surfaces are fully-enclosed shells rather than an agglomeration. The cerasome membrane closure is a critical requirement for vesicles to be used as drug delivery vehicles since an opening would cause dispersal of any encapsulated contents into the surrounding medium.

4.2.3 Functionalized Particle – Target Cell Interaction

In order to confirm the ability of functionalized particles to specifically bind to target cells, experiments were conducted with functionalized silica microparticles and BT-20 cancer cells. The BT-20 line of cells expresses the epithelial-cell-adhesion molecule (EpCAM), which is over-expressed in many tumor cells but is absent in normal blood cells [48]. Hence, EpCAM was chosen as the target receptor in these experiments. Silica microparticles approximately 1.5 μm in diameter were functionalized with two types of antibodies: anti-mouse IgG and anti-human EpCAM. The BT-20 cancer cells were then Fc-blocked and added to suspensions of functionalized microparticles in $1\times$ PBS containing 1% FBS. Each suspension was placed in a well on a 24-well plate mounted on a shaking incubator for 20 min at 25°C. Next, the mixed suspensions were dispensed on microscope slides allowing the particles and cells to settle onto

the surface of the slides before imaging. The particle concentration was sufficiently low to prevent significant numbers of particles from settling onto the cell surfaces. Figure 16 shows typical cells from two types of particle-cell suspensions subjected to identical experimental conditions. A typical cell from the suspension consisting of particles functionalized with anti-mouse IgG and BT-20 cancer cells is shown in Figure 16(a), while a similar cell from a suspension consisting of particles functionalized with anti-human EpCAM is shown in Figure 16b. Clearly, the particles functionalized with the anti-human EpCAM result in substantial particle-cell specific binding, while the particles functionalized with anti-mouse IgG show very little particle-cell nonspecific binding. For the control group (particles functionalized with anti-mouse IgG), on the average, fewer than 10 particles were observed to be bound to a target cell; in contrast, more than a hundred particles per target cell were observed to be specifically bound for the test group of particles functionalized with the targeting ligand (anti-human EpCAM).

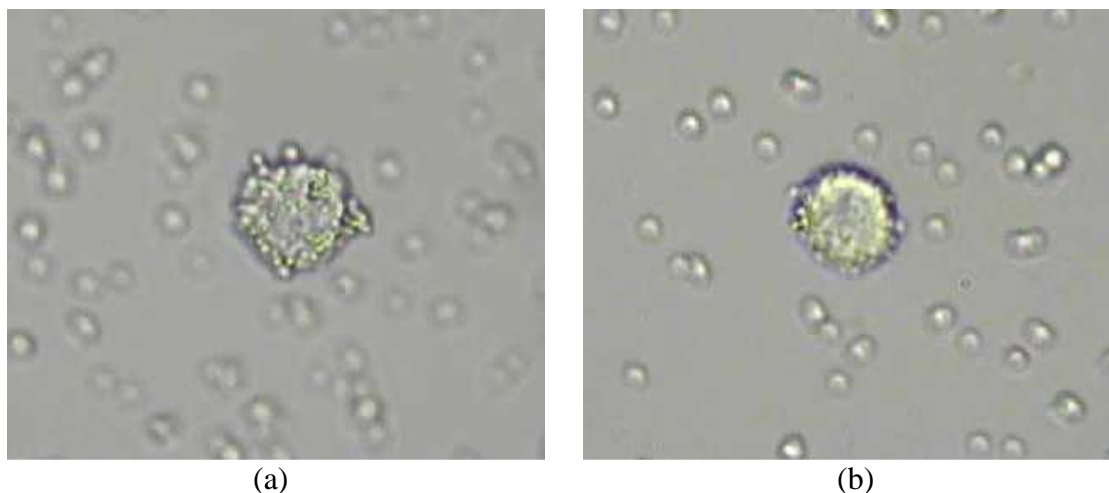


Figure 16 – A typical EpCAM-expressing target cancer cell (BT-20) after exposure to particles functionalized with: (a) the proper counter-receptor anti-human EpCAM, and (b) anti-mouse IgG, demonstrating the specific binding capabilities of the functionalized particles. All other experimental conditions were identical.

4.3 SPECIFIC INTERACTIONS BETWEEN ANTIBODY-FUNCTIONALIZED PARTICLES AND CIRCULATING TUMOR CELLS IN AN ORBITALLY-MIXED SUSPENSION

Initial experiments investigating particle-cell interaction in suspension were conducted while independently varying only the particle concentration N_p and incubation (mixing) time t . Several images of representative cells after incubation under various experimental conditions are shown in Figure 17.

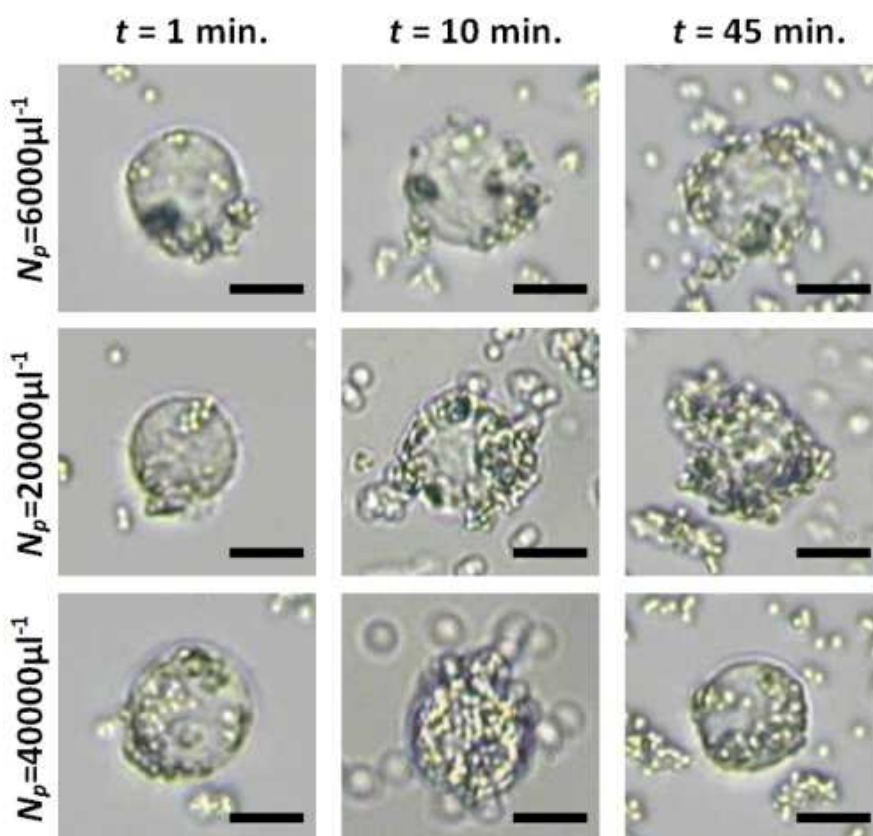


Figure 17 – Micrographs of individual cells with bound particles for cell coverage evaluation under various experimental conditions. Note: Depth-of-focus limitations preclude clear rendering of all particles in any single image. Scale bars 10 μm .

4.3.1 Effects of Incubation Time and Particle Concentration

Two important parameters affecting the interaction between functionalized particles and target cells mixed in a suspension are the incubation time and the cell/particle concentrations. Therefore, to investigate their effect on particle-cell binding, the incubation time t and particle concentration N_p were varied independently while other parameters were fixed. For a fixed incubation time, Figure 18, the surface coverage increases with increasing particle concentration. One may argue that this is to be expected since increasing the particle concentration without changing incubation time inevitably results in more particle-cell collisions and therefore more opportunities for a particle to bind to a cell. A similar argument may be made with regard to incubation time with fixed concentration. Clearly, the number of particle-cell collisions increases with incubation time. However, as seen in Figure 19, it was found that surface coverage does not necessarily increase monotonically with incubation time for a fixed particle concentration.

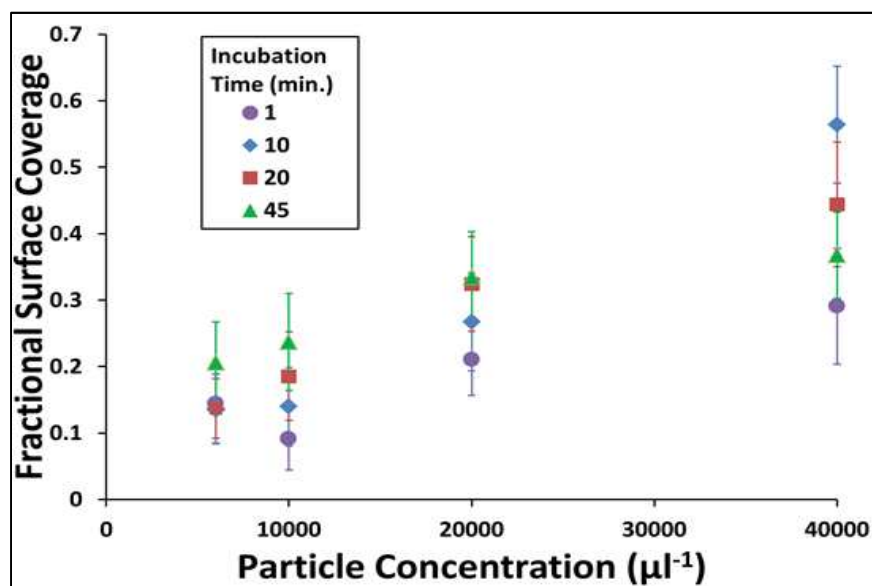


Figure 18 – Surface coverage as a function of particle concentration for various incubation times.

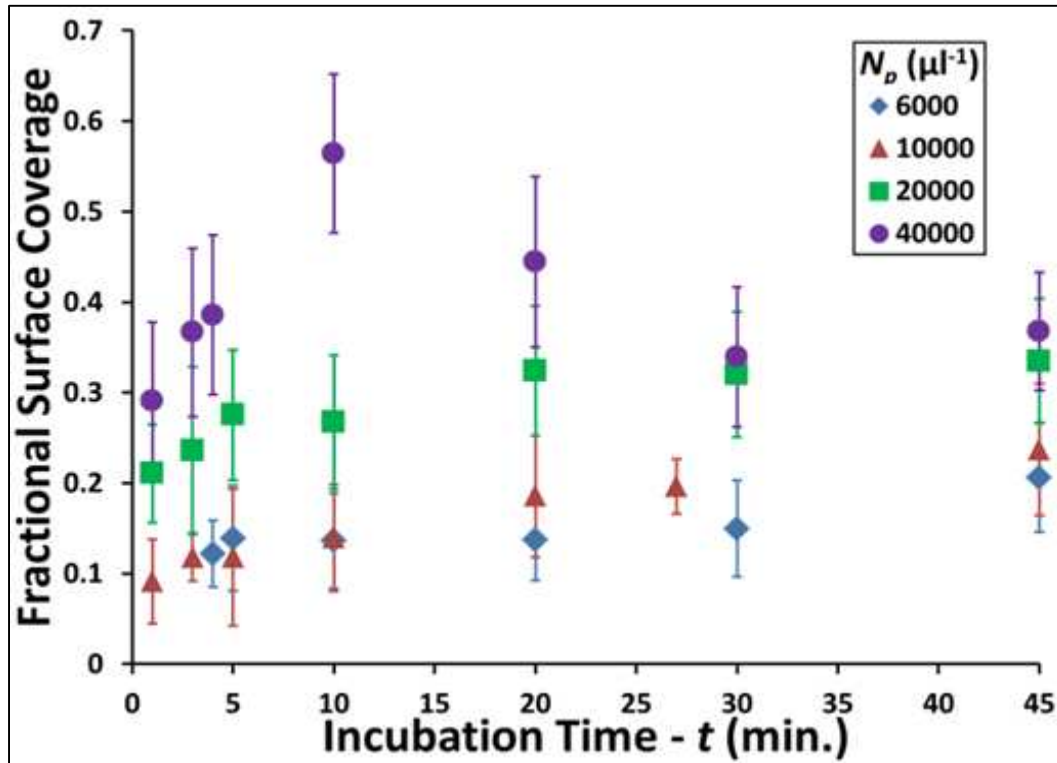


Figure 19 – Fractional cell-surface coverage as a function of incubation time for various particle concentrations.

A distinct and statistically significant maximum appears at $t=10$ min for $N_p=40000 \mu\text{l}^{-1}$. Under this relatively high particle concentration, the surface coverage exhibits a rapid increase within the initial 10 min of incubation; then, a gradual drop over the next 20 min takes place; and, finally, little to no change is observed in the final 15 min of the experiments. While the decreasing surface coverage stage is only statistically significant for $N_p=40000 \mu\text{l}^{-1}$, all particle concentrations share the other two features; a rapid increase in the initial and little change during the later stage of incubation.

Two features of the behavior depicted in Figure 19 have particularly important implications and warrant reiteration: (1) during later stages, further incubation time yields little to no change in surface coverage, and (2) there exists a set of conditions and time period during

which surface coverage decreases with incubation time. Either one of these is sufficient to show that the system dynamics cannot be described solely by adsorption (i.e., a continuous increase in the number of bound particles); hence, there must be a restricting effect(s). The former suggests the possible existence of a steady-state or equilibrium. The latter implies that there must be a mechanism for the removal of bound particles from cells. Together, these observations hint at the nature of the effects limiting particle adsorption to cells. For example, simple first-order reversible adsorption-desorption model cannot explain the overshoot that appears for high particle concentration. It is therefore necessary to investigate the effects of particle desorption and binding-affinity loss independently.

4.3.2 Particle Desorption

The effects of particle desorption were examined by first considering the basic kinetics of a reversible process, such as particle adsorption-desorption. By definition, a reversible process is characterized by two opposing effects that force the process toward equilibrium/steady-state. This was the principle upon which experiments investigating particle desorption were based; if desorption occurs, the initial condition of the surface coverage in relation to the steady-state value will determine whether the surface coverage increases or decreases in time.

Particle desorption was investigated by comparing cell coverage results from bare cells (the reference case, below steady-state), to those from cells with a sufficiently-high initial surface coverage (i.e. above the steady-state value for that particle concentration). This was done by mixing highly-concentrated suspensions of cells and particles for a very brief period before dilution. The high concentrations induced a rapid increase in surface coverage and the subsequent dilution resulted in a particle concentration of $N_p=6000 \mu\text{l}^{-1}$ (the lowest used) while

all other parameters were kept identical to those in the experiments previously described. With the exception of the brief mixing before dilution, the experiments were conducted as before and thus provided the high initial condition required for comparison. The results are summarized in Figure 20. The reference case shows a short-lived increase of surface coverage with incubation time, followed by no significant changes for the remaining duration of the experiment. This is clearly evident in Figure 20, from which one may make a rough estimate of the steady-state value.

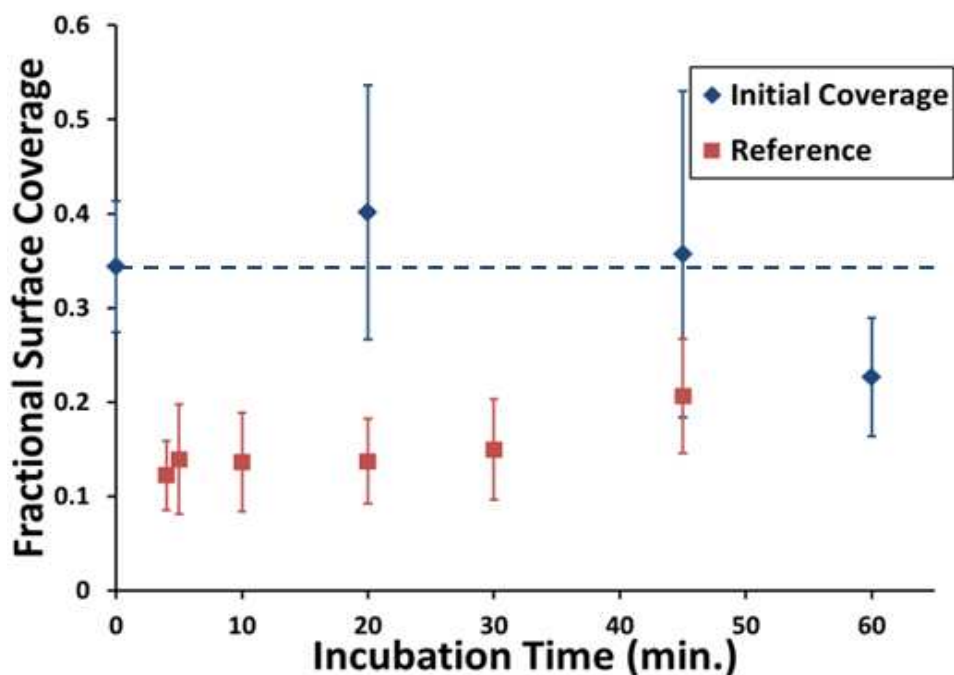


Figure 20 – Comparison of surface coverage between cells with an initial coverage to those of standard experiments, wherein cells had no initial coverage, for $N_p=6000 \mu\text{l}^{-1}$ showing the lack of significant particle desorption with incubation time.

The low particle concentration was selected in order to minimize further particle-cell binding (for cells with initial coverage) after the start of incubation, as well as to ensure that the initial coverage was significantly greater than any value observed in the reference case (i.e. well

above any steady-state). With initial coverage being the sole difference, particle desorption should result in the data sets tending toward an intermediate value. This is not observed; the coverage level of cells with initially-bound particles does not change significantly over the 45 min time-period of the experiments. Hence, it seems that particle desorption is negligible and, consequently, cannot explain the results presented in the previous section.

4.3.3 Loss of Binding Affinity

The fact that the cells undergo changes during experiments is irrefutable, but the pertinent issue to address was whether or not any of these changes affect the particle-cell interactions. To investigate any such effects, cells were initially incubated in suspension without particles. Particles were added to the suspensions after various time delays for additional incubation of 20 min. For a given particle concentration, the only parameter varied was the cell incubation time prior to the introduction of particles. The results plotted in Figure 21 show that any changes in the cell that occur over the time frame of the experiments have negligible impact on the resulting surface-coverage. It is thus evident that changes in the cells during incubation cannot account for the surface-coverage peak observed at the high particle concentration.

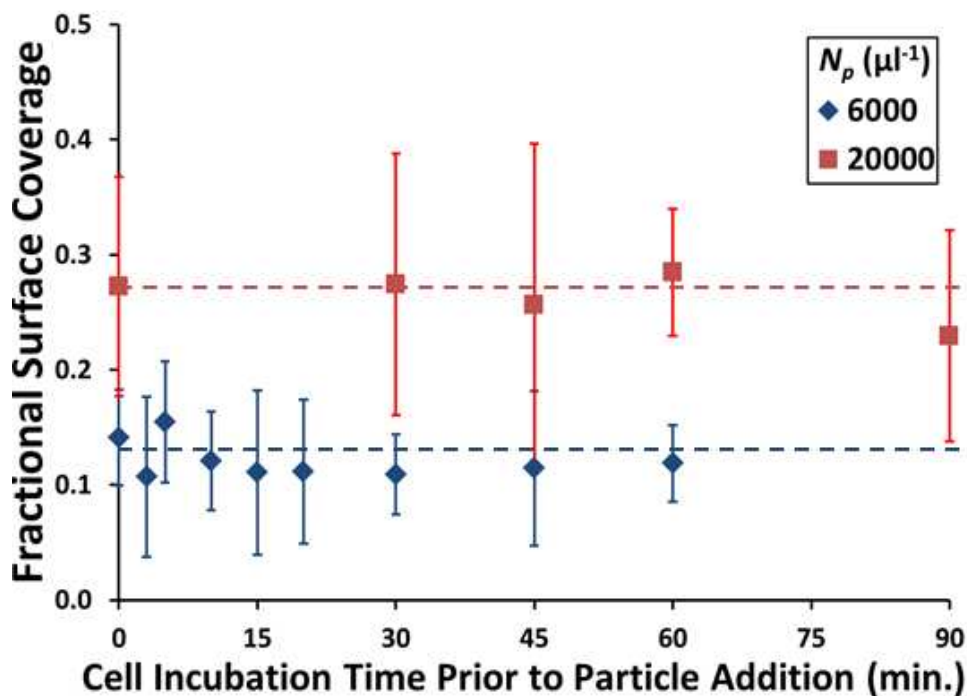


Figure 21 – Surface coverage as a function of cell incubation time prior to introduction of particles with subsequent particle-cell incubation time fixed at 20 min. for particle concentrations $N_p=6000$ and $20000 \mu\text{l}^{-1}$. Cell incubation time without particles does not affect the particle adsorption rates; effects related to cell viability loss are negligible.

4.3.4 Cell-Particle-Cell Interactions

Cell-particle-cell interaction in suspensions was observed where populations of individual cells and cell clusters are present. This can be seen in Figure 22, which illustrates the counting scheme used to characterize the populations; individual cells and clusters of cells were counted.

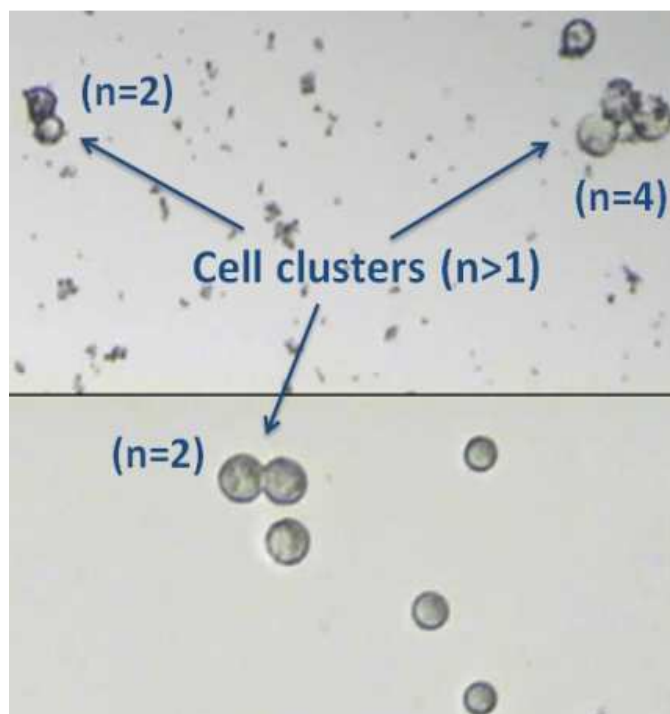


Figure 22 – Example of counting scheme. The total population is 8 including 5 individual cells and 3 clusters. Individual cells comprise $5/8=62.5\%$ of total population.

Population constituents were counted at various incubation times, and the fractions of individual cells in suspensions with various particle concentrations are presented in Figure 23 as a function of incubation time. The individual-cell fraction initially decreases rapidly, from about 95% to about 60% in 10 min. Later, it increases slightly, indicating that some, but not all, clusters dissociated back into individual cells. Thus, coverage values measured at later incubation times included cells that had previously clustered. It is plausible that following cluster dissociation, some broken-bond sites on separated cells can no longer support particle binding. This could explain why the surface coverage of individual cells does not increase with further incubation.

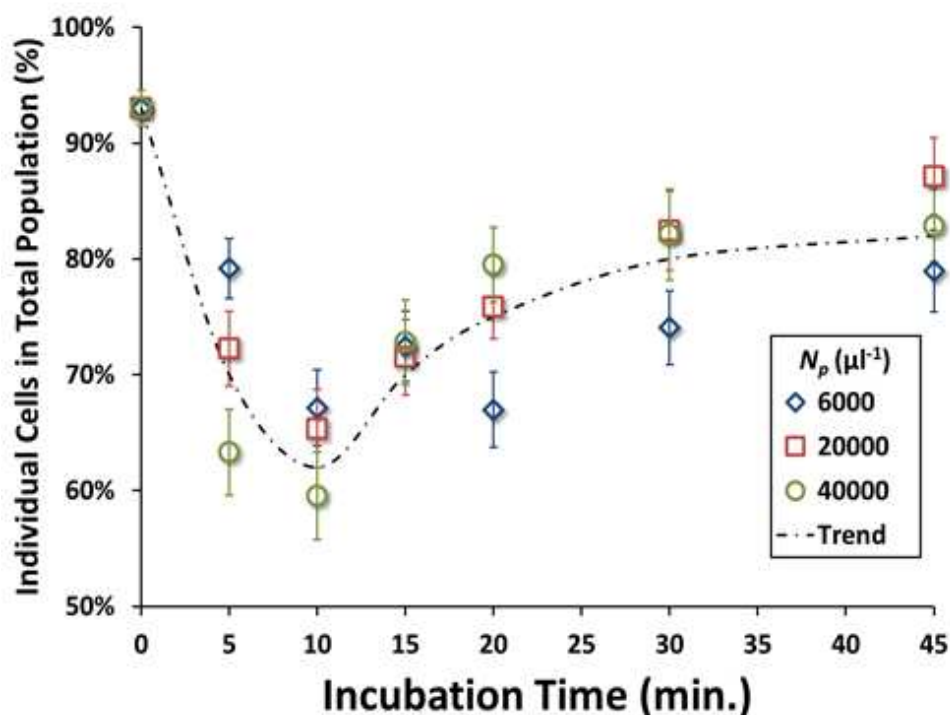


Figure 23 – Percentage of population appearing as individual cells for various times and particle concentrations; 100% means that all cells appear as individuals with no cell clustering.

4.3.5 Scaling Parameters for Cell Surface Coverage

As discussed in Sections 4.3.2 and 4.3.3, both flow induced particle-desorption and spontaneous loss of cellular binding affinity were found to be negligible. The findings discussed in Section 4.3.4, however, indicate that loss of binding affinity may occur as a result of cell-particle-cell interactions. This mechanism provides a means to construct a simple mathematical model to describe particle-cell interaction. Adsorption-only behavior is assumed and effects of binding affinity loss due to cell-particle-cell interaction are included. The fractional cell-surface coverage f is then given by

$$\frac{df}{dt} = K_{on}N_p(1 - f - f_{nv}) \quad (23)$$

where K_{on} is the particle adsorption rate and f_{nv} accounts for lost binding sites resulting from cell-particle-cell interaction. The time-evolution of f_{nv} is complex and its exact nature is unclear. The model is greatly simplified by approximating f_{nv} as directly proportional to f . For clarity, the proportionality constant, K_{on} and N_p are absorbed into a single constant $K_{nv}=K_{nv}(N_p)$.

$$\frac{df}{dt} = K_{on}N_p(1 - f) - K_{nv}f \quad (24)$$

Using this approximation, f may now be described as a first-order system such that:

$$\begin{aligned} f(t) &= \frac{N_p K_{on}}{N_p K_{on} + K_{nv}} \left[1 - e^{-(N_p K_{on} + K_{nv})t} \right] \\ &= f_{ss} \left[1 - e^{-t/\tau} \right] \end{aligned} \quad (25)$$

Fitting Equation 25 to each data set provides values for a time constant and steady-state coverage. Using the time constants and steady-state values as scaling parameters, the results presented in Figure 19 can be normalized as shown in Figure 24.

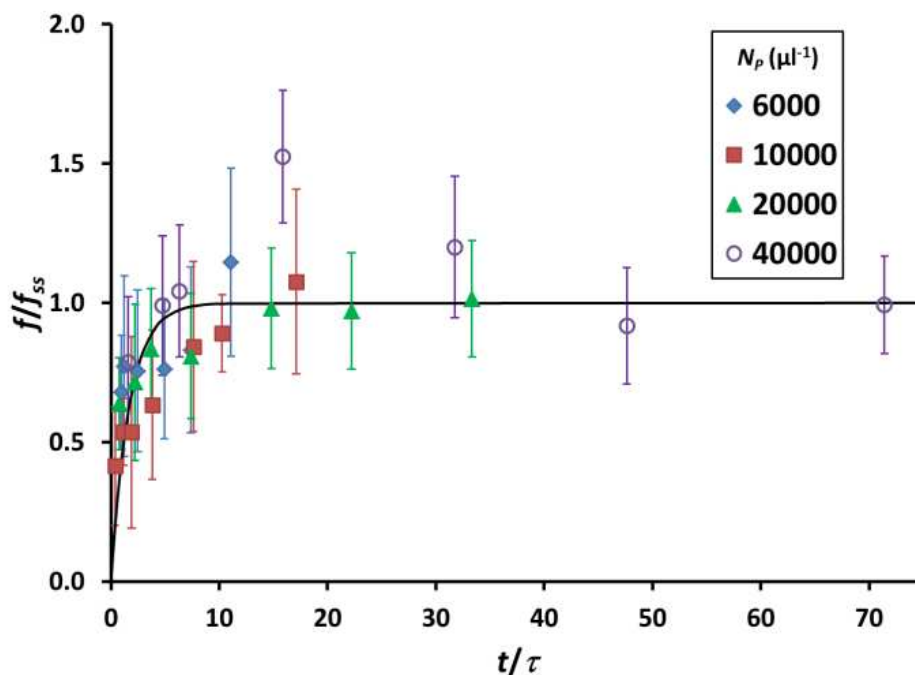


Figure 24 – Cell surface coverage normalized by its steady-state value, f/f_{ss} , as a function of the normalized incubation time, t/τ . Experimental results (symbols) collapse onto a single exponential curve (solid line calculated using Equation 25) for the low particle concentrations but not for the high particle concentration $N_p=40000 \mu\text{l}^{-1}$.

Once normalized, the data for all but the highest concentration ($N_p=40000 \mu\text{l}^{-1}$) collapse onto a single curve. The lack in agreement of Equation 25 with this particular set of data owes to the mechanism represented by the desorption-like term in our model; cell-particle-cell interaction effects differ on a fundamental level from true desorption effects. In contrast to desorption, cell-particle-cell cluster association-dissociation processes are not reversible since binding affinity is lost. Hence, they do not balance with adsorption, but instead tend to limit it thereby resulting in a final surface coverage value between 0 and 1; this is the steady-state value. Since cell-particle-cell clustering requires available binding sites, which are destroyed upon cluster dissociation, it is a self-limiting process. The cell-particle-cell interactions and particle-cell binding both cease when the available binding area reaches zero. The surface coverage value at this point in time

corresponds to the steady-state condition. Despite their differences, particle desorption and cell-particle-cell interaction often do not produce discernibly differing results; thus, the first-order approximation to the model description. Only with high particle concentration, for which there is rapid particle-cell binding and cell-particle-cell clustering very early on, do these differences become apparent. In such cases, both particle-cell binding as well as cell-particle-cell clustering processes occur faster than they are limited by binding affinity loss due to cluster dissociation. It therefore displays an overshoot in surface coverage, with a peak corresponding to the point at which the limiting effects “catch up” and begin to take over as the dominant mechanism driving the evolution of the average measured cell surface coverage in time; effects that are not described by the model.

Comparison of Figure 23 and Figure 24 reveals that the data fail to collapse onto the exponential curve only when cell-particle-cell clustering is at its highest. This suggests that particle-cell interaction may be represented reasonably well as a first-order system. The time constants and steady-state values are plotted as functions of particle concentration in Figure 25.

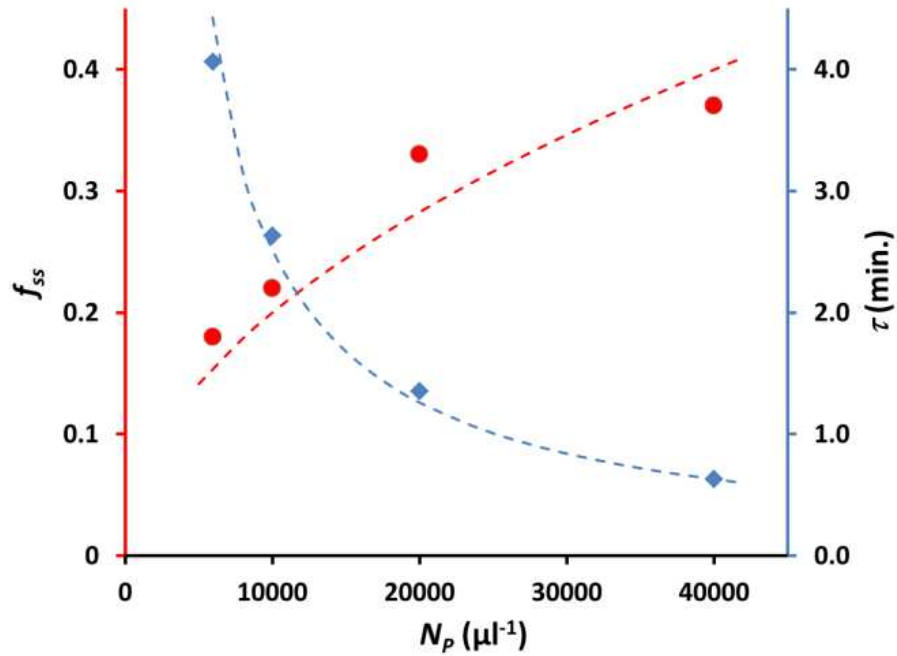


Figure 25 – A comparison between experimentally estimated steady-state and time-constant values (symbols) as a function of the particle concentration and calculated values (dash lines) based on a first-order interaction model (Equations 25-27).

Theoretical considerations suggest a functional dependence of the time-constant on particle concentration as given by Equation 26. Similarly, a dependence of the form given by Equation 27 is suggested for the steady-state value.

$$\tau(N_p) = C_1 N_p^{-1} \quad (26)$$

$$f_{ss}(N_p) = C_2 N_p^{1/2} \quad (27)$$

Fitting these functional forms to the experimentally estimated steady-state and time constant values, as plotted in Figure 25, shows a good agreement and yields coefficient values of $C_1=25000 \text{ min}/\mu\text{l}$ and $C_2=0.002 \mu\text{l}^{1/2}$.

The good agreement seen in Figure 25 validates the use of scaling parameters used to obtain Figure 24. Particle-cell binding is thus well-described by a first-order model with binding affinity loss due to cell-particle-cell interaction accounted for with a desorption-type term as long as the particle concentration is sufficiently low. To quantify what constitutes ‘sufficiently low’ particle concentration, it is necessary to characterize the effects of cell-particle-cell interaction in a way that will allow for comparison.

4.3.6 Cell-Particle-Cell Interaction Analysis

The data plotted in Figure 23 represent the relative constituency of two species, individual cells and clusters of cells and particles, of the total population. Hence, in a way similar to that followed in Section 2.1.1, the kinematics may be modeled by assuming each of the two species to be homogenous (i.e. clusters behave identically, regardless of size). The difference here is that in addition to cluster formation, clusters may also dissociate back into individual cells. The kinematic description of time-evolution of the number of individual cells N_c and number of cell clusters N_{cl} resulting from the cell-cluster association-dissociation process is as follows:

$$\frac{dN_{cl}}{dt} = K_{a1}N_c - K_{d1}N_{cl} \quad (28)$$

$$\frac{dN_c}{dt} = -K_{a1}N_c - K_{a2}N_cN_{cl} + K_{d2}N_{cl} \quad (29)$$

Here, K_a and K_d are the rates of cluster association and dissociation, respectively. K_{a1} and K_{a2} represent the rates of individual cells combining with other individuals and with cell clusters, respectively. Similarly, K_{d1} and K_{d2} represent the rates of full cluster dissociation, and dissociation of individual cells from clusters, also respectively. The system is thus described by two simultaneous, coupled first-order processes and therefore displays second-order behavior.

To linearize the system, the depletion of individual cells due to association may be approximated as proportional to the total number of bodies, N_c+N_{cl} . Collecting like terms and defining new rate constants to remove redundancy yields the following linear system:

$$\frac{dN_{cl}}{dt} = -K_{d1}N_{cl} + K_{a1}N_c \quad (30)$$

$$\frac{dN_c}{dt} = K_{d3}N_{cl} - K_{a3}N_c \quad (31)$$

Since Equations 30 and 31 are linearly independent, the solution is given by two decaying exponentials with rate constants corresponding to the eigenvalues of the coefficient matrix. The solution takes the following form for both N_c and N_{cl} :

$$N_{c/cl}(t) = Ae^{-t/\tau_a} + Be^{-t/\tau_d} \quad (32)$$

The coefficients A and B are determined by initial and steady-state values and τ_a and τ_d are the time-constants characterizing association and dissociation, respectively. Since the dissociation process is primarily the result of hydrodynamic loading, it is reasonable to assume that its characteristic timescale is not a function of particle concentration; $\tau_d \neq \tau_d(N_p)$. The cluster formation process, however, relies on particles for intercellular bridging and the characteristic timescale should therefore be a function of particle concentration; $\tau_a = \tau_a(N_p)$. The data presented in Figure 23 for $N_p=40000 \mu\text{l}^{-1}$ and $N_p=20000 \mu\text{l}^{-1}$ are plotted again in Figure 26 with corresponding best-fit curves according to Equation 32 with $\tau_d=6.9$ min in both cases.

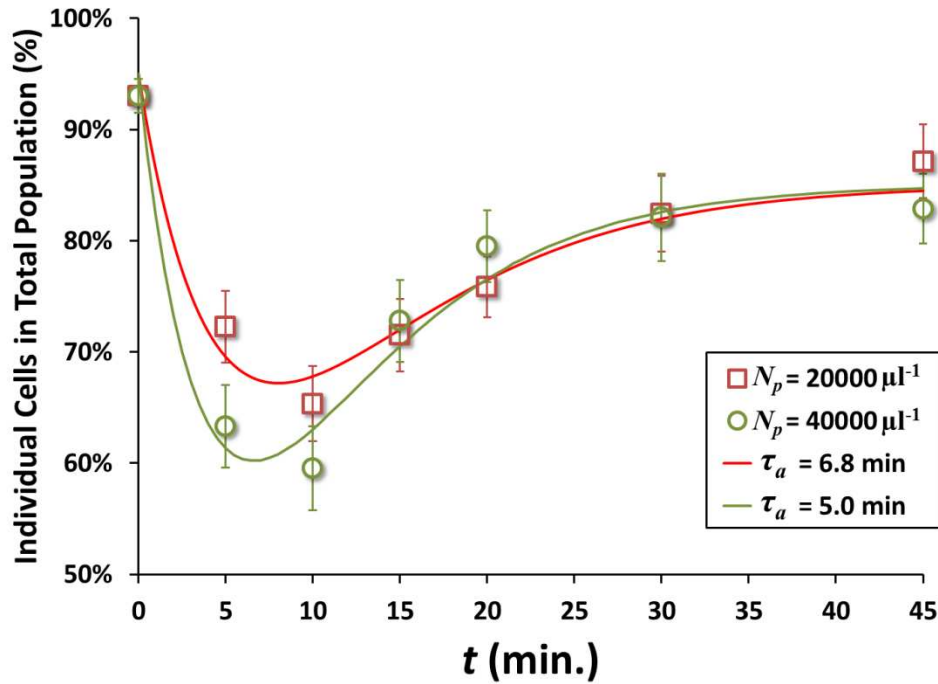


Figure 26 – Percentage of population appearing as individual cells re-plotted from Figure 23 and fit by Equation 32. Best-fit lines calculated using the same cluster-dissociation timescale $\tau_d=6.9$ min, but different cluster-association timescales $\tau_a=\tau_a(N_p)$. Comparison shows that cell-particle-cell clustering processes are association-dominated for only the highest particle concentration $N_p=40000 \mu\text{l}^{-1}$ for which $\tau_a/\tau_d\approx 0.7$.

For a particle concentration of $N_p=20000 \mu\text{l}^{-1}$, the best fit yields an association time-constant of $\tau_a=6.8$ min whereas in the case of $N_p=40000 \mu\text{l}^{-1}$, the association time-constant is $\tau_a=5.0$ min. In both cases, the dissociation time-constant is $\tau_d=6.9$ min; cluster association and dissociation processes occur at nearly identical rates for $N_p=20000 \mu\text{l}^{-1}$, and only for the highest particle concentration used, $N_p=40000 \mu\text{l}^{-1}$, does cluster association occur on a significantly shorter timescale than does cluster dissociation.

Comparison of the data for $N_p=6000 \mu\text{l}^{-1}$ in Figure 19 and Figure 23 shows that cell clustering initiates with relatively low surface coverage of $f\approx 0.15$. Furthermore, Figure 23 indicates that at this low surface coverage value, clustering continues and eventually yields

roughly the same minimum individual cell population (~65%) as do higher surface coverage values that result from higher particle concentrations (though on a larger timescale). These considerations suggest that the mere existence of the cell-particle-cell clustering phenomenon is relatively insensitive to surface coverage, and that increased surface coverage serves primarily to hasten the process. However, further consideration reveals that excessively-high surface coverage values must impede clustering; clearly, two already fully-occupied cell surfaces cannot be bridged by a monolayer of particles. Hindrance of the clustering phenomenon must occur when particles residing on the surface of one cell fail to locate available binding sites on another cell; when the product of particle-occupied area and available binding area $f \cdot f_{av}$ begins to decrease, so must the probability of two cells associating into a cluster upon encounter with one another. Although the precise relation of the available (viable) binding area f_{av} to the particle-occupied area f is unclear, an upper-bound on the surface coverage value at which the cell clustering begins to slow may be established by assuming no loss of binding affinity. The aforementioned product is then as follows:

$$f \cdot f_{av} \approx f \cdot (1 - f) \quad (33)$$

The maximum value of this product corresponds to $f=0.5$. Therefore, the surface coverage value at which additional particle-cell binding impedes cell-particle-cell clustering is *at most* $f=0.5$.

Since at any given time there is a distribution of surface coverage values amongst the cell population, often with considerable spread, cell clustering does not occur at a uniform rate for the entire cell population. Therefore, association-dominated clustering processes will preferentially remove, and deplete the individual cell population of cells within a certain surface coverage range (with an upper bound on the possible limit of $f=0.5$). If the process is *not*

association-dominated, although the preferential clustering will still be present, it will not deplete the population. It has been seen that for the particle concentration of $N_p=40000 \mu\text{l}^{-1}$, there exists a stage in the cell-clustering process that is association-dominated. Inspection of Figure 19 reveals that the peak value in surface coverage is $f \approx 0.6$, so it follows that this depletion has and/or continues to occur at and/or prior to the corresponding point in time $t=10$ min. Comparison with the dissociation timescale shows that at $t=10$ min, $t/\tau_d \approx 1.4$; the cluster-dissociation process is still underway and cells that were preferentially removed have not been reintroduced to the individual cell population (i.e. the measured sample). Thus, consistent with the findings of Section 4.3.2, the peak value does not indicate subsequent removal of bound particles, but is in fact the result of cells with surface-coverage values on the lower side of the distribution being temporarily removed from the population.

4.4 SPECIFIC INTERACTIONS BETWEEN ANTIBODY-FUNCTIONALIZED PARTICLES AND CIRCULATING TUMOR CELLS IN A MICROFLUIDIC DEVICE

The significant influence of cell-particle-cell interactions masks the effects of particle-single-cell interactions and convolutes interpretation of results. It was therefore sought to remove these interactions from the system. Additionally, better control of the flow field in which the cells reside was also required in order for the various effects to be attributed a specific parameter. These facts mandated a new approach that allowed full control of shear strain rate (local as opposed to average), and the ability to prevent intercellular interactions. Although it may be thought of as applicable to dosage, a full characterization of cell-particle-cell interactions is not the purpose of this work. The reason is two-fold; first, the scarcity of circulating tumor cells in humans, around 1-10 per ml of blood [65], means that the frequency of two CTS's colliding is

extremely low; second, a full understanding of these interactions first requires characterization of the interactions of particles with an individual cell. In pursuit of these goals, a microfluidic device was incorporated into design of experiments. Through the use of a microchannel, the desired control over the flow field was achieved and cell-particle-cell interactions were prevented.

The basic approach was to immobilize cells on a microchannel surface, then flow a particle suspension through the channel. This precluded the possibility of cell-particle-cell interaction and granted control over shear strain rate. Additionally, it offered a limited ability to observe what was happening in real time, although nothing quantitative could be determined from real-time observations due to the optical properties of the microchannel materials.

4.4.1 Validation of Specimen Preparation Methods

As outlined in Section 2.4, it was necessary to dismantle the microchannels prior to data acquisition. The method of specimen preparation following experiments was not previously tested and therefore verification of its efficacy was required. Verification was achieved by comparing images taken immediately following an experiment with images taken after the disassembly of the channel was complete. Such images are shown in Figure 27 where it is seen that the process involved in fixing the specimen and removing the PDMS from the glass has not disturbed particles bound to cells.

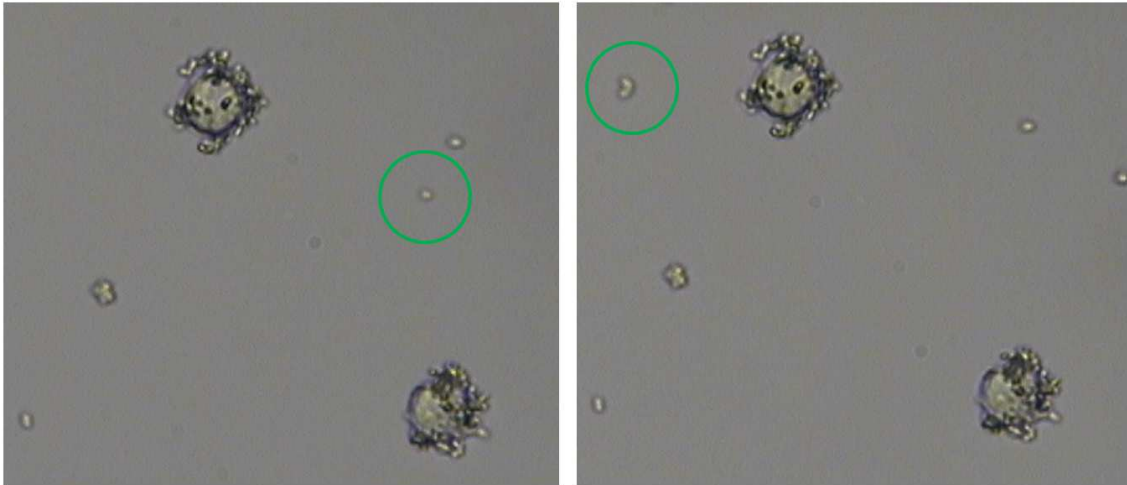


Figure 27 – Images taken (a) before and (b) after removal of the PDMS channel. Although some free particles are seen to have moved (green circles), particles bound to cells remain undisturbed.

4.4.2 Modeling Particle-Cell Binding For Immobilized Cells in a Steady Shear Flow

Referring back to the most general form of the model, Equation 6, the number of bound particles on a cell obeys the following kinematic relationship:

$$\frac{dv(t)}{dt} = k_{on}N_p[1 - f(t)] - k_{off}v(t) \quad (6)$$

Modeling the dynamics requires knowledge of the two unknown rate functions.

As a starting point, consider the experimental control parameters which are particle concentration N_p , flow volume V , and flow rate Q . It was shown in Section 4.1.1 that the rate of aggregation of particle onto existing clusters is directly proportional to particle concentration. A corollary of this finding is that particles do not interact with each other while in suspension (within the given concentration range). The particle suspensions utilized in particle-cell interaction experiments were much more dilute than the suspensions used in obtaining this result. It is therefore a reasonable assumption that interaction between functionalized particles in the experiments described herein is negligible. From this assumption, one may state

$$k_{on} \neq k_{on}(N_p)$$

$$k_{off} \neq k_{off}(N_p)$$

The next parameter to address is flow volume. Flow volume is an indirect measure of incubation time. Results presented in Section 4.3.3 indicated that spontaneous loss of cellular binding affinity was negligible. It is reasonable to assume this finding still valid for cells immobilized in microchannels, but it important to note that in this case the assumption remains untested. With this caveat in mind,

$$k_{on} \neq k_{on}(t)$$

$$k_{off} \neq k_{off}(t)$$

The last control parameter, flow rate, was chosen to study the effects of shear strain rate. It is known from the results discussed in Section 4.1.2 (as well as literature) that shear strain rate affects adsorption rates.

$$k_{on} = k_{on}(S)$$

While it is obvious that shear stress can remove particles and affect desorption, the magnitude of the stress required to do so is unknown. The analysis and discussion of Section 3.1.2 regarding ligand-receptor bond dynamics is worth revisiting here. Since the particle-cell bond is the result of many ligand-receptor bonds, one must consider the entire system of ligand-receptor complexes in order to gain knowledge of the particle desorption rate. Several points made in the discussion should be reiterated here. First, the rate of ligand-receptor bond formation from an encounter complex is constant, but the bond rupture rate is dependent on force. Second, the response time of the ligand-receptor bond formation-rupture system has a lower bound on the

order of milliseconds and increases with increasing applied force. Third, as a consequence of the first point, the steady-state fraction of ligand-receptor complexes that are in a bound state (as opposed to encounter complexes) depends on force in such a way that there is a critical particle-cell force value. If this critical value is exceeded, no steady state can exist; as ligand-receptor bonds break, the burden is passed to other bond complexes. Since the load on individual ligand-receptor bonds continues to increase, the bonds continue to rupture and the rate at which this occurs continues to increase.

Analysis is significantly simplified by comparing the response time of the ligand-receptor complex system to an appropriate scale characterizing impulse in the particle-cell bond system within a microchannel. Since the flow is steady, there is no such time scale; once a flow rate is chosen, it is set and the flow continues at that rate until the end of the experiment. Therefore, the ligand-receptor complex system that exists between a cell and bound particle may be considered always to be at steady state. Hence, the force on a particle-cell bond in comparison to the critical force is what will determine if desorption occurs. This means that the desorption rate is effectively a step function; particles will either stay bound to a cell, or if the critical shear strain rate is exceeded, the majority of the particles will rapidly desorb. Due to the stress distribution over the surface of the cell, there will be some range of shear strain rate that only causes desorption on certain parts of the cell, but this would be a readily observed effect since the distribution would cause relatively small deviation from the peak value for most of cell surface. Also conceivable is the cell detaching from the channel, in which case it is removed from the sample and this effect does not present itself in the data. With consideration paid to these arguments, it shall be assumed that particle desorption is not a factor. Existence of a steady-state

other than unity most likely indicates desorption effects; if present, these effects will present themselves in the experimental data and the issue may be revisited.

$$k_{off} \neq k_{off}(t)$$

Now, the dynamics of particle-cell interaction are introduced through the adsorption rate function.

$$\frac{dv(t)}{dt} = k_{on}(S)N_p[1 - f(t)] \quad (34)$$

At this point the $k_{on}(S)$ is still unknown, but as was discussed in depth in previous sections, the orthokinetic kernel is given by $k_o = S\lambda^3$ where λ is a length scale characterizing the capture volume and is itself dependent on shear strain rate $\lambda = \lambda(S)$. This length scale is known to frequently obey a power-law relationship with shear strain rate, as was also discussed previously. Therefore, it is reasonable to assume the adsorption rate function also obeys a power-law relationship with shear strain rate.

$$k_{on}(S) \propto S^a$$

For consistency in the units, this is best incorporated into Equation 34 as follows:

$$\frac{dv(t)}{dt} = v_{max}K_{on} \left(\frac{S}{S_0}\right)^a N_p[1 - f(t)] \quad (35)$$

$$\frac{df(t)}{dt} = K_{on} \left(\frac{S}{S_0}\right)^a N_p[1 - f(t)] \quad (36)$$

Equations 35 and 36 describe the evolution of the number of particle bound to a cell, and fractional cell-surface coverage, respectively, in time. The constants K_{on} and a are unknown and must be determined empirically. The value of v_{max} may be estimated from the size of a typical cell, the particle size, the fraction of the cell that is in contact with the channel surface

(immobilizing the cell), and the 2D random close packing factor $\phi_{RCP}=0.84$. With these, a value in the range of $v_{max}\sim 150$ is estimated.

Solution of Equation 36 gives the following:

$$f(t) = 1 - \exp \left[-K_{on} N_p \left(\frac{s}{s_0} \right)^a t \right] \quad (37)$$

Equivalently,

$$f(t) = 1 - \exp \left[-t/\tau \right] \quad (38)$$

$$\tau \equiv \left[K_{on} N_p \left(\frac{s}{s_0} \right)^a \right]^{-1}$$

4.4.3 Asymptotic Analysis and the Linear Approximation

As will be abundantly clear, attempting to compare the theoretical model with the data presented in the first part of Section 4.4.4 (to follow) is futile; no statistically significant fit of the model can be made to these data. Instead, qualitative features may offer some information. There is no clear evidence of asymptotic behavior and to the contrary, linearity is suggested (albeit weakly). If there is indeed linear behavior, it cannot be valid everywhere since there is a finite limit to the number of bound particles on a cell. Therefore, if the theoretical model is accurate, the data presented must describe the particle-cell binding process in its early stage; a stage for which the exponential is nearly linear. During such a stage, the deviation of the exponential from linear is, for the most part, much less than experimental error. Consequently, any exponential behavior in the data would be masked by experimental error. Without assuming any knowledge of the time constant, it may be confirmed that the condition is met by noting that the fractional

surface coverage does not exceed 0.63, the value at which $t=\tau$. Satisfying the condition shows that small t/τ approximations to the model are appropriate. As such, a Taylor series expansion of the exponential in $(-t/\tau)$ approximates the model for small t as follows:

$$\exp\left[-\left(\frac{t}{\tau}\right)\right] \approx 1 - \left(\frac{t}{\tau}\right) + \frac{1}{2}\left(\frac{t}{\tau}\right)^2 + \dots \quad (39)$$

Dropping higher order terms and incorporating the expansion into

$$f(t) \approx f_{ss} \cdot \left(\frac{t}{\tau}\right)$$

$$f(t) \approx K_{on} N_p \left(\frac{S}{S_0}\right)^a t \quad (40)$$

In this approximation, the model is readily able to be fit to the data, but the mere possibility of a fit does not mean the model description is accurate. Therefore, discussion of the theoretical model shall be set aside until further analysis of the experimental data can yield an interpretation without speculation.

4.4.4 Effects of Particle Concentration and Incubation Time

Since particle concentration was not only difficult to prescribe accurately, but also did not remain constant for long periods of time, it was not feasible to simply fix its value and vary the other parameters. From a large number of experiments, several sets were identified that utilized similar particle concentration values but differing values of flow rate or volume. These sets of experiments comprise only a fraction of the total number of experiments performed. Consequently, only a small fraction of the available data may be meaningfully presented in graphical form when N_p is the fixed parameter. This demands a different approach to

determining the effects of particle concentration; the approach detailed herein requires a simultaneous examination of both particle concentration effects and flow volume effects.

The average number of particles bound to a cell is plotted as a function of flow volume for several values of particle concentration with flow rate fixed at $Q=1.0 \mu\text{l/s}$ in Figure 28. Without yet staking any claims in the way of validity or accuracy, assume the behavior to be linear (at least for the time being). As discussed in the previous section, the behavior cannot be linear everywhere, and no claim of this is being made. A linear regression has been applied to each data set as shown by the dashed lines. In some cases, a straight line fits the data quite well, but in others the fit is questionable at best. Nevertheless, applying a fit provides a tool for analysis from which the applicability of a linear fit may be further examined.

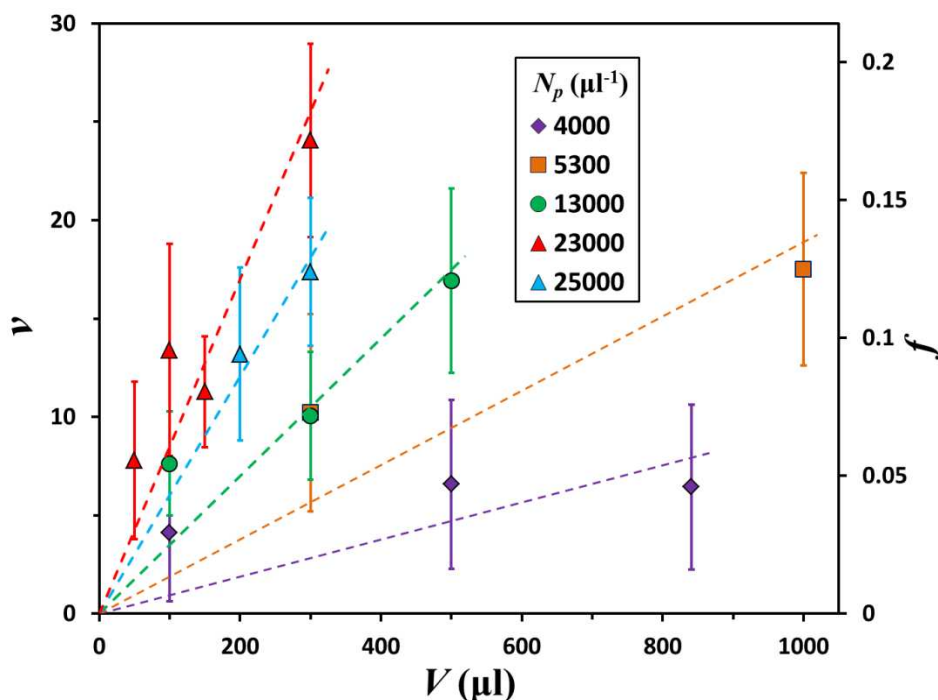


Figure 28 – Average number of bound particles per cell ν (left axis) and fractional cell-surface coverage f (right axis) as functions of flow volume for various particle concentrations with flow rate fixed at the reference value $Q=1.0 \mu\text{l/s}$. Dashed lines are linear fits made for the purposes of analysis and discussion and are not intended to indicate linear behavior.

With the exception of the fit to the data for $N_p=23000$, the slopes exhibit a trend of increasing with particle concentration. The discrepancy observed amongst the highest concentrations is likely attributable to measurement error in the particle concentration; the values shown are only nominal. With the best-case accuracy of $\pm 10\%$, $N_p=23000$ and $N_p=25000$ are well within error of one another. One obvious approach to prevent this source of error from showing itself in such a way would be to average the data when particle concentration values are within error of each other. Although this would prevent the appearance of possibly misleading trends (or lack of a trend altogether), it would introduce its own error and as will be shown, is not necessary due to the averaging that is inherent to the data reduction. For these reasons, the data are shown as-is and some discrepancy is to be expected.

The average number of particles bound to a cell is plotted as a function of particle concentration for various flow volumes with flow rate fixed at $Q=1.0 \mu\text{l/s}$ in Figure 29. Figure 29 also shows some fairly reasonable linear fits with slopes following a trend of increasing with flow volume. Consistency requires that the trends in the data seen in Figure 29 should show in Figure 28, and vice versa. This is indeed the case to within experimental error.

Some of the data shown appear in both Figure 28 and Figure 29, but these figures are not merely the same data plotted in two different ways; the majority of what is shown in each figure is unique to that figure. Much of the analysis that is to come relies on this fact.

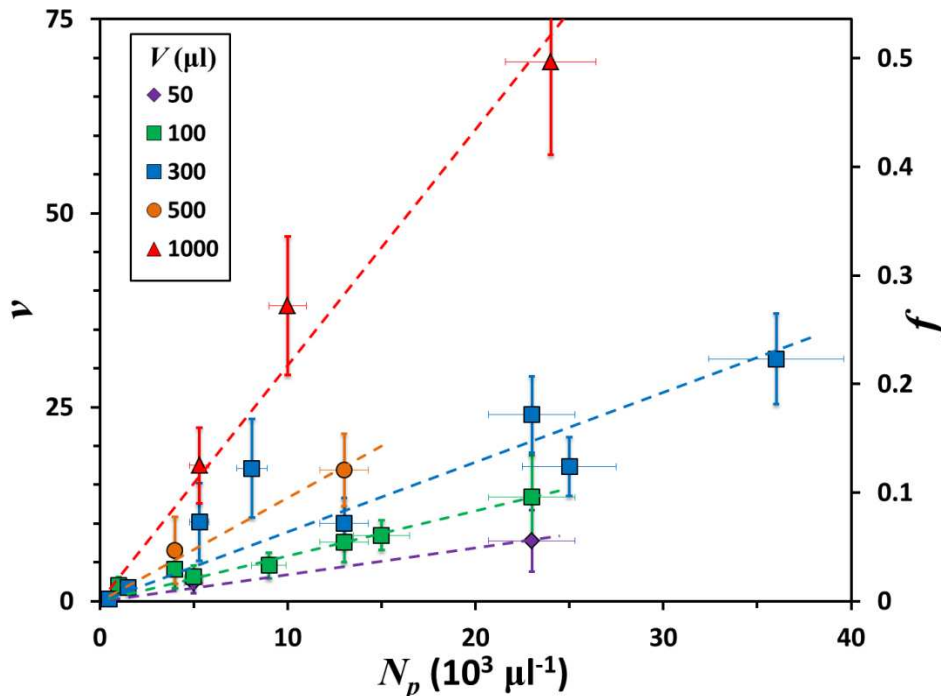


Figure 29 – Average number of bound particles per cell ν (left axis) and fractional cell-surface coverage f (right axis) as functions of particle concentration for various flow volumes with flow rate fixed at the reference value $Q=1.0 \mu\text{l/s}$. Dashed lines are linear fits made for the purposes of analysis and discussion and are not intended to indicate linear behavior.

Figure 28 and Figure 29 offer little more than identification of general trends. Further analysis is required in order to obtain functional relationships from the experimental data. In kind, the slopes of the linear regressions applied to the data shown in Figure 28 and Figure 29 are plotted in Figure 30 and Figure 31, respectively, as functions of their fixed parameters.

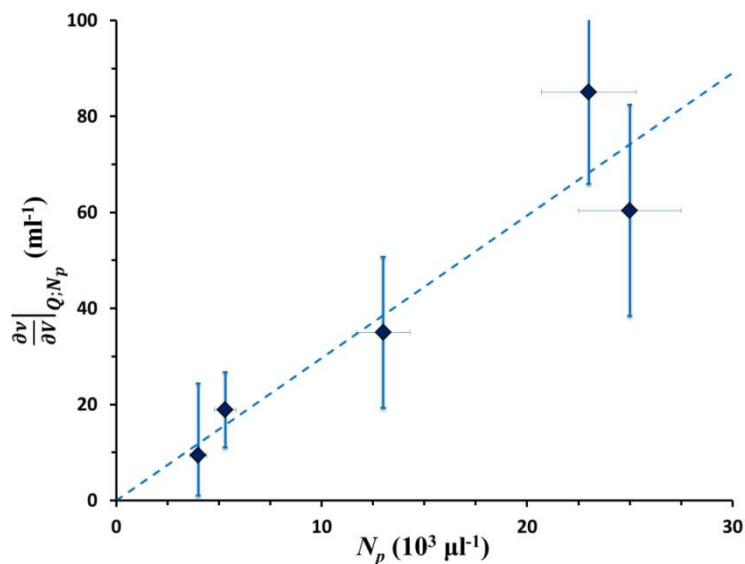


Figure 30 – Slopes of linear fits to the data shown in Figure 28 as a function of particle concentration.

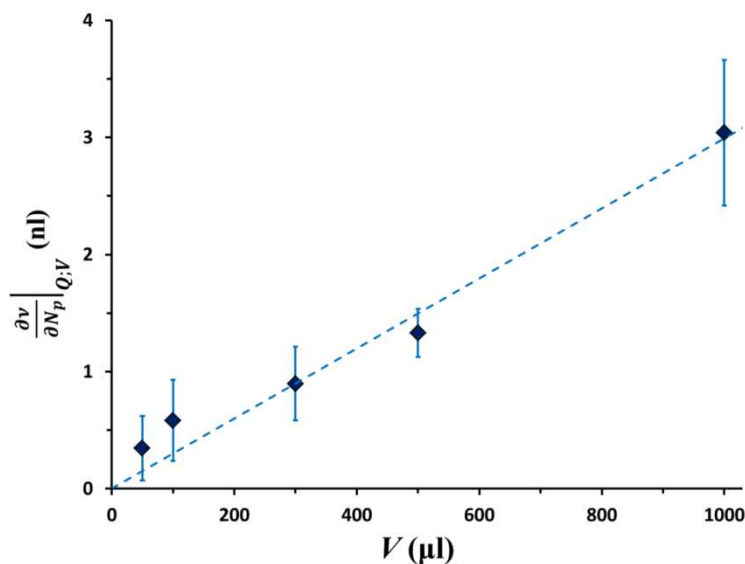


Figure 31 – Slopes of linear fits to the data shown in Figure 29 plotted as a function of flow volume.

There are several important deductions to be made from the figures above. The trends in the slopes of the fits in Figure 28 and Figure 29, briefly discussed earlier, are visually apparent in Figure 30 and Figure 31, as is the earlier-mentioned discrepancy and the error to which it was attributed. The significance of Figure 30 and Figure 31 is in revealing that, when examined

quantitatively, what were previously observed only as trends actually suggest correlation. In doing so, Figure 30 and Figure 31 have shown strong evidence of the validity of the assumptions upon which they are based in the first place (i.e. linearity). In Figure 30, the slopes of the best-fits describing $v(V;N_p)$ are plotted as a function of N_p and a straight line fits reasonably well (substantially better than many shown in Figure 28 and Figure 29). This linear fit implies

$$\left. \frac{\partial v}{\partial V} \right|_{Q;N_p} \propto N_p \quad (41)$$

Analogously, Figure 31 shows the slopes of best-fits describing $v(N_p;V)$ as a function of V . Again, a straight line fits nicely with the implication here being

$$\left. \frac{\partial v}{\partial N_p} \right|_{Q;V} \propto V \quad (42)$$

Integrating Equations 41 and 42 gives

$$v(N_p, V, Q = Q_{ref}) \propto N_p V + y(N_p) \quad (43)$$

$$v(N_p, V, Q = Q_{ref}) \propto V N_p + y(V) \quad (44)$$

where $y(N_p)$ and $y(V)$ are unknown functions resulting from integration. With no need for knowledge of the unknown functions, Equation 43 (which resulted from assuming linearity in N_p) states that f is linear in V . Conversely, Equation 44 (which resulted from assuming linearity in V) states that f is linear in N_p . Thus, the goodness-of-fit of the linear regressions presented in Figure 30 and Figure 31 each strengthen the assumption of the linearity used in constructing the other. This linearity and the validity thereof will be revisited.

By applying the linear regression represented by the dashed line in Figure 30, one obtains a continuous-function representation of $v=v(N_p,V)$. The slope obtained from this regression is represented as follows:

$$\frac{\partial}{\partial N_p} \left(\frac{\partial v}{\partial V} \Big|_{Q;N_p} \right) = \frac{\partial^2 v}{\partial N_p \partial V} \Big|_Q \quad (45)$$

The value (with extra figures that are outside significance kept for later use) is

$$\frac{\partial^2 v}{\partial N_p \partial V} \Big|_Q = (2.97 \pm 0.58) \times 10^{-6} \quad (46)$$

Similarly, applying the fit shown in Figure 31 also provides continuous-function representation with the slope and its value (again with extra figures) as follows:

$$\frac{\partial}{\partial V} \left(\frac{\partial v}{\partial N_p} \Big|_{Q;V} \right) = \frac{\partial^2 v}{\partial V \partial N_p} \Big|_Q \quad (47)$$

$$\frac{\partial^2 v}{\partial V \partial N_p} \Big|_Q = (2.99 \pm 0.27) \times 10^{-6} \quad (48)$$

N_p and V are independent of one another so the order of differentiation is irrelevant. Interchanging N_p and V in the differential operators in Equation 47 yields exactly Equation 45. Therefore, the slopes obtained from the best-fit lines in Figure 30 Figure 31 should be equal; this is confirmed on comparison of the two slope values. What is shown above is a consequence of what is arguably the most important finding to come from Figure 30 and Figure 31 and is as follows:

$$\frac{\partial^2 v}{\partial V \partial N_p} \Big|_Q = C_1 = \text{constant} \quad (49)$$

For this to be true requires linearity in both N_p and V . Upon integration, it admits the following:

$$v(N_p, V; Q = Q_{ref}) = C_1 N_p V + g_1(N_p) + g_2(V) \quad (50)$$

The two unknown functions g_1 and g_2 must be zero which can be shown by setting either N_p or V to 0.

$$v(N_p V; Q = Q_{ref}) = C_1 N_p V \quad (51)$$

Dividing by v_{max} expresses this in terms of fractional cell-surface coverage.

$$f(N_p V; Q = Q_{ref}) = \frac{C_1}{v_{max}} N_p V \quad (52)$$

This simple yet important result shows that within the parameter range at hand, f is a function only of the product $N_p V$, and not N_p nor V alone. This comes directly from reduction of the experimental data with no more than an assumption of linearity; an assumption that shall now be tested conclusively.

Equation 51 allows all of the data depicted in Figure 28 and Figure 29 to be plotted on a common axis $N_p V$, and provides the strongest test yet of linearity in both N_p and V . The average number of particles bound to a cell is plotted as a function of the product $N_p V$ in Figure 32 where the data fall along a single straight line.

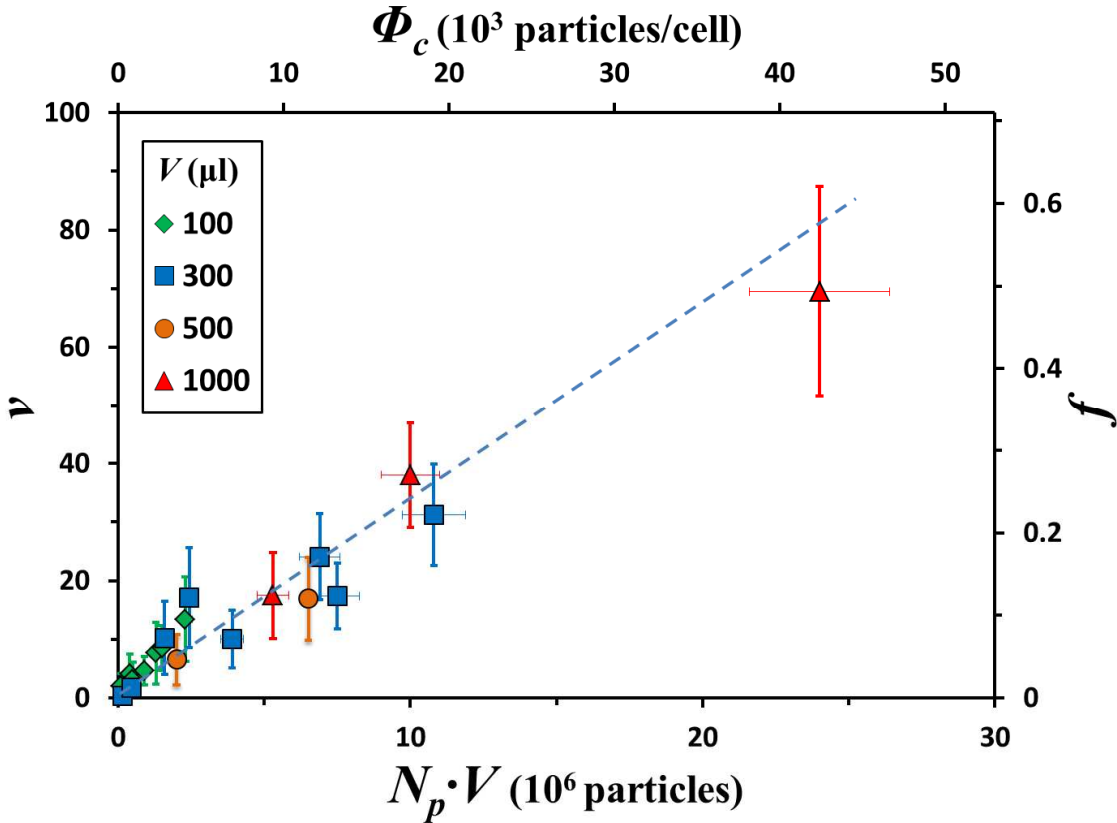


Figure 32 – Average number of bound particles per cell ν (left axis) and fractional cell-surface coverage f (right axis) functions of $N_p \cdot V$ with flow rate fixed at the reference value $Q=1.0 \mu\text{l/s}$. For comparison, the flow volumes are indicated by the different markers; particle concentration may be deduced from the x-coordinate. The data shown here include all of the data shown in Figure 28 and Figure 29; each point corresponds to a different value of the pair (N_p, V) . The quality of fit achieved by a straight line indicates linearity of f and ν in both N_p and V .

Each point appearing in Figure 32 corresponds to one or more experiments characterized by a pair of N_p and V values that is not shared with any other point. This confirms the assumption of (approximate) linearity in both N_p and V under the given conditions. Since the validity of the sole assumption involved in the analysis of experimental results thus far has been confirmed, Equation 51 is a basis for comparison of experimental results and the mathematical model, and Figure 32 presents the data in the form most appropriate for comparison. Since it depicts all of the experimental data presented to this point in the section (and then some), applying a linear

regression to the data shown Figure 32 will yield the most statistically significant value of the slope already encountered twice before.

$$C_1 = \left. \frac{\partial^2 v}{\partial v \partial N_p} \right|_Q = (3.03 \pm .17) \times 10^{-6} \quad (53)$$

Once again, extra figures have been retained for comparison from which it is seen that this latest value is greater than both previous values. This potentially deceiving result is a consequence of the way in which previous values were obtained; Equations 46 and 48 correspond to slopes of best-fit lines shown Figure 30 and Figure 31, respectively. The data shown in these figures (to which the lines were fit) are themselves the result of best-fits. The purpose of Figure 30 and Figure 31 was to obtain and confirm the validity of the scaling applied to the data as depicted in Figure 32. It is the purpose Figure 32 to provide the most accurate means of obtaining an empirical value for the model parameter.

Before dealing with the theoretical model, several features of Figure 32 warrant further discussion. In physical terms, the quantity $N_p V$ is the total particle flux through the channel. By taking the ratio of the cross-sectional area of a typical cell to that of the channel (normal to streamwise), one may obtain an estimate of the particle flux Φ_c through the capture zone of a cell. The estimate may be improved by accounting for the velocity profile, which when integrated over the height of a typical cell, shows that the average velocity in this vicinity is roughly half that averaged over the entire channel. Utilizing the ordinate v with the abscissa Φ_c , which may be considered to be in ‘units’ of ‘captured particles per cell’ and ‘particles encountered per cell’ respectively, then the slope of the linear fit is a measure of capture efficiency. In this case, the capture efficiency is found to be roughly 0.1%. The interpretation here is that a typical cell has a ~0.1% chance of capturing each particle it encounters.

Determining a single value of capture efficiency that is independent of flow volume and particle concentration is only possible when (approximate) linearity holds.

In all likelihood, this value of 0.1% capture efficiency that has been estimated here will not see use outside this work; this was not the point of the above exercise. The point was to show that a single value that is applicable over a broad range of conditions can be established for a parameter that would be of crucial importance for many clinical applications. The results suggest that in principle, by measuring the average number of bound particles per cell for several values of $N_p V$, one may establish a calibration curve from which one may predict how many particles will bind to target cells for any particle concentration and incubation time (provided $t < \tau$).

Recalling Equation 40, in the small t/τ approximation the model is as follows:

$$f(t) \approx K_{on} N_p \left(\frac{S}{S_0} \right)^a t$$

Since S is directly proportional to Q , and V and t are related through Q as $Q = V \cdot t$, this is easily expressed in terms of the experimental parameters (note also that Q has remained constant to this point).

$$f(Q, N_p, V) \approx K_{on} \left(\frac{Q}{Q_0} \right)^{a-1} N_p V \quad (54)$$

Here, Q_0 is an arbitrary flow-rate scale that appears as a result of the dimensional analysis leading to the power-law relationship. Its purpose is to maintain consistency in units and fitting does not allow this (arbitrary) value to be determined separately from that of K_{on} . This does not present a problem because the units are fixed when curve fits are applied and with an appropriate choice of Q_0 the physical meaning of K_{on} is left intact. Specifically, the appropriate value is $Q_0 = 1$ [units of Q].

Equating the RHS of Equations 51 and 54 provides direct comparison of experimental results to the theoretical model.

$$\frac{c_1}{v_{max}} N_p V = K_{on} \left(\frac{Q}{Q_0} \right)^{a-1} N_p V \quad (55)$$

Since Q has remained fixed at $Q=1.0 \mu\text{l/s}$,

$$K_{on} = \frac{c_1}{v_{max}} \quad (56)$$

Insofar as functional dependence on N_p and V is concerned, the two are in good agreement, but the effects of shear strain rate must be taken into account for the complete picture to be revealed.

4.4.5 Effects of Shear Strain Rate

Shear strain rate effects were investigated in a similar manner as were flow volume effects; the flow volume was fixed at $V=100 \mu\text{l}$ while the flow rate was varied. As before, particle concentration was difficult to control, resulting in limited data for a given fixed particle concentration value. Nevertheless, from the numerous experiments, it was possible to identify sets of data for which the concentration was constant (within error) and the flow rate was varied. These data, in terms of the average number of bound particles per cell as well as the fractional cell-surface coverage, are plotted as functions of flow rate in Figure 33 for several values of particle concentration. As shown, the fractional cell-surface coverage remains well below 0.63 in all cases, so the small t/τ approximation is still valid. While there is not much else that can be stated conclusively from Figure 33 on its own, there is an apparent trend of increasing particle-cell binding with decreasing flow rate. This is consistent with related findings discussed previously in Section 4.1.2.

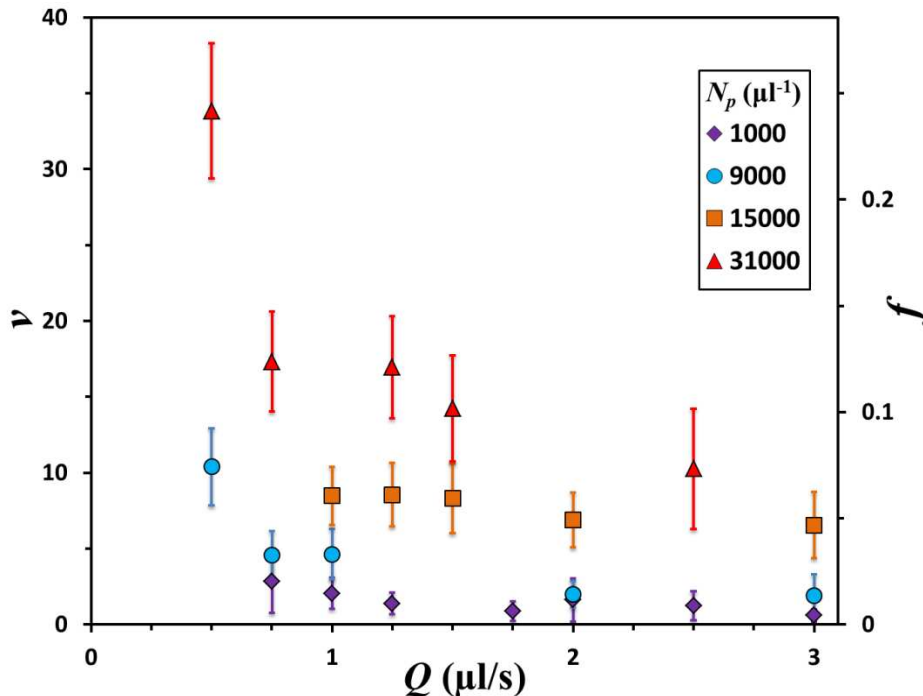


Figure 33 – Average number of bound particles per cell ν (left axis) and fractional cell-surface coverage f (right axis) as functions of flow rate for various particle concentrations with flow volume fixed at the reference value $V=100 \mu\text{l}$.

Just as before, more information may be obtained by examining the particle-cell binding dependence on particle concentration for various flow rates. Unlike before, however, it is already known that f is linear in N_p allowing for linear fits to be made without the need for assumptions (although it will later be seen that any such assumptions would again prove to be valid). The number of bound particles per cell and corresponding fractional cell-surface coverage are plotted as functions of particle concentration in Figure 34. The general trend of the best-fit slopes increasing with decreasing flow rate is consistent with the observations that were made pertaining to Figure 33.

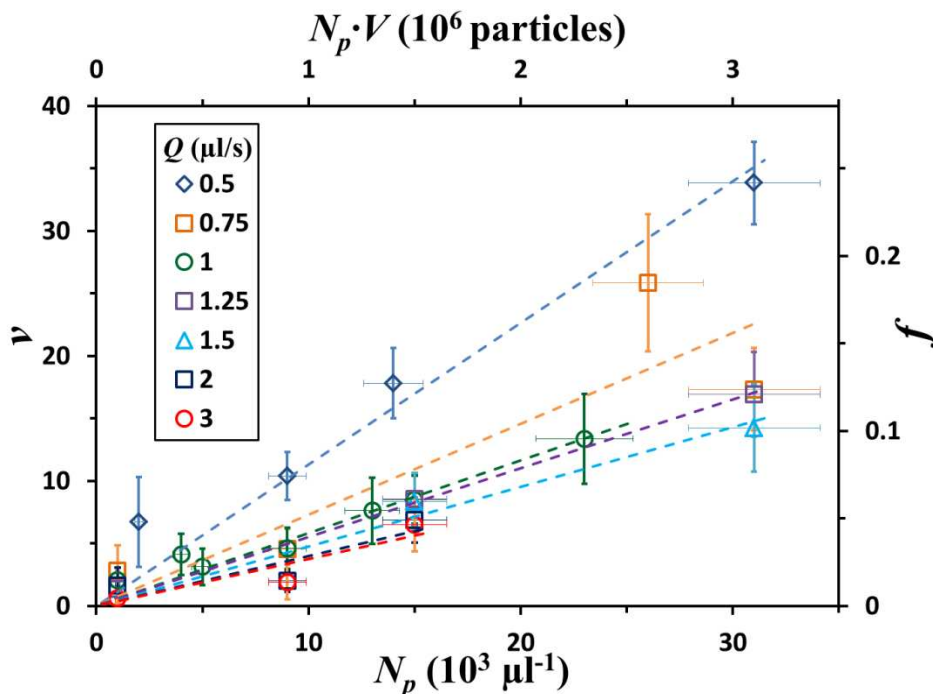


Figure 34 – Average number of bound particles per cell ν (left axis) and fractional cell-surface coverage f (right axis) as functions of particle concentration for various flow rates with flow volume fixed at the reference value $V=100 \mu\text{l}$.

Here, with flow volume fixed, the slopes are represented as follows:

$$\left. \frac{\partial \nu}{\partial N_p} \right|_{V;Q}$$

In contrast to findings discussed previously, the slopes do not exhibit a linear dependence on flow rate as is clear in Figure 35(a). Previous results and the findings of others (as discussed in Section 4.1) suggest a power-law relationship. Accordingly, the same data are plotted logarithmically in Figure 35(b) where it is seen that a power law fits the data quite well.

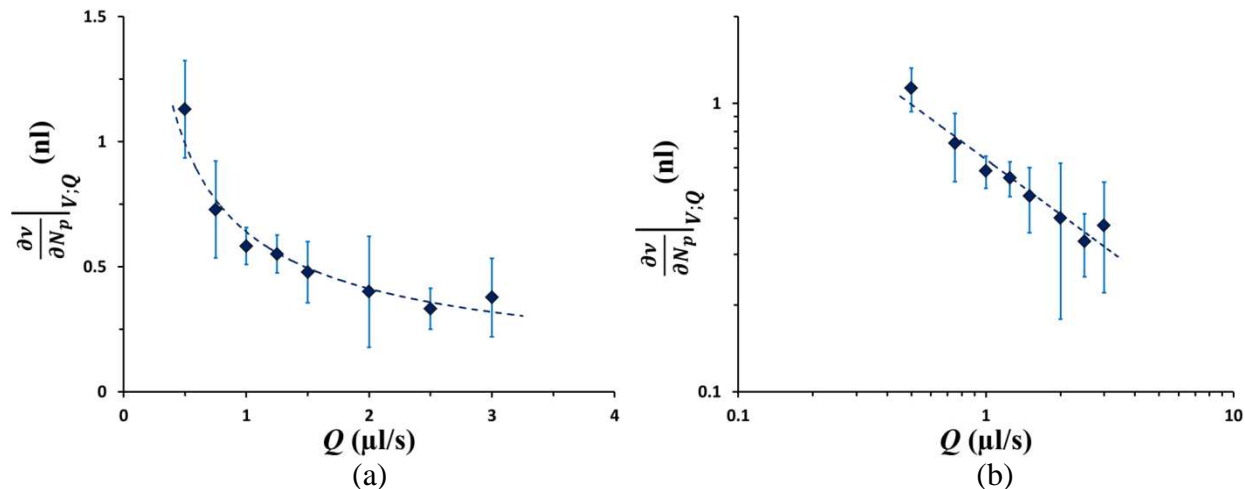


Figure 35 – Slopes of linear fits in Figure 34 as a function of flow rate plotted on (a) a normal scale, showing the strong affect shear strain rate can have on particle-cell binding at low flow rates and (b) a log-log scale, illustrating the high quality of fit achieved using a power-law relationship.

The power-law relationship observed in Figure 35 may be represented as follows:

$$\left. \frac{\partial v}{\partial N_p} \right|_{V;Q} = c_2 \left(\frac{Q}{Q_0} \right)^b$$

The fit provides two values; one coefficient and one exponent. However, only the exponent is of interest here, since a power-law fit introduces relatively large uncertainty into the coefficient.

Furthermore, as will be seen later, the coefficient is not needed.

$$(c_2 Q_0^{-b}) = 6.4 \times 10^{-4} \mu\text{l}$$

$$b = -.63 \pm .06$$

$$v(N_p, Q, V = V_{ref}) = c_2 \left(\frac{Q}{Q_0} \right)^{-.63} N_p$$

Plotting all the data shown in Figure 33 and Figure 34 together as a function of the product on the right-hand-side provides visual evidence of how accurately this describes the data for fixed $V=100 \mu\text{l}$.

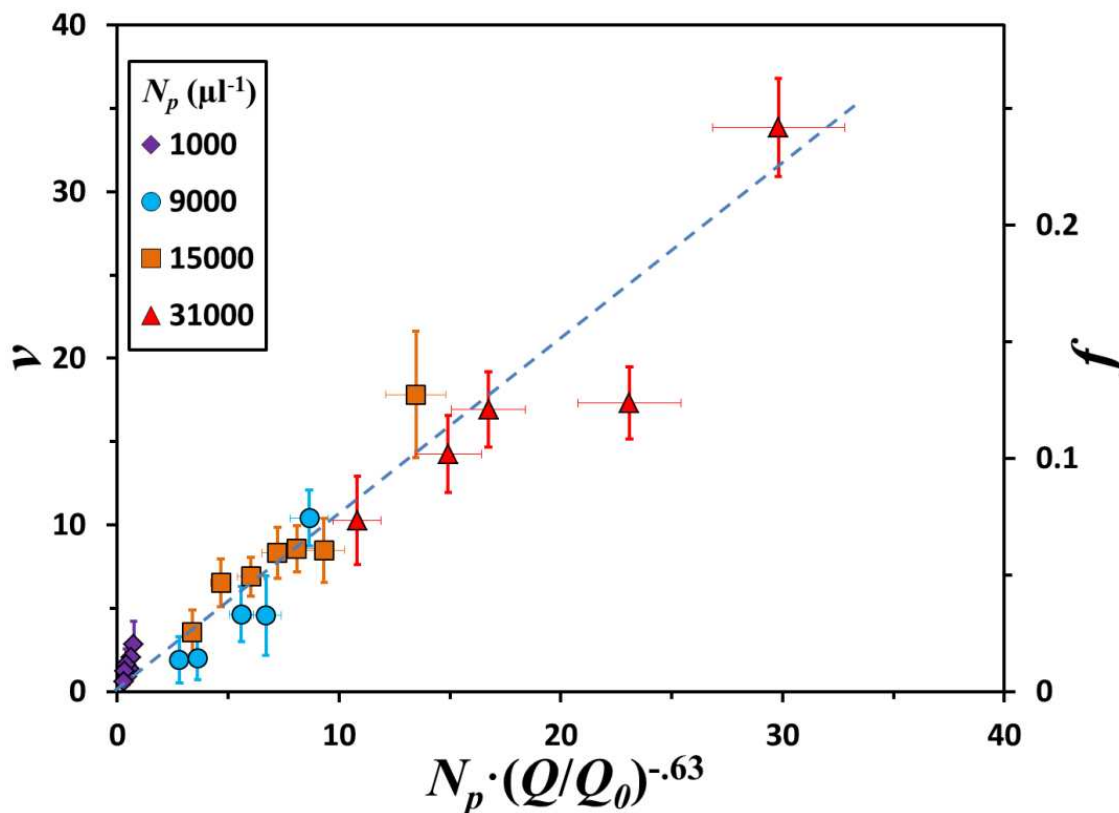


Figure 36 – Average number of bound particles per cell ν (left axis) and fractional cell-surface coverage f (right axis) as functions of the product $N_p(Q/Q_0)^{-0.63}$ for several values of particle concentration with flow volume fixed at the reference value $V=100 \mu\text{l}$. Analysis shows that this scaling of the x-coordinate should yield a linear relationship with ν and f ; the dashed line is for comparison purposes only.

4.4.6 Restrictions on Experimental Control Parameters

As was briefly mentioned in Section 2.4, several factors limited the values of the control parameters that were used. Various problems arose when excessively large or small values of flow rate, flow volume, or particle concentration were used, and careful determination of the

appropriate range of values for each of these parameters was necessary. Particle clustering, particle sedimentation, and cell viability/binding affinity loss were the primary concerns dictating the practical ranges.

At high particle concentrations, significant clustering occurred in the suspension regardless of its initial state in the syringe. To avoid cluster-cell interactions while also obtaining statistically significant results, the particle concentration was restricted to $10^3 < N_p < 3 \times 10^4 \mu\text{l}^{-1}$.

Particle sedimentation and cell-channel adhesion strength dictated the lower and upper bounds that were feasible for the flow rate. At excessively-low flow rates, particle sedimentation occurred in the tubing leading to non-uniform and/or depleted concentration within the channel, as well as particle clustering as the suspension entered the bend at the inlet to the channel. At excessively-high flow rates, cells began to detach from the channel. Since adhesion was the result of ligand-receptor affinity, it is reasonable to assume that cells expressing lower levels of EpCAM detached first, leaving only cells with relatively-high EpCAM expression levels. To avoid altering the averages, flow rate values were capped at a value at which no significant detachment was observed. The resulting range was $0.5 < Q < 3.0 \mu\text{l/s}$. However, at flow rates $Q < 1.0 \mu\text{l/s}$, it was found that sedimentation was still a factor and although it was not observed initially, extended flow periods provided ample evidence of the effects. Utilization of these low flow rates was required to satisfactorily characterize the effect of shear strain rate (see Figure 35a, for example), so the flow time was further constrained when low flow rates were used.

The time that cells remained attached inside the microchannel required control to avoid loss of cellular binding affinity. After ~40 min, the cellular binding affinity had decreased by an

amount such that the effect was abundantly clear upon first inspection. To mitigate error caused by this phenomenon, the flow time was restricted to 1000 s.

Based on the above-mentioned concerns, the following restrictions were imposed on the experimental control parameters:

$$10^3 < N_p < 3 \times 10^4 \mu\text{l}^{-1}$$

$$0.5 < Q < 3.0 \mu\text{l/s}$$

$$\frac{V}{Q} < 1000 \text{ s for } Q \geq 1.0 \mu\text{l/s}$$

$$\frac{V}{Q} < 300 \text{ s for } Q < 1.0 \mu\text{l/s}$$

These restrictions on the control parameters precluded the possibility of reaching a steady-state surface-coverage value. However, based on the extensive discussions and analyses presented in Sections 3.1.2 and 4.4.2, steady-state was assumed to be unity. Based on the collection of experimental results with surface coverage values spanning from zero to $f \approx 0.5$, there were no reasons to suspect otherwise.

4.4.7 Comparison of Experimental Results to the Model Description

A number of important findings have been discussed thus far, most of which have been circuitously building up to what is the overall theme of this section; a full description of particle-cell binding as a function of particle concentration, flow volume, and flow rate. Only the milestone findings need be recalled, and so are reiterated below.

The experimental data show that, for a fixed $Q=1.0 \mu\text{l/s}$,

$$f(N_p, V; Q = Q_{ref}) = \frac{C_1}{v_{max}} N_p V$$

Similarly, for a fixed $V=100 \mu\text{l}$, experiments show

$$f(N_p, Q, V = V_{ref}) = \frac{C_2}{v_{max}} \left(\frac{Q}{Q_0} \right)^{-.63} N_p$$

The mathematical model, in the small t/τ approximation, is

$$f(Q, N_p, V) \approx K_{on} \left(\frac{Q}{Q_0} \right)^{a-1} N_p V$$

In this approximation, the functional form of the mathematical model agrees precisely with the experimental findings. Therefore, the two unknown constant in the model, K_{on} and a , may be determined from empirical values. Comparison of the model to the experimental findings yields the following:

$$K_{on} Q_{ref}^{a-1} N_p V = \frac{C_1}{v_{max}} N_p V$$

$$K_{on} = \frac{C_1}{v_{max}} \left(\frac{Q_{ref}}{Q_0} \right)^{a-1} = (2.2 \pm .12) \times 10^{-8}$$

$$K_{on} V_{ref} Q^{a-1} N_p = \frac{C_3}{v_{max}} Q^{-.63} N_p$$

$$a = 1 - (.63 \pm .06)$$

Incorporating the empirical values into the theoretical model permits a full description of the fractional cell-surface coverage as a function of Q , N_p , and V simultaneously. Using nominal values, this is

$$v(Q, N_p, V) \approx 3 \times 10^{-6} \left(\frac{Q}{Q_0} \right)^{-.63} N_p V$$

Expressing this as fractional cell-surface coverage and putting it back in terms of t using $t=V/Q$

$$f(Q, N_p, V) \approx \frac{(3 \times 10^{-6})}{v_{max}} \left(\frac{Q}{\mu\text{l/s}} \right)^{.37} N_p t$$

Since particle desorption is negligible,

$$f(t) = f_{ss} \cdot \left(1 - \exp \left[-t/\tau \right] \right)$$

$$f_{ss} = 1$$

$$\begin{aligned} \tau &\equiv \left[K_{on} N_p \left(\frac{S}{S_0} \right)^a \right]^{-1} \\ &= \left[(2 \times 10^{-8}) N_p \left(\frac{Q}{Q_0} \right)^{.37} \right]^{-1} \end{aligned} \quad (57)$$

Thus, a full model description that is valid for any t has been obtained through comparison of experimental findings with the small t/τ approximation of the model. All experimental data discussed in this section have been plotted against the unabridged theoretical model, incorporating empirical values of K_{on} and a , as a function of t/τ in Figure 37. Under this scaling, it becomes clear that the model is in good agreement with the experimental data.

In the preceding sections, a model for $f(t)$ has been developed and an approximation to this model was made for small t/τ . Experimental data representing the early stage of particle-cell binding have been presented, and through comparison of these data with the model, subject to the small t/τ approximation, empirical values were obtained for K_{on} and a . By incorporating these values into the model, a full description of the particle-cell binding process that is valid for both small and large t/τ was recovered.

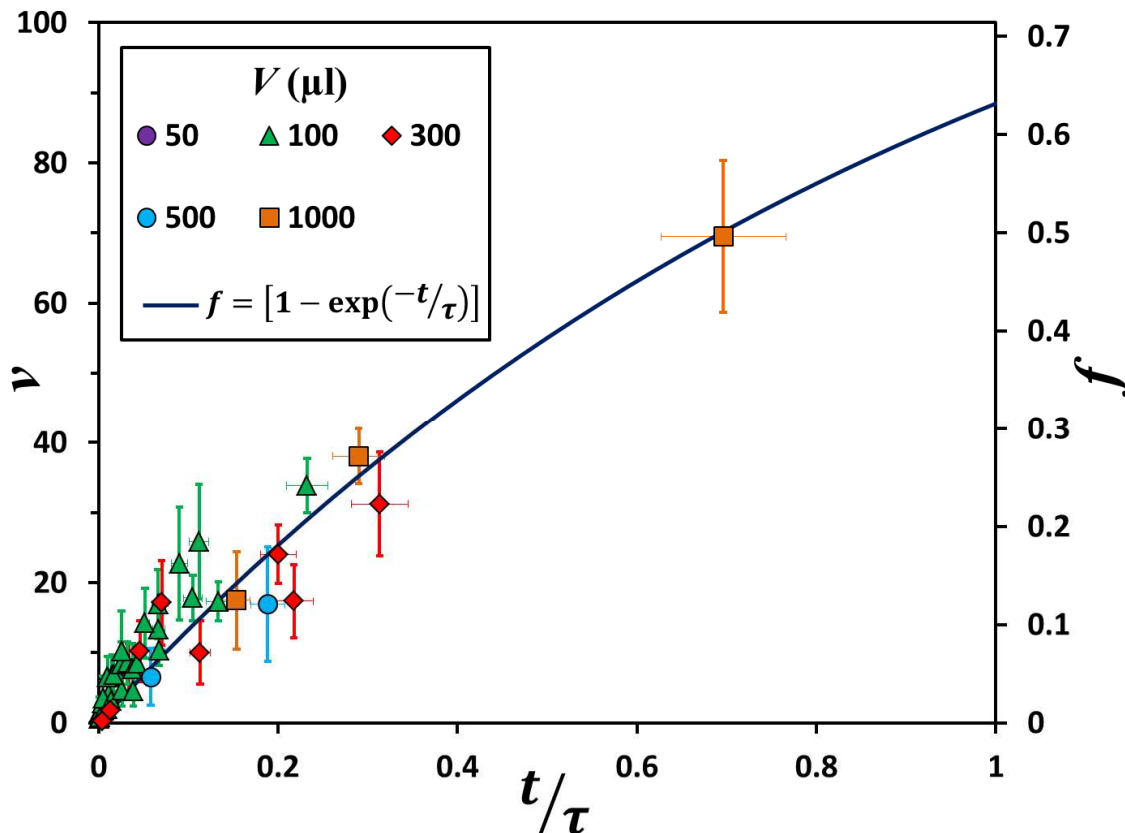


Figure 37 – Average number of bound particles per cell ν (left axis) and fractional cell-surface coverage f (right axis) as functions of time scaled by the time constant obtained from the theoretical model and calculated using the empirically-found value of K_{on} . All data appearing in Figure 28, Figure 29, Figure 32, Figure 33, Figure 34 and Figure 36 appear here. The solid curve was calculated from Equation 57. Different markers are for comparison and indicate different flow volumes without indicating any commonality among particle concentration or flow rate values.

5. GENERALIZED DESCRIPTION PARTICLE-CELL INTERACTION

While particle-cell interaction has been the theme of a large part of this work, its study has taken two considerably different paths. In Section 4.3, the study focused on the resulting surface coverage due to incubation of a suspension of both particles and cell. Since neither species was spatially constrained, other mechanisms such as cell-particle-cell interaction arose and had significant effects on resulting surface coverage. In contrast, when cells were immobilized in microchannels, interactions involving multiple cells were prevented. Furthermore, whereas in the former case, both particles and cells were subjected to unsteady flow, immobilized cells saw a steady flow of particle suspension. A consequence of this was that the relative velocity between particle and cell was increased greatly over that with both species in suspension.

Clearly, there are numerous effects that show themselves in only one of these systems. However, the fundamental mechanism that governs particle-cell binding, ligand-receptor interaction, is present in both systems. This is not to say this is the only similarity; only that it is the most fundamental. Therefore, there should be some commonality in the results obtained from experiments involving each of these systems. Looking back to the general form of the model, Equation 6, provides further insight.

$$\frac{dv(t)}{dt} = k_{on}N_p[1 - f(t)] - k_{off}v(t)$$

It has been shown that desorption is negligible in both cases so $k_{off}=0$.

$$\frac{dv(t)}{dt} = k_{on}N_p[1 - f(t)]$$

Development of the model branches very early on as a result of the varied shear strain rate. From here, the model incorporates different effects, but this is not to imply that this is where the similarities end. This is made most clear with a side-by-side comparison of the development of each. Henceforth, unconstrained particles and cells in suspension shall be referred to as system “A” and be described in the left column, while immobilized cells inside a microchannel with a flowing particle suspension shall be referred to as system “B” and be described in the right column.

Analysis must start with the adsorption rate in both cases. While it is constant in A, it is a function of shear strain rate in B.

| | |
|-----------------------------------|----------------------|
| $k_{on} = v_{max}K_{on} = const.$ | $k_{on} = k_{on}(S)$ |
|-----------------------------------|----------------------|

The presence of cell-particle-cell interactions introduces another term into the model for A. In B, a multiplicative factor influencing the adsorption rate appears and is dependent on shear strain rate.

| | |
|--|--|
| $\frac{df}{dt} = K_{on}N_p(1 - f - f_{nv})$ $\frac{df}{dt} = K_{on}N_p(1 - f) - K_{nv}f$ | $\frac{df(t)}{dt} = K_{on} \left(\frac{S}{S_0}\right)^a N_p[1 - f(t)]$ |
|--|--|

The model branches diverge significantly at this point. B is ready for solution, but before solution of A, the f_{nv} term must be addressed. Following the discussion of Section 4.3.5, f_{nv} is approximated as proportional to f and K_{on} and N_p are absorbed into $K_{nv}=K_{nv}(N_p)$.

| | |
|--|--|
| $f(t) = \frac{K_{on}N_p}{K_{on}N_p + K_{nv}} \left[1 - e^{-(K_{on1}N_p + K_{nv})t} \right]$ | $f(t) = 1 - \exp \left[-K_{on}N_p \left(\frac{S}{S_0} \right)^a t \right]$ |
|--|--|

As a result of the desorption-type term, A admits a solution that has a steady state depending on various rates. In contrast, B has a steady state of unity.

| | |
|---|--------------|
| $f_{ss} = \frac{K_{on}N_p}{K_{on}N_p + K_{nv}}$ | $f_{ss} = 1$ |
|---|--------------|

Both A and B have time constants that are inversely proportional to N_p . B, however has an additional parameter which also appears in the time constant.

| | |
|----------------------------|--|
| $\tau(N_p) = C_1 N_p^{-1}$ | $\tau \equiv \left[K_{on2} N_p \left(\frac{S}{S_0} \right)^a \right]^{-1}$ |
|----------------------------|--|

With the scaling parameters established, both systems are described by the following equation:

$$f(t) = f_{ss} \left(1 - \exp \left[-t/\tau \right] \right) \quad (58)$$

By using their respective time constants and steady-state values as scaling parameters, the same exponential function is recovered from both branches. This indicates that despite the differing mechanisms involved, the fundamental mechanisms results in first-order behavior and particle-cell binding is thus still well-described as a first-order process. When the experimental data are

normalized by their corresponding time constant and steady state values, they fall along the same exponential curve that was recovered from both branches of the model; Equation 58. The normalized data are plotted against the curve calculated using Equation 58 in Figure 38.

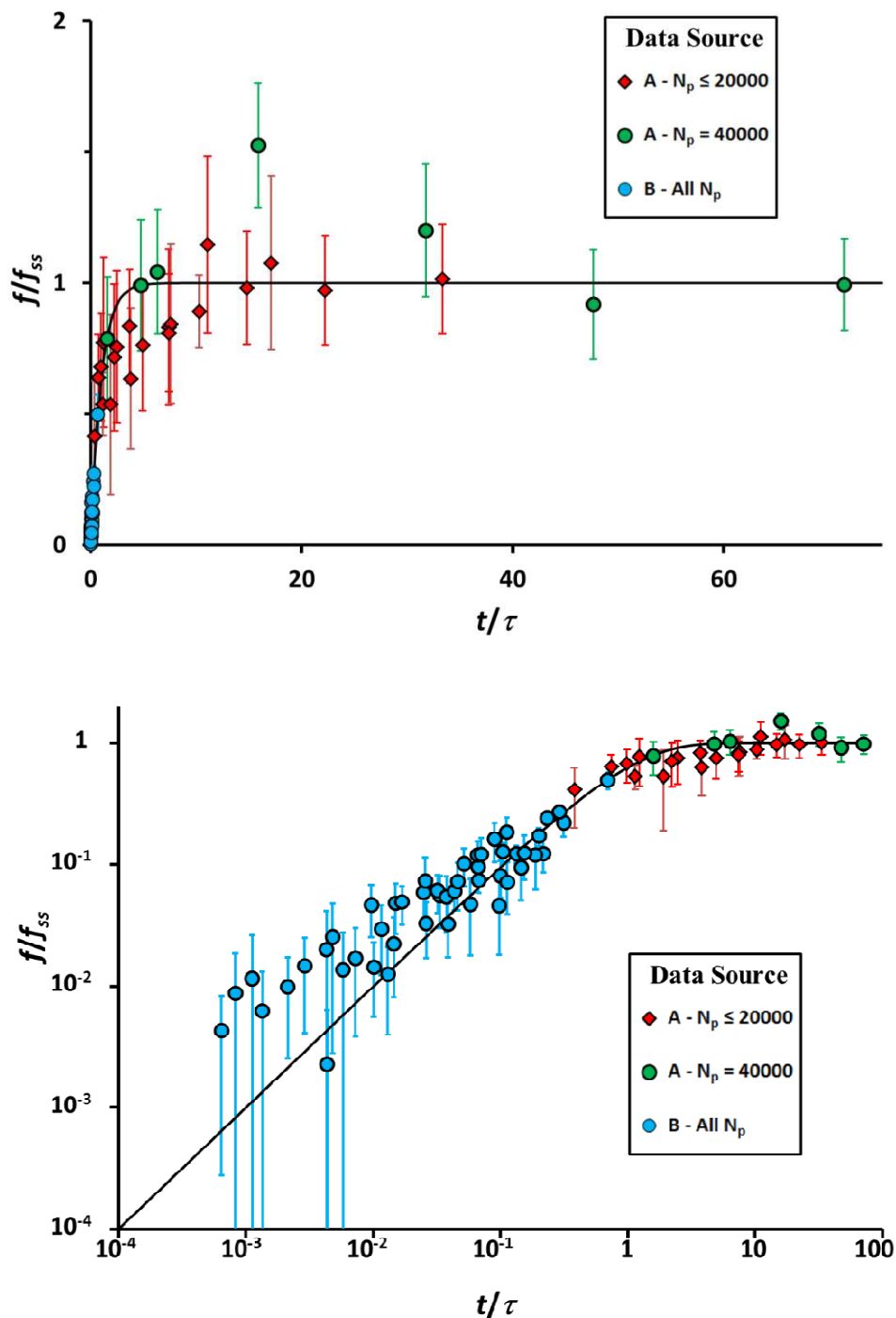


Figure 38 – Cell surface coverage normalized by its steady-state value, f/f_{ss} , as a function of the normalized incubation time, t/τ , plotted on a normal scale (top) and a log-log scale (bottom). Experimental results shown in Figure 18 and Figure 19 (set “A”) and in Figure 28, Figure 29, Figure 33 and Figure 34 (set “B”) collapse onto a single exponential curve (calculated using Equation 58). Set “A” corresponds to data resulting from experiments with cells freely moving in suspension as described in Section 4.3. Set “B” corresponds to data resulting from experiments

involving immobilized cells in a microchannel as described in Section 4.4. Only the data for the high particle concentration of $N_p=40000 \mu\text{l}^{-1}$ in set “A” deviate substantially. This deviation occurs when cell-particle-cell clustering is at its highest, as seen from Figure 23. This phenomenon is not described by the model, which examines the process on an individual-cell level.

6. CONCLUSIONS

Particle dynamics due to non-specific interactions leading to aggregation inside a microchannel have been investigated. A method of functionalizing particles with antibodies in order to achieve specific-targeting capabilities has been developed. The specific interactions between functionalized particles and target cells have been studied in two significantly different types of microfluidic systems. A mathematical model of particle-cell interaction has been developed and compared with experimental results.

The initial stage of cluster growth in a microchannel due to the flow of dilute suspensions of polystyrene microparticles was investigated experimentally and analyzed theoretically. The effects of suspension void fraction ϕ , wall shear strain rate S , and channel-height to particle-diameter ratio h/d , on the cluster growth rate were independently examined. The experimental data show that during the initial stages of cluster growth, the averaged cluster area growth rate depends linearly on suspension void fraction. The cluster growth rate coefficient β is independent of the void fraction and obeys a power-law relationship with the shear strain rate. The exponent value depends on the evolution of the cluster height; assuming a hemispherical cluster shape results in $\beta \propto S^{0.9 \pm 0.1}$. The cluster growth rate coefficient also obeys a power-law relationship with the channel-height to particle-diameter ratio, $\beta \propto (h/d)^{-3.5 \pm 0.25}$, for h/d in the range of 3 to 10.

The linear dependence of cluster area growth rate on the suspension void fraction predicted based on Smoluchowski's theoretical model agrees well with the current experimental results. The dependence of the cluster growth rate coefficient on shear strain rate reported elsewhere based on a modernized flocculation theory [58] was found to be in agreement, within

experimental error, with the empirical power law established in this study. The cluster growth rate coefficient dependence on the channel-height to particle-diameter ratio does not, to the author's knowledge, agree with previously observed or predicted results. This is likely due to the dependence of the capture volume length scale λ on the particle diameter d and particularly the channel height h ; this dependence is expected to be strongly affected by the particular experimental conditions. Nevertheless, the power-law established in this work is qualitatively consistent with similar experimental studies with an exponent value on the same order of magnitude.

A novel class of ceramic liposomal nanoparticles, cerasomes, has been functionalized with fluorescently-tagged antibodies on their surfaces. The bio-functionality of the cerasomes has been confirmed by examining the presence of the antibodies on the cerasome surface using fluorescence microscopy. SEM revealed no obvious changes in size and shape of the functionalized cerasomes compared with unmodified ones, demonstrating the integrity of the functionalized cerasomes. This functionalization method, in general, is not limited to the use of a particular type of antibodies. Therefore, the method described herein can be used to create functionalized cerasomes tailor-made for any target cell type by immobilizing proper counter-receptor antibodies. Particles functionalized with the proper counter-receptor showed a significantly increased attachment efficiency to target cancer cells over particles functionalized with other antibodies. The cerasomes with immobilized antibodies, which act as homing ligands, promise great potential for drug therapy with significantly improved selectivity over standard liposomes.

A quantitative characterization of interactions of functionalized particles with target cells has been performed and a mathematical model of particle-cell interaction has been developed. The interactions between functionalized particles and target cells were studied in two different microfluidic systems; a freely mixed suspension of both particles and cells, and a microfluidic device in which cells were immobilized and subjected to particle suspension flow.

With both species in suspension, it was found that cell-surface coverage by particles does increase with particle concentration, but not necessarily with incubation time. An apparent concentration-dependent steady-state value was reached after sufficient incubation time. For high particle concentration, an overshoot and subsequent decrease in surface coverage were observed. It was determined that neither particle-desorption nor loss of binding affinity over time could account for the observed behavior. Theoretical considerations showed that particle-cell interaction alone could not fully explain observations and experiments indeed showed cell-particle-cell interactions were the dominant mechanism in determining the number of particles bound to cells. These findings suggest that separation of a bound particle from a cell may result in loss of binding affinity. With the exception of the case of high particle concentration, for which cell-particle-cell interaction was most significant, particle-cell binding was found to be reasonably well described by a first-order model. The steady state value was found to be directly proportional to the square-root of particle concentration $f_{ss} \propto N_p^{1/2}$, while the time constant was found to be inversely proportional to particle concentration $\tau \propto N_p^{-1}$. The overshoot in surface coverage observed for high particle concentration is not described by the model.

Particle-cell interaction was further investigated by incorporating a microfluidic device to immobilize cells thereby preventing cell-particle-cell interaction. The use of microchannels also

allowed for the accurate control of shear strain rate. The effects of shear strain rate, particle concentration, and incubation time, on the early stage of particle-cell binding were studied using this microfluidic system. Through an asymptotic analysis, experimental investigation of the linear stage of particle-cell binding provided empirical values that, when incorporated into the model, provide a model description valid for all stages to be obtained. It was again found that a first-order model describes the particle-cell binding process reasonably well. The steady-state value was found to be independent of the control parameters within the ranges tested. This is consistent with the previous finding indicating the dominance of cell-particle-cell interaction in determining the final number of particles bound to a cell. The time constant was found to be inversely proportional to the particle concentration, consistent with previous findings, and to obey a power law with shear strain rate as $\tau \propto S^{-.37 \pm .06}$.

By using the steady-state values and time constants as scaling parameters, it was shown that, regardless of which microfluidic system was utilized, the resulting experimental data were well-described by the first-order model (with the single aforementioned exception). These findings could be of substantial importance in clinical applications. By obtaining two empirical values and identifying proper scaling parameters, a semi-empirical model has been constructed that is suitable for extrapolation. By following the principles of this work, one may greatly reduce the parameter space (and indeed the dimension thereof) that would otherwise be spanned during clinical testing, saving time, money, and ultimately lives.

REFERENCES

- [1] G H Goldsztein and J C Santamarina, "Suspension extraction through an opening before clogging," *Appl Phys Lett*, vol. 85, no. 9, pp. 4535-4537, 2004.
- [2] K V Sharp and R J Adrian, "On flow-blocking particle structures in microtubes," *Microfluid Nanofluid*, vol. 1, no. 4, pp. 376-380, 2005.
- [3] Y Gu and D Li, "Deposition of spherical particles onto cylindrical solid surfaces: I. Numerical simulations," *J Colloid Interface Sci*, vol. 248, no. 2, pp. 315-328, 2002.
- [4] Y Gu and D Li, "Deposition of spherical particles onto cylindrical solid surfaces: II. Experimental studies," *J Colloid Interface Sci*, vol. 245, no. 2, pp. 329-339, 2002.
- [5] X Xuan and D Li, "Particle motions in low Reynolds number pressure-driven flows through converging-diverging microchannels," *J Micromechanics & Microeng*, vol. 16, no. 1, pp. 62-69, 2006.
- [6] J S Marshall, "Particle aggregation and capture by walls in a particulate aerosol channel flow," *J Aerosol Sci*, vol. 38, no. 3, pp. 333-351, 2007.
- [7] A Konstandopoulos, "Deposit growth dynamics: particle sticking and scattering phenomena," *Powder Technol*, vol. 109, no. 1-3, pp. 262-277, 2000.
- [8] P Raiskinmaki et al., "Clustering and viscosity in a shear flow of a particulate suspension," *Phys Rev E*, vol. 68, no. 6, p. 061403, 2003.
- [9] S Wang, H Lu, Z Shen, H Liu, and J Bouillard, "Prediction of flow behavior of micro-particles in risers in the presence of van der Waals forces," *Chem Eng*, vol. 132, no. 1-3, pp. 137-149, 2007.
- [10] TGM Van de Ven and S G Mason, "The microrheology of colloidal dispersions VII: Orthokinetic doublet formation of spheres," *J Colloid and Polymer Sci*, vol. 255, no. 5, pp. 468-479, 1977.
- [11] J L Perry and S G Kandlikar, "Fouling and its mitigation in silicon microchannels used for IC chip cooling," *Microfluid Nanofluid*, vol. 5, no. 3, pp. 357-371, 2008.
- [12] C J Koh, P Hookham, and L G Leal, "An experimental investigation of concentrated suspension flows in a rectangular channel," *J Fluid Mech*, vol. 266, no. 1, pp. 1-32, 1994.
- [13] D Semwogerere and E R Weeks, "Shear-induced particle migration in binary colloidal suspensions," *Phys Fluids*, vol. 20, no. 4, p. 043306, 2008.
- [14] D Semwogerere, J F Morris, and E R Weeks, "Development of particle migration in pressure-driven flow of a Brownian suspension," *J Fluid Mech*, vol. 581, no. 1, pp. 437-451, 2007.
- [15] M Vanni and G Baldi, "Coagulation efficiency of colloidal particles in shear flow," *Adv Colloid Interface Sci*, vol. 97, no. 1-3, pp. 149-175, 2002.

- [16] H Mousa, W Agterof, and J Mellema, "Experimental investigation of the orthokinetic coalescence efficiency of droplets in simple shear flow," *J Colloid Interface Sci*, vol. 240, no. 1, pp. 340-348, 2001.
- [17] H N Unni and C Yang, "Brownian dynamics simulation and experimental study of colloidal particle deposition in a microchannel flow," *J Colloid Interface Sci*, vol. 291, no. 1, pp. 28-36, 2005.
- [18] TGM Van de Ven and S G Mason, "The microrheology of colloidal dispersions IV: Pairs of interacting spheres in shear flow," *J Colloid Interface Sci*, vol. 57, no. 3, pp. 505-516, 1976.
- [19] J A Maroto and F J de las Nieves, "Theoretical and experimental comparison of the colloid stability of two polystyrene latexes with different sign and value of the surface charge," *Colloid Polymer Sci*, vol. 276, no. 6, pp. 453-458, 1998.
- [20] O Spalla and B Cabane, "Growth of colloidal aggregates through polymer bridging," *Colloid Polymer Sci*, vol. 271, no. 4, pp. 357-371, 1993.
- [21] M Tirado-Miranda, A Schmitt, J Callejas-Fernndez, and A Fernandez-Barbero , "Colloidal clusters with finite binding energies: Fractal structure and growth mechanism," *Langmuir*, vol. 15, no. 10, pp. 3437-3444, 1999.
- [22] E Brunet, G Degre, F Okkels, and P Tabeling, "Aggregation of paramagnetic particles in the presence of a hydrodynamic Shear," *J Colloid Interface Sci*, vol. 282, no. 1, pp. 58-68, 2005.
- [23] H M Wyss, D L Blair, J F Morris, H A Stone, and D A Weitz, "Mechanism for clogging of microchannels," *Phys Rev E*, vol. 75, no. 6, p. 061402, 2006.
- [24] T Gudipaty, M T Stamm, L SL Cheung, L Jiang, and Y Zohar, "Cluster formation and growth in microchannel flow of dilute particle suspensions," *Microfluid Nanofluid*, vol. 10, no. 3, pp. 661-669, 2011.
- [25] D Conrad, "Tumor-seeking nanoparticles," *NCI Alliance for nanotechnology in cancer - monthly feature*, pp. 1-3, September 2006.
- [26] L Cavalcanti, O Konovalov, I Torriani, and H Haas, "Drug loading to lipid-based cationic nanoparticles," *Nucl Instrum Methods Phys Res*, vol. 238, no. 1-4, pp. 290-293, 2005.
- [27] T Lian and R J Y Ho, "Trends and developments in liposome drug delivery systems," *J Pharm Sci*, vol. 90, no. 6, pp. 667-680, 2001.
- [28] P Pathak and V K Katiyar, "Multi-functional nanoparticles and their role in cancer drug delivery – A Review," *J Nanotech Online*, vol. 3, May 2007.
- [29] D C Drummond, O Meyer, K Hong, D B Kirpotin, and D Papahadjopoulos, "Optimizing liposome delivery of chemotherapeutic agents to solid tumors," *Pharmacol Rev*, vol. 51, no. 4, pp. 691-744, 1999.

- [30] Z Cao et al., "Stabilized liposomal nanohybrid cerasomes for drug delivery applications," *Chem Commun*, vol. 46, no. 29, pp. 5265-5267, 2010.
- [31] K Jain, "Editorial: Targeted drug delivery for cancer," *Technol Cancer Res*, vol. 4, no. 4, pp. 311-313, 2005.
- [32] C Fan et al., "Tumor selectivity of stealth multi-functionalized superparamagnetic iron oxide nanoparticles," *Int. J. Pharm.*, vol. 404, no. 1-2, pp. 180-190, 2011.
- [33] D Simberg et al., "Biomimetic amplification of nanoparticle homing to tumors," *Proc. Natl. Acad. Sci.*, vol. 104, no. 3, pp. 932-936, 2007.
- [34] F Kiessling et al., "RGD-labeled USPIO inhibits adhesion and endocytotic activity of alpha v beta3-integrin-expressing glioma cells and only accumulates in the vascular tumor compartment," *Radiology*, vol. 253, no. 2, pp. 462-469, 2009.
- [35] C Fang et al., "Functionalization of iron oxide magnetic nanoparticles with targeting ligands: their physicochemical properties and in vivo behavior," *Nanomedicine (Lond)*, vol. 5, no. 9, pp. 1357-1369, 2010.
- [36] K Morishige et al., "High-resolution magnetic resonance imaging enhanced with superparamagnetic nanoparticles measures macrophage burden in atherosclerosis," *Circulation*, vol. 122, no. 17, pp. 1707-1715, 2010.
- [37] A Tsourkas et al., "In vivo imaging of activated endothelium using an anti-VCAM-1 magneto-optical probe," *Bioconjug. Chem.*, vol. 16, no. 3, pp. 576-581, 2005.
- [38] K A Kelly et al., "Detection of vascular adhesion molecule-1 expression using a novel multimodal nanoparticle," *Circ. Res.*, vol. 96, pp. 327-336, 2005.
- [39] M Hashizume, S Kawanami, S Iwamoto, T Isomoto, and S Kikuchi, "Stable vesicular nanoparticle 'Cerasome' as an organic-inorganic hybrid formed with organoalkoxysilane lipids having a hydrogen-bonding unit," *Thin Solid Films*, vol. 438-439, no. 22, pp. 20-26, 2003.
- [40] K Katagiri, M Hashizume, K Ariga, T Terashima, and J Kikuchi, "Preparation and characterization of a novel organic-inorganic nanohybrid 'cerasome' formed with a liposomal membrane and silicate surface," *Chemistry*, vol. 13, no. 18, pp. 5272-5281, 2007.
- [41] X Yue, Y Jing, and Z Dai, "Liposomal cerasome: a nanohybrid of liposome and silica," *Asia-Pac J Chem Eng*, vol. 6, no. 4, pp. 569-574, 2011.
- [42] K Katagiri, R Hamasaki, K Ariga, and J Kikuchi, "Preparation and surface modification of novel vesicular nano-particle 'cerasome' with liposomal bilayer and silicate surface," *J Sol-gel Sci Techn*, vol. 26, pp. 393-396, 2003.
- [43] L E van Vlerken and M M Amiji, "Multi-functional polymeric nanoparticles for tumour-targeted drug delivery," *Expert Opin Drug Del*, vol. 3, no. 2, pp. 205-216, 2006.

- [44] O C Farokhzad et al., "Microfluidic System for Studying the Interaction of Nanoparticles and Microparticles with Cells," *Anal. Chem.*, vol. 77, no. 17, pp. 5453–5459, 2005.
- [45] M T Stamm, Z Zha, L Jiang, Z Dai, and Y Zohar, "Functionalization of particles with antibodies for specific targeting of cancer cells," *J Physic Chem Biophysic*, vol. 2, no. 1, p. 1000105, 2012.
- [46] R Julien and R Botet, *Aggregation and Fractal Aggregates*. Singapore: World Scientific, 1987.
- [47] Y Sasaki, K Matsui, Y Aoyama, and J Kikuchi, "Cerasome as an infusible and cell-friendly gene carrier: synthesis of cerasome-forming lipids and transfection using cerasome," *Nature Protocols*, vol. 1, no. 3, pp. 1227-1234, 2006.
- [48] P T Went et al., "Frequent EpCAM protein expression in human carcinomas," *Hum Pathol*, vol. 35, no. 1, pp. 122-128, 2004.
- [49] S C Leeuwenburgh, I D Ana, and J A Jansen, "Sodium citrate as an effective dispersant for the synthesis of inorganic-organic composites with a nanodispersed mineral phase," *Acta Biomater*, vol. 6, no. 3, pp. 836-844, 2010.
- [50] I Migneault, C Dartiguenave, M J Bertrand, and K C Waldron, "Glutaraldehyde: behavior in aqueous solution, reaction with proteins, and application to enzyme crosslinking," *Biotechniques*, vol. 37, no. 5, pp. 790-796, 798-802, 2004.
- [51] J K Kim et al., "Enhanced proton treatment in mouse tumors through proton irradiated nanoradiator effects on metallic nanoparticles," *Phys Med Biol*, vol. 57, no. 24, pp. 8309-8323, 2012.
- [52] P Cherukat and J B McLaughlin, "The inertial lift on a rigid sphere in a linear shear flow field near a flat wall," *Journal of Fluid Mechanics*, vol. 263, pp. 1-18, 1994.
- [53] P Cherukat, J B McLaughlin, and A L Graham, "The inertial lift on a rigid sphere translating in a linear shear flow field," *International Journal of Multiphase Flow*, vol. 20, no. 2, pp. 339–353, 1994.
- [54] K P Ivanov, M K Kalinina, and Y I Levkovich, "Blood flow velocity in capillaries of brain and muscles and its physiological significance," *Microvasc Res*, vol. 22, no. 2, pp. 143-155, 1981.
- [55] L J Latecki, A Lazarevic, and D Pokrajac, "Outlier Detection with Kernel Density Functions," *Lect Notes Artif Int*, vol. 4571, pp. 61-75, 2007.
- [56] C B Korn and U S Schwarz, "Dynamic states of cells adhering in shear flow: from slipping to rolling," *Phys Rev E Stat Nonlin Soft Matter Phys*, vol. 77, no. 4-1, p. 041904, 2008.

- [57] D A Hammer and S M Apte, "Simulation of cell rolling and adhesion on surfaces in shear flow: general results and analysis of selectin-mediated neutrophil adhesion," *J Biophys*, vol. 63, no. 1, pp. 35-57, 1992.
- [58] J Gregory, "Flocculation in laminar tube flow," *Chem Eng Sci*, vol. 36, no. 11, pp. 1789-1794, 1981.
- [59] E Yamaguchi and R Adrian, "Theoretical and experimental study of microchannel blockage phenomena," in *21st Int Congr Theor Appl Mech*, Warsaw, 2004, pp. 15-21.
- [60] L M Lee, R L Heimark, J C Baygents, and Y Zohar, "Self-aligned immobilization of proteins utilizing PEG patterns," *Nanotechnology*, vol. 17, no. 4, pp. S29-S33, 2006.
- [61] L S L Cheung et al., "Detachment of captured cancer cells under flow acceleration in a bio-functionalized microchannel," *Lab Chip*, vol. 9, no. 12, pp. 1721-1731, 2009.
- [62] M D Butterworth, R Corradi, J Johal, S F Lascelles, and S P Armes, "Zeta-potential measurements on conducting polymer-inorganic oxide nanocomposite particles," *J Colloid Interf Sci*, vol. 174, no. 2, pp. 510-517, 1995.
- [63] M T Stamm, T Gudipaty, C Rush, L Jiang, and Y Zohar, "Particle aggregation rate in a microchannel due to a dilute suspension flow," *Microfluid Nanofluid*, vol. 11, no. 4, pp. 395-403, 2011.
- [64] Y M Bae, B K Oh, W Lee, W H Lee, and J W Choi, "Study on orientation of immunoglobulin G on protein G layer," *Biosens Bioelectron*, vol. 21, no. 1, pp. 103-110, 2005.
- [65] M C Miller, G V Doyle, and L W M M Terstappen, "Significance of Circulating Tumor Cells Detected by the CellSearch System in Patients with Metastatic Breast Colorectal and Prostate Cancer," *J Oncol*, vol. 2010, p. 617421, 2010.
- [66] M T Stamm, Z Zha, L Jiang, Z Dai, and Y Zohar, "Functionalization of ceramic liposomal nanoparticles, cerasomes, with antibodies," in *16th International Conference on Solid-State Sensors, Actuators and Microsystems*, Beijing, 2011, pp. 226-229.